2009

Matter sources interacting with a black hole: dynamics and observable signatures

Miguel Megevand
Louisiana State University and Agricultural and Mechanical College

MATTER SOURCES INTERACTING WITH A BLACK HOLE: DYNAMICS AND OBSERVABLE
SIGNATURES

A Dissertation

Submitted to the Graduate Faculty of the
Louisiana State University and
Agricultural and Mechanical College
in particular fulfillment of the
requirements for the degree of
Doctor of Philosophy

in

The Department of Physics and Astronomy

by
Miguel Megevand
Licenciado en Física, Universidad Nacional de Córdoba, 2003
December 2009

Acknowledgements

First, I would like to thank my advisor, Luis Lehner, for all that he has taught me, from the very basics of doing research in physics to the more specific concepts of numerical relativity, and for the great patience he exhibited in working with me during these years. It was truly a pleasure to work with him.

In addition, I thank Matt Anderson, Sarvnipun Chawla, Travis Garrett, Iñaki Olabarrieta, Carlos Palenzuela and Jorge Pullin, present and past members of the LSU Relativity Group, as well as Eric Hirschmann, Steve Liebling and David Neilsen, members of our collaboration group. I have learned much from the innumerable discussions with them. I also want to thank Juhan Frank, Patrick Motl, Jan Staff and Joel Tohline for all their help in astrophysics related matters, especially Juhan for his patience when frequently knocking at his door for advice. Finally, I thank Gabriela Gonzalez and Robert Hynes for their useful suggestions to this dissertation.

Table of Contents

Abstract

Dynamical systems involving black holes are one of the most promising sources of detectable gravitational waves. Additionally, one expects strong electromagnetic signals whenever matter sources are present. In this dissertation, we study different astrophysical scenarios pertaining the interaction of matter with a black hole.

We first investigate the possibility to localize scalar field configurations surrounding a (dynamic) black hole. The analytical study is illustrated by performing numerical simulations that show the evolution of a Klein-Gordon-like scalar field shell surrounding a black hole. Second, we present a method to estimate the gravitational wave frequency at the end of the inspiral phase of a compact binary. This method is applied to study the possibility of a neutron star's tidal disruption occurring before plunging into the companion black hole, and to provide a way of improving gravitational wave data analysis when using match filtering techniques. Last, we study the effects of a black hole merger on a circumbinary disk. We consider separately the effects of central mass reduction (due to the energy loss through gravitational waves) and black hole recoil (due to asymmetric emission of gravitational radiation), presenting possibly detectable electromagnetic signatures.

Chapter 1
Introduction

A large area of astrophysics concentrates on the study of the dynamics of compact objects, and the interaction with matter that usually surrounds them, as these are central to explain energetic observable phenomena, like gamma ray bursts and others yet to be observed by means of gravitational waves. Systems of interest include the collision of binary black holes and neutron stars, black holes interacting with an accretion disk, supernova core collapse, etc.

The study of these systems, in which the curvature of space-time is strong, requires applying Einstein theory of Relativity (of which a brief overview is given in section 1.1). Whole areas of theoretical research in physics, like Numerical Relativity and Gravitational Wave Astronomy, are based on the study and application of the theory of General Relativity to understand astrophysical systems and processes.

At the experimental (or observational) level, the detection of electromagnetic waves (ranging from radio signals to gamma rays) has provided for many years the only observable signatures of theses systems. Recently, technological advances permitted the construction of gravitational wave detectors, such as the Laser Interferometer Gravitational-Wave Observatory (LIGO) [1], that will open a new window in the the study of our universe. However, gravitational waves couple very weakly, meaning that only those generated in very strong sources, and sufficiently close, might be detected, such as the collision of black holes and neutron stars, and even in these cases the detection and data analysis represent a difficult enterprise. This fact makes particularly important the interaction between theory, detection and interpretation. For instance, applying theoretical models in the data analysis (in the form of templates) can improve the probability of detection of gravitational waves (see chapter 3 and references therein).

The astrophysical processes that generate gravitational waves strong enough to be detected are usually also sources of electromagnetic radiation. Even if the gravitational wave source itself does not emit electromagnetic radiation, the surrounding gas can be affected, either directly by the compact objects involved in the process, or indirectly through the gravitational waves they emit. Variations in the electromagnetic radiation of the affected gas may provide signatures of the given astrophysical process. For example, a binary black hole may produce a quasiperiodic electromagnetic signal associated with the orbital motion prior to merging if gas is involved [2].

The detection of optical counterparts may also be particularly important to prove the first gravitational waves detected. On the other hand, the detection of one type of wave could help in the detection of the other. For example, triangulation from the Laser Interferometer Space Antenna (LISA) may localize a source within 1 square degree. This would not be precise enough to directly point a telescope and observe the electromagnetic counterpart, however, telescopes could monitor that portion of the sky in search for unusual electromagnetic emission that could identify a unique host galaxy. Triangulation is also possible by combining different ground based detectors located far away from each other, like the two LIGO observatories and VIRGO [3].

The combined study of gravitational and electromagnetic signals can be useful also in fundamental physics. Dark energy researchers have explored the possibility that the accelerated expansion of the universe results from a failure of general relativity in cosmological scales. The simultaneous study of gravitational and electromagnetic radiation from a single, distant, source could probe dark energy as a manifestation of modified gravity on large scales [4].

An example of processes involving both types of radiation is the collision of a black hole with a neutron star, where, besides the gravitational waves emitted by the binary, there are variations in the electromagnetic radiation of the star due to the interaction with the black hole. In this case, the tidal disruptions can be studied, for instance, to determine intrinsic properties of the neutron stars (see chapter 3).

A less obvious case in which both types of waves may be generated is that of a binary black hole merger. Though the black holes can not emit electromagnetic waves themselves, they are usually surrounded by matter. An example of this situation is that of a galaxy with a super-massive black hole at its core. It is widely accepted today that most (if not all) galaxies have indeed a super-massive black hole at their core, with masses of about 10^5 to 10^8 times the mass of the sun, although the details of the mechanisms leading to form such enormous black holes is not yet well understood. During their evolution, these galaxies undergo collisions with other galaxies. To illustrate this, we show in Figure 1.1 a Hubble Space Telescope image of NGC 4676, or "the Mice Galaxies", showing these two galaxies in the process of colliding, and eventually merging into a single galaxy. A closer example is our own Milky Way, which is expected to collide with the Andromeda Galaxy in about two billion years.

Figure 1.1: Hubble Space Telescope image of NGC 4676, the Mice Galaxies.

After the galaxies merge, the black holes start orbiting each other inside the newly formed galaxy. The distance between the black holes then begins to shrink slowly, initially because of the interaction with surrounding gas, and later, once they are close enough, because of the angular momentum loss due to the emission of gravitational radiation. This process continues until the black holes merge. During most of this process gas accretes into each black hole. However, in the last stages the gas can not follow the quickly shrinking binary, and a gap forms between the accretion disk and the binary. The inner edge of the disk continues shrinking initially, until reaching an equilibrium, at which point the disk's inner edge "freezes" at that position and the disk remains quasi-stationary, while the black holes continue getting closer until they merge. This effect is due in part by the torques exerted by the quickly rotating binary and the viscosity in the disk. See, for instance, [5] for a more detailed description of this process.

As the black holes inspiral and merge into a single black hole, they emit gravitational radiation, which carries away mass and momentum, meaning that the mass of the resulting black hole will be less than that of the binary, and it may have a recoil velocity (with respect to the binary's center of mass) if the total linear momentum radiated is not zero.

The mass loss and recoil of the central object will cause a large disruption of the disk that is orbiting on its gravitational potential, causing shocks in the gas and increasing its temperature. The hot gas may then release energy in the form of electromagnetic radiation.

We have just mentioned some examples of systems involving compact objects, stressing the importance of such systems that emit both electromagnetic and gravitational waves. In this dissertation I study aspects of the interaction of black holes with the surrounding matter and other compact objects. The study includes the coalescence of black holes with neutron stars and other black holes, and their interaction with scalar fields and circumbinary disks. This involves formulating and solving very complex systems of partial differential equations, which requires, besides analytical derivations, the use of high performance computing to solve the equations numerically.

After giving a brief overview of Einstein's theory of gravitation and gravitational waves in the rest of this introductory chapter, I go on, in chapter 2, to study a case involving the Einstein's equations coupled to a Klein-Gordon field, which not only allows for testing the techniques used in Numerical Relativity, but also presents the challenge at the theoretical level. In that chapter I investigate the possibility of confining a scalar field to a region around a black hole. To that end I first present an analytical study in spherical symmetry showing that, in that case, one can define a coordinate dependent potential for the scalar field, and in particular it can be given the form of a potential well. To test the ability of this potential to confine the scalar field I wrote a numerical code to solve the Einstein equations coupled to a Klein-Gordon field in spherical symmetry, and analyzed the corresponding solutions. This study provides a simple model that can be useful for mimicking features of accreting matter into black holes and for testing more complicated numerical codes. It also has pedagogical motivations, since it involves dealing (in the simpler setup of spherical symmetry) with most of the difficulties normally encountered in Numerical Relativity, i.e.: some analytical derivations, the formulation of the Einstein (and matter) equations in an appropriate form for the numerical integration, solving the constraint equations to obtain consistent initial data, writing and testing a numerical code and analyzing the solutions obtained.

Next, in chapter 3, I concentrate on black hole-neutron star collisions. These binaries can emit gravitational waves, possibly detectable by ground based interferometer detectors such as LIGO. I study a method to estimate time-frequency characteristics of compact binary mergers, showing implications on the ability to probe the tidal disruption of neutron stars through gravitational waves. We also show that this estimation is also very useful in the analysis of gravitational wave signals, in which knowing the end frequency of the inspiral phase of binary systems can improve searches of gravitational signatures from a compact binary coalescence.

Finally, in Chapter 4, I study the effects of black hole merger on a surrounding disk of gas. This include those caused by a reduction in the total mass of the binary and a recoil of the resulting black hole. Both effects are due to the emission of gravitational waves, which carry away mass and momentum. This study involves solving numerically the relativistic fluid equations for a disk of gas on a spinning black hole space-time. The numerical simulations show variations in the gas energy that would translate into variations of electromagnetic radiation that might be observable, thus providing an electromagnetic counterpart to the gravitational waves generated in the black holes' collision.

1.1 Einstein's Theory of Relativity

Einstein's theory of General Relativity is a theory of gravity that gives a geometrical description of space-time. In the Newtonian theory of gravity (and also in the special theory of Relativity) the space-time is implicitly assumed to be flat, and massive objects exert an attraction force on other massive objects given by Newton's law of gravitation,

$$F = G\frac{m_1 m_2}{r^2}.$$

Thus, for example, the orbits of a planet around the sun can be explained by applying this law, together with Newton's laws of motion.

On the other hand, in the relativistic description there is no gravitational force. Instead, massive objects cause the space-time around them to curve, and free particles then depart from straight motion due to that curvature. In our example of the sun and planets, the sun instead of attracting the planets, "bends" the space-time around it, and the planets are actually in free motion on that curved space-time. This description still explains the orbits of the planets, since in a curved space-time the trajectories of free particles are not straight lines. Instead, they move along geodesics, which are defined to be the shortest path between two given points (a generalization of a straight line for curved space). In this case, the closed geodesics correspond to the orbits. (Notice that for this simple example the planet is treated as a point particle and the curvature that it would produce on the space-time is neglected.)

In the previous example, the Newtonian theory gives a very good description and usually one does not need to apply the theory of relativity to study the motion of planets. That is not the case when considering other systems, like for instance those involving compact astronomical objects. This is because the curvature at a given region depends on the amount of matter and how it is distributed, being larger for larger mass concentrated on a small region.

However, relativistic effects are sometimes noticeable even in systems without a strong curvature in the case of very precise measurements, or if observations are carried over an extended period of time. An example is the discrepancy (about 1%, or 43 seconds of arc per century) of the observed rotational velocity of Mercury's perihelion, as compared to the Newtonian predictions. This discrepancy disappears when applying General Relativity. These observations serve as a test of the theory of general relativity.

1.1.1 Theoretical Basis

Without going into much detail, I now briefly overview some basic aspects of the theory of General Relativity. For more details see, for example, [6] or any other text book in General Relativity. In what follows I use geometrized units, where $c = G = 1$ (see appendix F of [6] for the conversion rules). The standard convention of implicit summation over repeated indices is used, as well as the convention of lowering indices by contracting with the metric tensor and rising them with the inverse metric (see [6]).

The space-time is described in terms of the metric tensor, whose components g_{ab} in arbitrary coordinates $\{x^a\}$ are given by

$$ds^2 = g_{ab} \ dx^a dx^b. \tag{1.1}$$

To obtain the metric we need to solve the Einstein equations, which are given in tensorial form by

$$G_{ab} \equiv R_{ab} - \frac{1}{2}R \ g_{ab} = 8\pi \ T_{ab}, \tag{1.2}$$

where R_{ab} is the Ricci tensor (which contains second order derivatives of the metric), $R \equiv g^{ab} R_{ab}$ and T_{ab} is the stress-energy tensor, that provides the matter contribution to the Einstein's equations. G_{ab} is called the Einstein's tensor. Thus, for example, if one is considering a (real) scalar field, T_{ab} is given by equations (2.1-2.3). Vacuum solutions can be obtained by setting $T_{ab} = 0$, in which case equation (1.2) reduces to $R_{ab} = 0$

In the presence of matter one needs to solve equation (1.2) together with the evolution equations for the matter, that can be obtained from the condition

$$\nabla^a T_{ab} = 0, \tag{1.3}$$

where ∇_a represents the covariant derivative, such that

$$\nabla_a g_{bc} = 0.$$

Despite the simple appearance of Einstein's equations when presented in the tensorial form of (1.2), they are actually a complex system of second order, partial differential equations. Only a few analytical solutions to the Einstein equations are known, which were obtained assuming symmetries that simplify the equations. Remarkably, one of the simpler solutions, obtained after assuming a static, spherically symmetric, vacuum solution, is that of a non-spinning black hole, known as a Schwarzschild space-time. Alternatively, relaxing the conditions to allow for a stationary rather than static solution, one obtains the space-time of a (stationary) spinning black hole, or Kerr space-time. These two solutions can be further generalized to represent a charged black hole, which in the non-spinning case is known as the Reissner-Nordstrom solution. More general solutions of the Einstein equations containing one or more black holes can be obtained numerically, or using other approximation methods (see below). The characteristic that defines a black hole is the existence of an event horizon, which delimits the "exterior" region from a (closed) region from which nothing can escape, not even light, hence the name of black hole.

For clarity, we now consider a concrete example, the Schwarzschild solution for a static black hole space-time. Its metric is given (in Schwarzschild coordinates) as:

$$ds^2 = -\left(1 - \frac{2M}{r}\right) dt^2 + \left(1 - \frac{2M}{r}\right)^{-1} dr^2 + r^2 \left(d\theta^2 + \sin^2\theta \, d\varphi^2\right), \tag{1.4}$$

where M is the mass of the black hole. The event horizon in this case is located at $r = 2M$. Notice that at large distances from the black hole, in the limit $M/r \to 0$, we obtain the metric of flat (Minkowski) space-time in spherical coordinates. The singularity at $r = 2M$ is only a coordinate singularity and can be removed with a change of coordinates (see chapter 2). On the other hand, the singularity at $r = 0$ is a physical singularity. However, since it is located inside the event horizon, it is causally disconnected from the exterior solution. The existence of a singularity inside the event horizon is a common feature of all black hole solutions, and one that needs to be handled properly when performing numerical simulations (see chapters 2 and 4).

We saw some examples of analytical black hole solutions, obtained in special cases where exploiting symmetries greatly simplify the equations. To obtain more general solutions of the Einstein equations containing one or more black holes, one usually needs to solve the equations numerically, or use other approximation methods, and even then the problem may be very challenging. In fact, numerical solutions of a binary black hole merger, to name an important example, have been accomplished for the first time only a few years ago.

In systems where Newtonian gravity is dominant, but there is also some contribution from relativistic gravity, a good approximation can be given by a post-Newtonian expansion. For

instance, the gravitational waves emitted by a binary black hole can be very accurately described by post-Newtonian expansions during the binary's inspiral phase, up to very close to merging (see chapter 3 and references therein).

As another approximation, one can use a perturbative analysis over a known solution, given that the physical system to study is known to present a small deviation from that solution. For example, this technique can be used to study the quasi-normal modes of a perturbed Schwarzschild (or Kerr) black hole, or to study linear perturbations over a Minkowski space-time, which gives rise to solutions corresponding to gravitational waves. See, for instance, [7].

In some cases, one can neglect the contribution to the space-time curvature from a given matter source, and evolve only the matter equations on a fixed space-time background, where the background can be given by a known solution of the Einstein equations. This approximation is known as the Cowling approximation. This approach greatly simplifies the problem. Also, the computing power needed when using this approximation in numerical simulations is reduced significantly. The Cowling approximation is used in chapter 4 when evolving the fluid equations on a Kerr black hole background.

Other scenarios, such as the merger of two black holes, can only be well described by solving numerically the full general relativistic equations without further approximations. In order to solve the Einstein's equations numerically, a particular formulation is used, in which equations (1.2) take the form of a set of hyperbolic equations plus a set of elliptic equations. Given consistent initial data, one can integrate numerically in time the hyperbolic system (evolution equations). Consistent initial data must satisfy the elliptic system (referred as constraint equations). Since this system consists of more variables than equations, some of the variables can be set at will to reflect the particular physical system one wants to describe, and then solve numerically the constraint equations for the rest of the variables to obtain consistent initial data. It can be shown that, if the constraint equations are satisfied initially, then they are automatically satisfied for all times[1]. An example of this procedure is that used in chapter 2 to obtain solutions for a black hole with a scalar field.

1.1.2   Gravitational Waves

One of the most important predictions of the theory of General Relativity is the existence of gravitational waves, since Gravitational Wave Astronomy will make possible a new way of exploring our universe. Gravitational waves can be thought of as ripples in the fabric of space-time, that propagate at the speed of light. They are generated by any accelerated quadrupole (or higher order) mass distribution, though waves strong enough to be detected would only be generated in systems involving very strong curvatures in highly dynamical systems. Examples of sources of gravitational waves that may be detectable are the collision of two black holes or neutron stars, supernova core collapse, and maybe even isolated neuron stars if they present some asymmetry, like an off axis bump on the surface.

As measured by a distant observer, gravitational waves have the effect of weekly distorting the (otherwise flat) space-time, in such a way that the distance between two points grows and shrinks perpendicularly to the direction of propagation as the wave passes by. The relative distance change is called strain, usually denoted by h. As the space-time expands in one direction, it contracts in the perpendicular direction, and vice versa. Gravitational waves can be decomposed

---

[1]However, when evolving the equations numerically, some extra care is needed to ensure the constraints are preserved, and hence one is actually solving the Einstein's equation. For example, by implementing constraint preserving boundary conditions, and monitoring the constraints during the evolution to check that they converge to zero (see chapter 2)

into two polarizations, "plus" (+) and "cross" ($\times$), where the angle between the two polarizations is 45 degrees.

This is usually illustrated with the following example. Consider a circular array of particles, and a gravitational wave with + polarization propagating perpendicularly to the plain of the array. As the wave passes through, the particles will move alternatively away from (towards) the center in the vertical direction, as they move towards (away from) the center in the horizontal direction, deforming the circle into an "oscillating" ellipse, as illustrated in figure 1.2. In the case of a $\times$ polarization, the particles move in the same way, but with the axes of the ellipse rotated 45 degrees on the plane of the array.

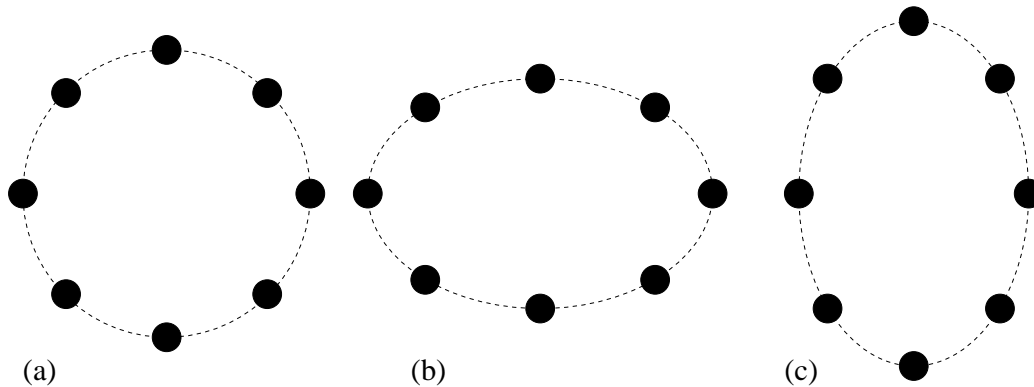(a)   (b)   (c)

Figure 1.2: As a gravitational wave propagates through a circular array of particles, (a), the separation between the particles shrinks (expands) vertically as it expands (shrinks) horizontally, (b) and (c).

One important property of gravitational waves is that they carry away energy and momentum. This implies that in some circumstances the effects of energy or momentum loss through gravitational waves can be observed without actually detecting the radiation. For example, the loss of angular momentum of a binary system will cause the distance between the two bodies to gradually shrink, and the frequency of the orbits to increase. In fact, it was indirectly shown that gravitational radiation exists by observing this effect in a pulsar binary system (PSR B1913+16). The measured change in the orbital frequency of this system is in accordance with the predicted emission of gravitational waves. After thirty years of following this pulsar, astronomers have by now corroborated the agreement with the predictions of general relativity to within about 0.2 percent [8]. Another example is the double pulsar PSR J0737-3039, discovered in 2003, which allowed even more precise testings of general relativity [9], showing agreement up to at least 0.05 percent.

The effect of gravity waves illustrated in figure 1.2 has been exaggerated for clarity, gravitational waves are typically very weak, which makes their detection difficult. For example, the strain of gravitational waves emitted by a pair of stars or black holes of similar mass orbiting each other can be approximated [10], in order of magnitude, by

$$h \approx \frac{G^2 M^2}{c^4 r R} \approx \frac{G^{\frac{5}{3}} M^{\frac{5}{3}} \Omega^{\frac{2}{3}}}{c^4 R}, \tag{1.5}$$

where M is the total mass of the system, r is the orbital radius, R is the distance to the binary and Ω is the orbital angular velocity. This simplified approximation gives, for the particular

case of the binary PSR B1913+16 mentioned in the previous paragraph[2], a maximum amplitude $h \approx 10^{-23}$. The typically small value of the strain is not the only difficulty in the detection of gravitational waves, another factor to take into account is their frequency, since detectors are able to detect waves only on a given frequency range. Despite these difficulties, a large number of known binaries are expected to be detectable by LISA [11].

Of the different possible sources of gravitational radiation, one for which we can make a clear prediction of its gravitational waveform is a binary black hole coalescence. This process can be divided into three distinct phases: inspiral, merger, and ring-down. During the inspiral phase, the binary emission is quasi-periodic. As the radiation takes away energy, the orbits shrink and the frequency and amplitude of the waves continually increase, slowly first, and faster as the black holes get closer. Then the black holes merge, emitting a burst of gravitational radiation. After merger, the resulting black hole vibrates as it settles down to a stationary state, during this ring-down phase the gravitational waves decay exponentially.

Though gravitational waves have not been detected yet, some gravitational wave observatories have already begun operation, like LIGO [1], GEO [12] and VIRGO [3]; and more are being built or are planed for the future, like LISA [13]. Some of these observatories are sensitive to completely different frequencies, complementing each other. For instance, LIGO's range of sensitivity (about 10 to 10^4 Hz, with a peak sensitivity around 150Hz) is suitable for detecting waves generated in collisions of medium-mass black holes and neutron stars, while LISA will be sensitive to lower frequencies (as low as about 10^{-4} Hz), suitable for detecting super-massive black hole mergers. The frequency difference between the mentioned sources is explained by the fact that the gravitational wave frequency is proportional to the inverse of the source's mass. On the other hand, some detectors operate in similar frequency ranges, like for example the two LIGO observatories, VIRGO and GEO. In this case, since they are located far away from each other, their observations can be contrasted to rule out any false positives caused by local sources, as well as triangulated to determine the location of the gravitational wave sources.

---

[2]Notice that in equation 1.5 we assume optimal orientation and polarization for detection (which is not the case with PSR B1913+16), for more general cases the strain would actually be smaller

Chapter 2
Scalar Field Confinement in General Relativity

In this chapter we investigate the possibility to localize scalar field configurations surrounding a black hole. We analyze and resolve difficulties encountered when localizing scalar fields in General Relativity. We illustrate this ability with a simple spherically symmetric model which can be used to study features of accreting shells around a black hole. This is accomplished by prescribing a scalar field with a coordinate dependent potential. Numerical solutions to the Einstein equations coupled to a Klein-Gordon-like field are shown, where a scalar field is indeed confined within a region surrounding a black hole. The resulting spacetime can be described in terms of simple harmonic time dependence. The work shown in this chapter resulted in a publication [14].

2.1   Introduction

Self-gravitating scalar field configurations have been very useful in many aspects of gravitational theory. Their role as describing matter models (eg.[15, 16, 17, 18, 19, 20]); as governing mechanisms to model inflationary scenarios (eg. [21, 22]); as probes of strong curvature regions (eg.[23, 24]), etc., has made them an ideal tool in a number of fronts.

In this chapter, we examine confining a self gravitating scalar field to a given region of spacetime. We concentrate, in particular, to confining the field to a region surrounding a black hole, which can be useful for mimicking some properties of accreting black hole systems using a simple scalar field model. Since normally a scalar field would fall into the black hole and/or radiate away to infinity, the model should include a mechanism that will prevent this from happening, at least to some non-trivial extent.

One way to confine the scalar field would be by employing a potential well which would introduce some sort of barrier and thus allow for confinement. The use of carefully chosen potentials is common practice with scalar fields, and are usually functions of the field itself. Examples of this kind of potential are the quadratic ($V(\phi) \propto \phi^2$) –that introduces a mass term–; and the quartic ($V(\phi) \propto \phi^4$). However, that kind of potential does not allow for confining the scalar field within a specific region of space, that one can specify *a priori.*

What we are looking for is a potential that somehow depends on the coordinates and in particular can be chosen to describe a potential well within a region. However, this proposition seems a priori imposible without breaking the covariance of the theory. A difficulty one encounters with a coordinate-dependent potential, is that the corresponding stress-energy tensor is in general inconsistent, in the sense that its divergence will not be zero for a non-trivial scalar field. This fact, together with the Einstein equations, would imply that the Bianchi identities (a well known property of the Riemann tensor) are not satisfied [6].

Faced with this situation, a possible way of confining the scalar field is to exploit symmetry considerations. The existence of the symmetry provides a simple way to consistently introduce a coordinate-dependent potential in the problem. A particular case of a coordinate dependent

potential has already been implemented in [25, 26] to effectively simulate angular momentum in spherical or axial symmetry.

We concentrate mainly on the case of spherical symmetry, but give prescriptions for the implementation of potentials in both spherical and axial symmetry. We will see that, if the space is spherically symmetric, we can implement a potential that depends on the areal radius (defined as r such that $A = 4\pi r^2$ is the area of the sphere labeled by $r = const.$). In the same way, for an axially symmetric spacetime, the potential can depend on the length of the closed integral curves defined by the associated killing vector [6]. Notice that, since the potential will be chosen to depend only on coordinates that are defined by physical properties of the system, the covariance will not be broken.

Even though one will not be able to specify the potential as an arbitrary function of *any* coordinate, one may still be able to confine a scalar field to some region, as we show later for the case of spherical symmetry. This fact will become apparent in section 2.2.1 and in its applications in the rest of this chapter.

This chapter is organized as follows. In section 2.2, we study the specification of a stress-energy tensor for a scalar field with a coordinate dependent potential. Showing that such implementation is possible when the space-time possesses a symmetry. In particular, the case of spherical symmetry is studied in depth (we also consider an axi-symmetric case in section 2.7.1). In section 2.3 we describe the formulation used, and the resulting equations. In section 2.4 we discuss how the equations are solved numerically, after obtaining initial data by two different methods. In section 2.5 we show and analyze the numerical solutions obtained, finding that, after some transient behavior, the scalar field reaches a state described by a simple harmonic time dependence and remains confined to a region surrounding the black hole. We have confirmed these for initial masses of the scalar field up to 50% of that of the black hole. Finally, we make some final remarks in section 2.6. In all this chapter we use Einstein's index notation, where a repeated index imply summation over its possible values, and we lower and rise indices by contracting with the metric and inverse metric, respectively. We also use geometrized units, where $G = c = 1$.

2.2 Scalar Field on a Coordinate-Dependent Potential

In this section we study the specification of a stress-energy tensor for a scalar field with a coordinate dependent potential. Our motivation is to confine a scalar field within a region around a black hole. We will see that this can be done when the space-time possesses a symmetry. However, the specification of such potential is not completely arbitrary since it must depend on the coordinates only through some particular function. Knowing the approximate dependence of that function on the coordinates, one can then construct a potential that confines the scalar field.

Before presenting our approach, we include an overview of how the equations of motion are obtained from a stress-energy tensor in the case of a coordinate-independent potential. Then, based on that procedure, we will study the generalization to the case of a coordinate-dependent potential.

The equations of motion for a real scalar field ϕ on a coordinate-independent potential can be derived from the stress-energy tensor

$$T_{ab} = T^{(k)}{}_{ab} + T^{(p)}{}_{ab}, \tag{2.1}$$

where, for later convenience, we have split this tensor into what we call the "kinetic" and

"potential" terms:

$$T^{(k)}{}_{ab} \equiv (\nabla_a \phi)(\nabla_b \phi) - \frac{1}{2} g_{ab} (\nabla_c \phi)(\nabla^c \phi), \tag{2.2}$$

$$T^{(p)}{}_{ab} \equiv -\frac{1}{2} g_{ab} V(\phi). \tag{2.3}$$

The kinetic part, $T^{(k)}{}_{ab}$, corresponds to a massless scalar field without a potential.

The equations of motion can be obtained [6, 15] through the condition

$$\nabla_a T^a{}_b = 0 , \tag{2.4}$$

Equation (2.4) can be re-expressed with $\nabla_b \phi$ as a common factor,

$$0 = \nabla_a T^a{}_b = (\nabla_b \phi) \, \mathcal{L}(\phi), \tag{2.5}$$

where $\mathcal{L}(\phi)$ contains second order derivatives of ϕ. The equations of motion for a non-trivial scalar field is then

$$\mathcal{L}(\phi) = 0 . \tag{2.6}$$

For example, for $V(\phi) = m^2 \phi^2$ we obtain the Klein-Gordon equation,

$$\mathcal{L}(\phi) \equiv \left(\nabla_a \nabla^a - m^2 \right) \phi = 0 . \tag{2.7}$$

This is analogous to the Lagrangian approach, where the variation of the action is set to zero, and, after integrating by parts, the integrand becomes $\delta \phi \mathcal{L}(\phi)$.

After this detour, we now turn our attention back to the case of interest, the implementation of a coordinate-dependent potential. Our discussion is based on the preceding one though now generalizing it to the case of a coordinate-dependent potential $V(x^c, \phi)$.

A naive first approach would be to replace occurrences of $V(\phi)$ in (2.3) by $V(x^c, \phi)$. However, this will bring an unfortunate consequence, namely that one can now no longer express the divergence of $T^a{}_b$ in the form given by eqn (2.5), where $\nabla_b \phi$ appears as a common factor. Instead one has

$$\begin{aligned} 0 = \nabla_a T^a{}_b &= (\nabla_b \phi) \left(\nabla_a \nabla^a \phi - \frac{1}{2} \frac{\partial}{\partial \phi} V(x^c, \phi) \right) \\ &\quad - \frac{1}{2} \frac{\partial}{\partial x^b} V(x^c, \phi). \end{aligned} \tag{2.8}$$

The crucial difference with eqn. (2.5) is that several (independent) equations must be satisfied by the real scalar field ϕ. As a result, the system of equations will be generically inconsistent.

To resolve this problem we start by: (i) adopting a different ansatz for $T^{(p)}{}_{ab}$ (equation (2.9) below), and (ii) imposing symmetry conditions on the scalar field.

First, consider setting $T^{(p)}{}_{ab}$, instead of being given by equation (2.3), to be the product of a function of ϕ and a coordinate dependent tensor,

$$T^{(p)}{}_{ab} \equiv H_{ab}(x^c) \, f(\phi), \tag{2.9}$$

where the function f is independent of x^c and the tensor H_{ab} is independent of ϕ. Now, find a suitable H_{ab} such that $\nabla_a T^a{}_b$ takes the form of equation (2.5), this will induce conditions on H_{ab}. Under this choice the divergence of the stress-energy tensor results

$$\nabla_a T^a{}_b = (\nabla_b \phi) \nabla_a \nabla^a \phi + \frac{\partial f}{\partial \phi} (\nabla_a \phi) \, H^a{}_b + f(\phi) \, \nabla_a H^a{}_b . \tag{2.10}$$

11

Now, we look for conditions that would allow us to express the *r.h.s.* of equation (2.10) in such a way that $\nabla_b \phi$ appears as a common factor. Since $H^a{}_b$ is independent of ϕ, $\nabla_b \phi$ cannot appear in the last term of (2.10); Then, that term must be zero, resulting in the first condition on $H^a{}_b$,

$$\nabla_a H^a{}_b = 0 . \tag{2.11}$$

We now consider the second term in the *r.h.s.*; the condition

$$(\nabla_a \phi) \, H^a{}_b = (\nabla_b \phi) \, h(x^c) , \tag{2.12}$$

for some scalar $h(x^c)$, ensures that that term has $\nabla_b \phi$ as a common factor. Equation (2.12) is satisfied for any scalar field ϕ if

$$H^a{}_b = h(x^c) \delta^a{}_b . \tag{2.13}$$

However, this condition, together with equation (2.11), implies that $h(x^c)$ is a constant. This means that $T^{(p)}{}_{ab}$ is of the form (2.3) (with V independent of x^c). Thus, for an arbitrary scalar field, and without any further structure in the spacetime, space-dependent potentials can not be considered.

However, by imposing further conditions on the scalar field ϕ, $H^a{}_b$ can indeed be chosen with further structure than that of equation (2.13) while still satisfying equation (2.12). To this end, we consider[1] the tensor $H^a{}_b$ of the form

$$H^a{}_b = h(x) \delta^a{}_b + A^a{}_b . \tag{2.14}$$

Replacing (2.14) into (2.12) we find

$$(\nabla_a \phi) A^a{}_b = 0 . \tag{2.15}$$

The simplest case is the one with $A^a{}_b = 0$ for which $H^a{}_b$ is given by (2.13). More general cases arise when ϕ is independent on one of the coordinates, lets say $\partial_{x^3} \phi \equiv \nabla_3 \phi = 0$. Here one can adopt $A^3{}_3$ arbitrarily and set all other components to zero, thus satisfying equation (2.15).

In this particular case, $H^a{}_b$ takes the form

$$H^a{}_b = \begin{bmatrix} h & 0 & 0 & 0 \\ 0 & h & 0 & 0 \\ 0 & 0 & h & 0 \\ 0 & 0 & 0 & b \end{bmatrix} \tag{2.16}$$

for some functions $h(x^c)$ and $b(x^c)$.

Similarly, when ϕ does not depend on two of the coordinates, lets say $\partial_{x^2} \phi = 0$, $\partial_{x^3} \phi = 0$, one can choose

$$H^a{}_b = \begin{bmatrix} h & 0 & 0 & 0 \\ 0 & h & 0 & 0 \\ 0 & 0 & b & 0 \\ 0 & 0 & 0 & c \end{bmatrix} . \tag{2.17}$$

Analogous results are obtained when some of its derivatives are linearly related. For example, if $\partial_{x^3} \phi = c \partial_{x^2} \phi$, one can adopt $A^3{}_3$ arbitrarily and set $A^2{}_3 = -c A^3{}_3$ keeping all other components zero. With this choice, equation (2.15) will be satisfied and $H^a{}_b$ will then be given in terms of two functions $h(x^c)$ and $b(x^c)$ in a slightly different way as is (2.16).

---

[1]This equation can be thought as the definition of the tensor $A^a{}_b$.

Summarizing, we have seen that a coordinate dependent potential can be implemented if the following conditions are satisfied: (i) its derivatives are linearly dependent (this includes the possibility of one or more of them being zero). (ii) The "potential" part of the stress-energy tensor is given by (2.9), with $H^a{}_b$ satisfying $\nabla_a H^a{}_b = 0$ and being expressible in the form (2.16), (2.17), or similar expressions depending on how condition (i) is fulfilled.

In the next section we will consider in detail the case of spherical symmetry.

2.2.1 Spherical Symmetry

We will now concentrate on the case of spherical symmetry. The line element can be written in the form

$$ds^2 = -N^2 dt^2 + g_{rr}(dr + \beta dt)^2 + g_\Omega d\Omega^2, \tag{2.18}$$

where N, g_{rr}, β, and g_Ω are functions of t and r. We adopt coordinates so that $\partial_\theta \phi = \partial_\varphi \phi = 0$. Then, $H^a{}_b$ is given by (2.17), with the additional condition that $b = c$ due to the spherical symmetry. $H^a{}_b$ is then

$$H^a{}_b = \begin{bmatrix} h & 0 & 0 & 0 \\ 0 & h & 0 & 0 \\ 0 & 0 & b & 0 \\ 0 & 0 & 0 & b \end{bmatrix}, \tag{2.19}$$

with h and b functions of t and r.

The evaluation of $\nabla_a H^a{}_b$ gives rise to non-trivial equations only in the t and r components,

$$\frac{dg_\Omega}{dt}(h - b) + 2g_\Omega \frac{dh}{dt} = 0, \tag{2.20}$$

$$\frac{dg_\Omega}{dr}(h - b) + 2g_\Omega \frac{dh}{dr} = 0. \tag{2.21}$$

In order to obtain a family of solutions to these equations we will demand that h depends on the coordinates only through g_Ω: $h(t,r) = h(g_\Omega(t,r))$. With this condition, we have that

$$\frac{dh}{dx^i} = \frac{\partial h}{\partial g_\Omega} \frac{dg_\Omega}{dx^i} \tag{2.22}$$

for $x^i = (t, r)$. Substituting this into either equation (2.20) or (2.21), we obtain an expression for b in terms of h,

$$b = h + g_\Omega \frac{\partial h}{\partial g_\Omega}. \tag{2.23}$$

We have just seen that, if h depends on the coordinates only through g_Ω, and b is given in terms of h by (2.23), the prescription (2.19) for the tensor $H^a{}_b$ allows us to express $\nabla_a T^a{}_b$ with $\nabla_b \phi$ as a common factor. More explicitly:

$$\nabla_a T^a{}_b = (\nabla_b \phi) \left(\nabla_a \nabla^a \phi + \frac{\partial f}{\partial \phi} h(g_\Omega) \right). \tag{2.24}$$

Notice that, if one wanted to calculate $\nabla_a T^a{}_b$ without setting $\partial_\theta \phi = \partial_\varphi \phi = 0$ at the onset, one would obtain (2.24), but with $h(g_\Omega)$ replaced by $b(g_\Omega)$ for the angular components $\nabla_a T^a{}_\theta$ and $\nabla_a T^a{}_\varphi$. However, because those terms are actually multiplied by zero, equation (2.24) is true for all four components.

Setting the *r.h.s* of (2.24) to zero we obtain the equation of motion for ϕ,

$$\nabla_a\nabla^a\phi + \frac{\partial f}{\partial \phi}h(g_\Omega) = 0, \tag{2.25}$$

where we remind the reader that f is an arbitrary function of ϕ, and h is an arbitrary function of g_Ω.

Throughout the rest of this chapter we will choose these functions as

$$f(\phi) \;=\; -\frac{1}{2}\phi^2, \tag{2.26}$$

$$h(g_\Omega) \;=\; m^2 + V(g_\Omega). \tag{2.27}$$

With this choice, the equation of motion for the scalar field becomes

$$\left(\nabla_a\nabla^a - m^2 - V(g_\Omega)\right)\phi = 0, \tag{2.28}$$

where we interpret the function $V(g_\Omega(t,r))$ as a coordinate-dependent potential. The function $g_\Omega(t,r)$ is just the square of the areal radius, $R(t,r)$. Then, we can write (2.28) in the form

$$\left(\nabla_a\nabla^a - m^2 - \tilde{V}(R)\right)\phi = 0, \tag{2.29}$$

where $\tilde{V}$ is an arbitrary function of the areal radius. The term $m^2\phi$ is actually redundant, since it can be absorbed in the definition of the potential V, to which we can always add a constant m^2, so we simply set the parameter m to zero in our simulations.

It is worth emphasizing that the potential can be chosen (if not as a function of r) as a completely arbitrary function of $R(t,r)$. This fact is exploited later to define a potential well that does confine the scalar field.

For the case of axial symmetry one can proceed analogously. We summarize the results obtained in that case in section 2.7.1.

2.3 Formulation of the Equations

In this chapter we solve the non-vacuum Einstein equations for a dynamic spherically symmetric space time, coupled to a real scalar field. The scalar field satisfies a Klein-Gordon-like equation with the addition of a potential, as explained in section 2.2.1.

The equations are decomposed using a Cauchy formulation, in which the space-time is foliated by space-like surfaces. The particular formulation used is the Einstein-Christoffel hyperbolic formulation [27], where the equations are decomposed into a system of (first order in space and time derivatives) hyperbolic "evolution equations," plus a system of (first order in space derivatives) "constraint equations." These equations can be solved by giving initial data that satisfy the constraint equations on a given surface of the foliation, and then integrating the evolution equations in time. The constraint equations at later times are then automatically satisfied [6] in the domain of dependence of that surface.

The equations solved are the Einstein-Klein-Gordon equations, with the addition of a potential,

$$G_{ab} = 8\pi T_{ab} \qquad , \tag{2.30}$$

$$\left(\nabla_a\nabla^a - V\right)\phi = 0 \quad , \tag{2.31}$$

where the stress-energy tensor, T_{ab}, and the potential, V, are given according to section 2.2.1, as well as the condition that ϕ is independent of (θ, ϕ). In equation (2.31) we have set $m = 0$, but, as mentioned, this parameter can be incorporated in the definition of V.

We consider the line element and extrinsic curvature of a space time in spherical symmetry in the form

$$ds^2 = -N^2 dt^2 + g_{rr}(dr + \beta dt)^2 + r^2 g_T d\Omega^2, \tag{2.32}$$

$$K_{ij} dx^i dx^j = K_{rr} dr^2 + r^2 K_T d\Omega^2, \tag{2.33}$$

where β is the (r component of the) shift vector, and N is the lapse function. In the Einstein-Christoffel formulation, the shift and "densitized lapse" function, $\alpha \equiv N/\sqrt{g}$, are arbitrarily specified and kept fixed during the evolution. We denote by g the determinant of the three-metric.

In spherical symmetry, this system reduces to nine first order evolution equations, and four first order constraint equations, the later containing only spatial derivatives.

The variables evolved are: the metric components, g_{rr} and g_T; the scalar field, ϕ; and other variables used to convert the equations from second to first order. They are: the extrinsic curvature components, K_{rr} and K_T (defined in eqn.(2.33)); variables $\{\Psi, \Pi\}$ constructed with first-derivatives of ϕ,

$$\Psi = \partial_r \phi, \tag{2.34}$$

$$\Pi = \frac{1}{N}\left(\beta\, \partial_r \phi - \partial_t \phi\right); \tag{2.35}$$

and the variables $\{f_{rrr}, f_{rT}\}$ containing first spatial derivatives of the metric,

$$f_{rrr} = \frac{\partial_r g_{rr}}{2} + \frac{4 g_{rr} f_{rT}}{g_T}, \tag{2.36}$$

$$f_{rT} = \frac{\partial_r g_T}{2} + \frac{g_T}{r}. \tag{2.37}$$

The complete expressions of these equations are shown in detail in section 2.7.2. Their derivation, and the notation used, is based on [28] and [29], with the addition of terms containing the potential.

2.4 Numerical Implementation

2.4.1 Initial Data

As explained in chapter 1, consistent initial data must satisfy equations (2.82)-(2.86). These equations determine some variables in terms of others judiciously chosen. We exploit this freedom to describe a black hole centered at $r = 0$ by specifying $\{V, \phi, g_{rr}, K_{rr}\}$ from the known Schwarzschild solution and solving for g_T and K_T.

Before describing the details of our implementation, we discuss how the potential and scalar field are chosen. We adopt a potential V with two free parameters $\{A, r_0\}$ to regulate the depth and location of the "well" where the scalar field is to be confined (see figure 2.1). A simple expression for V suffices for this task, and we adopt

$$V(R) = A\left(1 - e^{-(R-r_0)^2}\right), \tag{2.38}$$

with the areal radius R given by $R = r\sqrt{g_T}$. The parameters in this expression were set to $A = 30/M^2$ and $r_0 = 6M$, where M is the initial mass of the black hole. Notice that during the evolution $R = R(t, r)$, thus, in these coordinates, the shape (and position) of the potential well can change in time. We will return to this point later.

The scalar field ϕ is defined following either one of two different strategies. One is designed to conform to time-harmonic situations in weakly-gravitating cases and the other simply prescribing a sufficiently smooth profile. The latter choice allows us to investigate the spacetime's response to fields not designed to conform to a time-harmonic dependence.

● Time-Harmonic Scalar Field

To prescribe a scalar field which will give rise to a spacetime with harmonic time-dependence, we begin by considering the limiting case when the scalar field's amplitude is negligible; there the metric should be described by the Schwarzschild's solution. Now, considering the scalar field as existing over this fixed background spacetime, a Schrödinger-like eigenvalue equation can be obtained to determine time-harmonic states as discussed below.

The Schwarzschild metric in Eddington-Finkelstein coordinates is:

$$ds^2 = - \left(1 - \frac{2M}{r} \right) dt^2 + \left(1 + \frac{2M}{r} \right) dr^2 + \frac{4M}{r} dtdr + r^2 d\Omega^2. \tag{2.39}$$

We use this metric to evaluate the equation of motion for ϕ, equation (2.31). To solve this partial differential equation (PDE) we use the following ansatz that yields separation of variables[2],

$$\phi(t, r) = u(r) \cos\left(\omega \left[t - 2M \ln \left(\frac{r - 2M}{M} \right) \right] \right). \tag{2.40}$$

The equation for $u(r)$ results

$$\mathcal{L} u(r) = \left[\omega^2 - \left(1 - \frac{2M}{r} \right) V(r) \right] u(r), \tag{2.41}$$

where the second order operator $\mathcal{L}$ is given by

$$\mathcal{L} = - \left(1 - \frac{2M}{r} \right)^2 \frac{\partial^2}{\partial r^2} - \frac{2}{r} \left(1 - \frac{M}{r} \right) \left(1 - \frac{2M}{r} \right) \frac{\partial}{\partial r} \tag{2.42}$$

Equation (2.41) is integrated to obtain $u(r)$. Then, from its definition, equation (2.40), $\phi(t, r)$ is calculated. Finally, from $\phi(t, r)$ we obtain $\Pi(t, r)$ and $\Phi(t, r)$ evaluating these functions at $t = 0$ and adopting them as initial data.

Equation (2.41) can be straightforwardly integrated to obtain both the eigenvalue and eigenfunction through a standard shooting algorithm. To this end, we transform the second-order equation to a system of two first order equations for $u(r)$ and $u'(r) \equiv du/dr$ augmented with a third equation $((\omega^2)' = 0)$ to simplify the implementation (see [30] for the details).

The system of equations is then integrated outwards from $r_L \equiv 4M$ on one hand, and also inwards from $r_R \equiv 8M$. The obtained solutions are matched at an intermediate point, in our case at r_0 (the center of the potential well), with the conditions that both the solutions and derivatives are continuous. The initial guesses for the boundary conditions are then varied until

---

[2]Suggested by the fact that in Schwarzschild coordinates, $(\tilde{t}, \tilde{r})$, the ansatz $\phi = u(\tilde{r}) \cos(\omega \tilde{t})$ yields separation of variables. The coordinates transformation being: $\tilde{t} = t - 2M \ln \left(\frac{r-2M}{M} \right)$, $\tilde{r} = r$.

a satisfactory match is obtained. The code used to implement the shooting algorithm is the one described in [30], except that the ODE integrator is replaced for LSODE (Livermore Solver for ODEs) [31]. The boundary conditions, consistent with the physical scenario in mind are determined as follows.

We have a system of three first order ordinary differential equations (ODE), thus three boundary conditions need be specified. Natural conditions for our purposes result from requiring that the fields fall sufficiently rapidly at the boundaries. We thus impose a relationship between u and its derivative at each boundary, of the form $u' = ku$. The coefficient k at each boundary can be found through a WKB-type approach. To do so, we first consider the variable change $u(r) \equiv F(r)\tilde{u}(r)$ and fix $F(r) = [r(r - 2M)]^{-\frac{1}{2}}$ so as to remove the first order derivative in equation (2.41). The resulting equation is

$$-f(r)\tilde{u}''(r) + V_{\text{eff}}(r)\tilde{u}(r) = \omega^2 \tilde{u}(r) \tag{2.43}$$

with $f(r)$ and $V_{\text{eff}}(r)$ given by

$$f(r) = \left(1 - \frac{2M}{r}\right)^2, \tag{2.44}$$

$$V_{\text{eff}}(r) = \left(1 - \frac{2M}{r}\right) V(r) - \frac{M^2}{r^4}, \tag{2.45}$$

and we interpret V_{eff} as an effective potential (which is shown in figure 2.1). Next, we freeze the
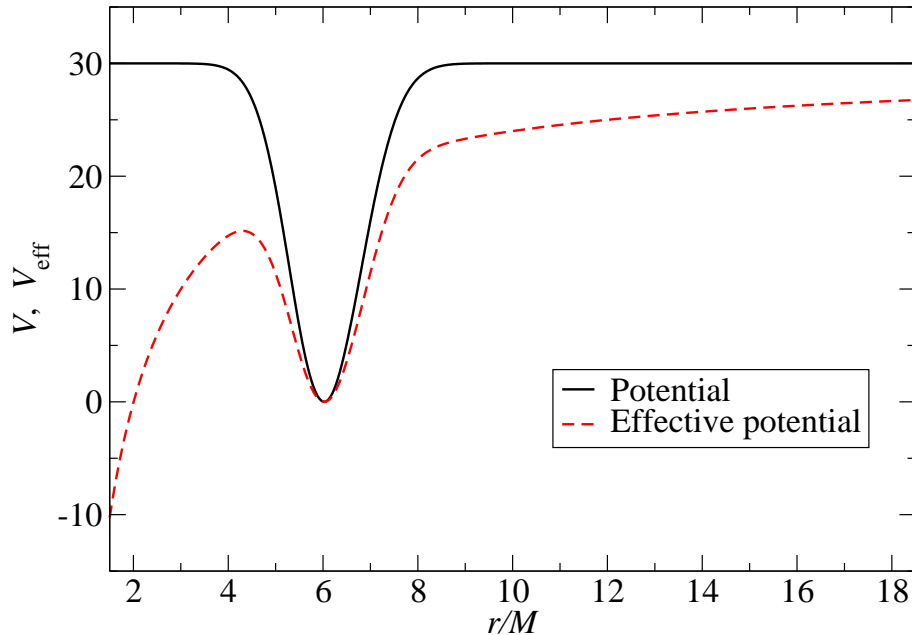
Figure 2.1: Potential and effective potential, as defined in (2.38) and (2.45), respectively. As mentioned in the text, the potentials are, in general, functions of $R \equiv r\sqrt{g_T}$. The potentials showed in this figure are those used to find the time harmonic states $u(r)$, where the Schwarzschild metric is used, hence $R = r$.

coefficients $f(r)$ and V_{eff} on a small neighborhood of each boundary point and consider solutions of the form $\exp(\pm kr)$, with $k^2 = (V_{\text{eff}} - \omega^2)/f$. The conditions at the boundaries are then

determined by

$$\tilde{u}(r) \propto e^{+k_1 r} \quad \text{at} \quad r = r_L, \tag{2.46}$$

$$\tilde{u}(r) \propto e^{-k_2 r} \quad \text{at} \quad r = r_R, \tag{2.47}$$

where

$$k_1 = \sqrt{\frac{V_{\text{eff}}(r_L) - \omega^2}{f(r_L)}}, \tag{2.48}$$

$$k_2 = \sqrt{\frac{V_{\text{eff}}(r_R) - \omega^2}{f(r_R)}}. \tag{2.49}$$

As illustrated later, these conditions indeed ensure the solutions decay rapidly outside of the potential well (for a bounded range of values of ω^2). Notice that since the equations are homogeneous there remains a freedom on the amplitude of the fields at the boundaries. We fix this freedom by setting $u = 1$ at r_L and adopting as the varying parameter for the shooting method the value of u at r_R.

Once obtained $\phi(r)$ in $[r_L, r_R]$ using equation (2.40), we set $\phi(r) = 0$ outside this region. For the amplitude of ϕ used in the case of time-harmonic initial data, the values of ϕ and its derivative at r_L and r_R are small enough to ensure that this matching is sufficiently smooth, as is corroborated when evolving these initial data.

● Smooth Profile Scalar Field

The other approach employed is to adopt a simple expression for the scalar field. In particular we adopt a "pulse" of compact support of the form

$$\phi(r) = \begin{cases} c(r - r_1)^4(r - r_2)^4 & r_1 \leq r \leq r_2 \\ 0 & \text{elsewhere} \end{cases}, \tag{2.50}$$

where the values r_1 and r_2 control the width of the pulse and were chosen so that it is centered with the potential (at $r = 6M$): $r_1 = 5M$, $r_2 = 7M$. After specifying r_1 and r_2, the coefficient c is chosen so that the scalar field has a given mass. This initial data is used to compare with the previous approach in regimes where the fixed-background approximation is justified and to study the spacetime's behavior in non-linear cases.

● Space-Time Initial Data

Having specified both the potential and the scalar field, consistent initial data is determined by integrating the constraint equations in the following manner. First, the functions g_{rr}, K_{rr}, α, and β are set equal to those read-off from the Schwarzschild solution in Eddington-Finkelstein coordinates. Adopting these coordinates gives the freedom to place the inner boundary inside the black hole. We found it convenient to rewrite the constraint equations in the form:

$$\partial_r g_T = d_T, \tag{2.51}$$

$$\partial_r d_T = f_1(g_T, d_T, K_T; F_i), \tag{2.52}$$

$$\partial_r K_T = f_2(g_T, d_T, K_T; F_i), \tag{2.53}$$

where F_i represents all the functions that are specified a priori (including ϕ). These equations are integrated outwards from the inner boundary using the step adaptive integrator LSODE, using as boundary data (g_T, d_T, and K_T at $r = r_{\min}$) the values read-off from the Schwarzschild solution.

2.4.2 Evolution

We discretize the equations with a scheme formulated to take advantage of numerical techniques which guarantee stability of generic linear first order hyperbolic systems. We adopt: (i) second order accuracy by implementing second-order derivative operators satisfying summation by parts [32, 33, 34, 35, 36]; (ii) a third-order Runge-Kutta operator for the time integration through the method of lines [37]; (iii) a Kreiss-Oliger [38] style dissipative algorithm to control the high frequency modes of the solution [39, 36, 40] and (iv) maximally dissipative boundary conditions setting all incoming modes to zero [41, 42, 43, 39].

We employ a uniform grid to cover the region $r \in [r_{\min}, r_{\max}]$ with N equi-spaced points. The grid-spacing between points is $\Delta r = (r_{\max} - r_{\min})/(N-1)$. The time step Δt is defined in terms of Δr as $\Delta t = cfl\,\Delta r$ and $cfl = 0.25$ is chosen so that the CFL condition [44] is satisfied. In what follows, sub-indices denote particular points of a slice, and super-indices distinguish each slice.

The inner boundary, $r = r_{\min}$, is set inside the black hole initially, and monitored during the evolution to ensure that it remains inside and constitutes an outflow boundary of the computational domain. Then, there is no need to prescribe boundary conditions there. At the outer boundary, $r = r_{\max}$, we adopt boundary conditions in which the incoming modes are set to zero. The characteristic structure for the system of equations is detailed in section 2.7.3.

The codes have been tested to ensure that the numerical solutions obtained converge to the corresponding solutions of the Einstein equations. In section 2.7.4 we show the convergence test for the Hamiltonian constraint.

2.5 Analysis and Results

In the simulations performed in this work we set the initial mass of the black hole to $M = 1$ (in geometrized units). The domain of integration was chosen so that the region of interest is unaffected by the conditions adopted at the right boundary. This corresponds to $r_{\min} = 1M$ and $r_{\max} = 221M$. The maximum resolution used was $\Delta r = 0.01M$ (22000 grid points).

In the two approaches we use to obtain initial data, we have the freedom of adjusting the amplitude of the scalar field, which in turn determines its mass. We set initial data where the mass of the scalar field is $m_{\rm sf} = 0.01M$ in the time-harmonic case, while for the non-time-harmonic cases we set $m_{\rm sf}$ equal to $0.01M$, $\kappa\,0.1M$, (M being the initial mass of the black hole and $\kappa = 1...5$). To calculate the mass we use the Misner-Sharp formula [15],

$$M_{\rm MS}(r) = \frac{r\sqrt{g_T}}{2} \left[1 + \frac{r^2}{g_T} \left(K_T^2 - \frac{f_{rT}^2}{g_{rr}} \right) \right], \tag{2.54}$$

which measures the total mass inside a spherical surface labeled by coordinate r. In our initial data the mass of the black hole, M, is preset, so we can calculate $m_{\rm sf}$ by subtracting M from the total mass of the space-time,

$$m_{\rm sf} = M_{\rm MS}(R) - M, \tag{2.55}$$

where R labels a sphere containing the scalar field, which is localized initially. (See figure 2.8). During the evolution we employ this formula, replacing M for $M_{\rm MS}$ at the horizon[3].

---

[3]The position of the apparent horizon is given by the outermost trapped surface.

In our analysis we also evaluate (see discussion at the end of section 2.5.2) the Kretschmann invariant $I \equiv R_{abcd}R^{abcd}$, where R_{abcd} is the Riemann tensor. This quantity provides a gauge-invariant curvature quantity that can be compared with its value in known spacetimes. For a Schwarzschild space-time, I is given by

$$I_{\mathrm{Sch}} = \frac{48(M_{\mathrm{MS}})^2}{R^6}, \tag{2.56}$$

where, in Schwarzschild coordinates, $M_{\mathrm{MS}} = M$ and $R = r$. We evaluate the quotient I/I_{Sch} using (2.56) with $R = r\sqrt{g_T}$ and M_{MS} defined in (2.54).

2.5.1   Initial Data

As explained in section 2.4.1, we first find time-harmonic states for the scalar field on a Schwarzschild space-time. By varying the initial guess for the frequency in the shooting integration we obtain different modes. We show the first modes in figures 2.2 and 2.3. However, for this work we used only the first mode which will be referred to as "the time-harmonic state", unless otherwise specified. These modes have been re-scaled so that they can be normalized (in analogy with quantum mechanics) so that $\int r^2 |u(r)|^2 dr = 1$. There is no physical justification for choosing that particular normalization, but it is helpful when comparing different eigenstates, which otherwise would have greatly different amplitudes.
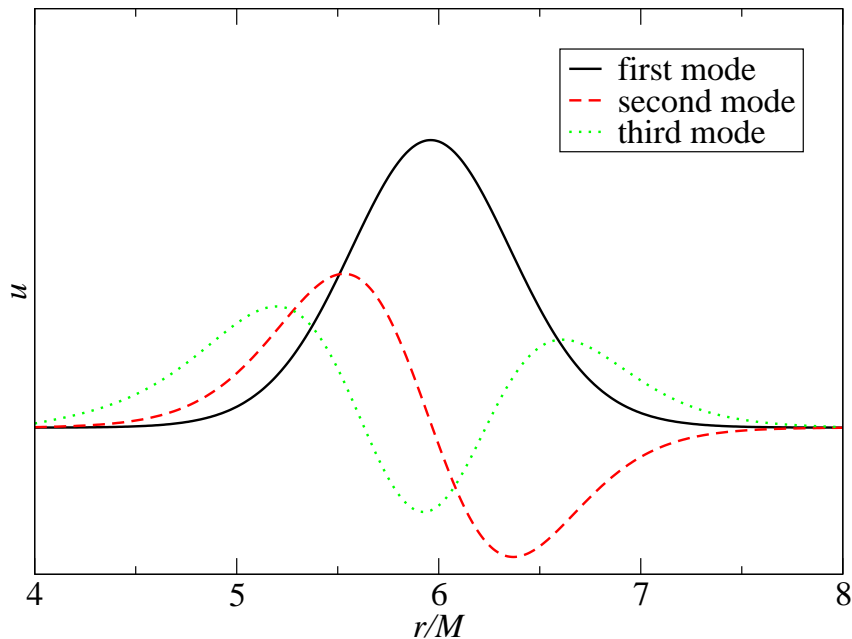
Figure 2.2: First time-harmonic states of $u(r)$.

The other approach used to define the initial data corresponds to the "pulse" described in section 2.4.1. In the linear regime we employ both types of initial data, with a scalar field's initial mass $m_{\mathrm{sf}} = 0.01M$. In the non-linear regime we adopt only the non-time-harmonic initial data with masses m_{sf} ranging from $0.1M$ to $0.5M$.
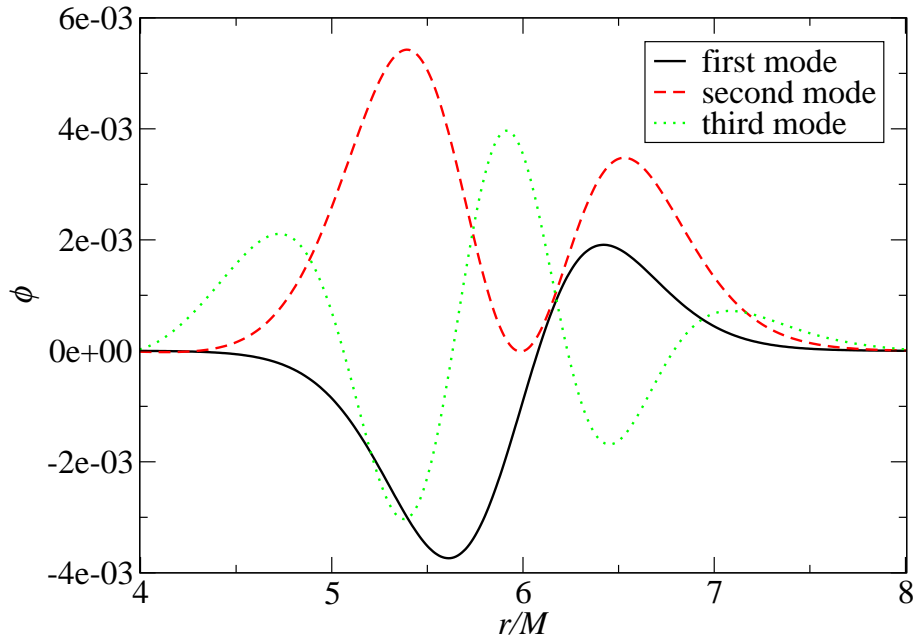
Figure 2.3: Scalar field at $t = 0$ obtained from the first time-harmonic states of $u(r)$, using equation (2.40).

2.5.2 Evolution

We study the evolution of the prescribed data. We begin by considering first the linear regime, adopting scalar field configurations with initial mass of 1% of that of the black hole. After confirming that the time-harmonic configuration behaves as expected, we confirm that the "pulse" configuration evolves towards a time-harmonic regime. Then, we study cases in the non-linear regime, with initial scalar field masses ranging from 10% to 50% of that of the black hole. In all cases we evolve until $t = 200M$.

• **Linear Case**

The time-harmonic initial data constructed essentially remains unchanged through the evolution while the non-time-harmonic data evolves towards a time-harmonic state. Figures 2.4 and 2.5 illustrate $\phi(r)$ at different times for the maximum resolution employed ($\Delta r = M/100$). Figure 2.4 corresponds to the time-harmonic initial data, and figure 2.5 to non-time-harmonic initial data. In both cases we sampled along two different periods at $t \approx 80M$; and then at $t \approx 160M$. The corresponding pairs, are then plotted together illustrating how after 22 periods apart the solutions are essentially the same. This is further illustrated in figure 2.6 where we show the difference between each of these pairs for three different resolutions.

Finally, figure 2.7 displays the absolute value of the Fourier transform in time of $\int \phi \, dr$, denoted $|F[\phi]|$. The scalar field is first integrated in space, then a discrete Fourier transform in t is calculated, where t ranges from 0 to $200M$ in the case of time-harmonic initial data, and from $t_0 = 60M$ to $200M$ in the non-time-harmonic case. In the plot we also indicate the frequencies ($f_n = \omega_n/2\pi$) obtained from the shooting integration when calculating the time-harmonic states. The time t_0 is chosen after the initial transient behavior, indicated by a time-harmonic behavior observed in ϕ. The initially non-time-harmonic scalar field relaxes to a superposition of the first three time-harmonic modes, the first one being the dominant one. We point out here that
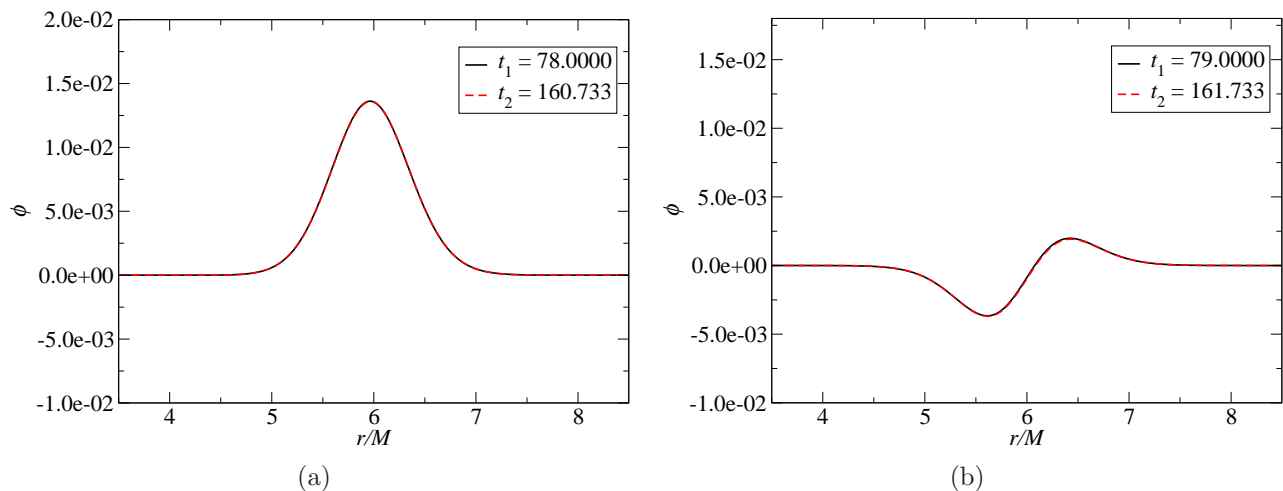
Figure 2.4: The scalar field at different times is compared to check if the evolution remains described by a time-harmonic dependence. Case with time-harmonic initial data. Initial mass of the scalar field $m_{\mathrm{sf}} = 0.01M$. Figure 2.4(a) shows the scalar field when it reaches a maximum, while figure 2.4(b) shows it at about a quarter of a period later. In both cases, the profile shown in continuous line is separated 22 periods from the one in dashed line.
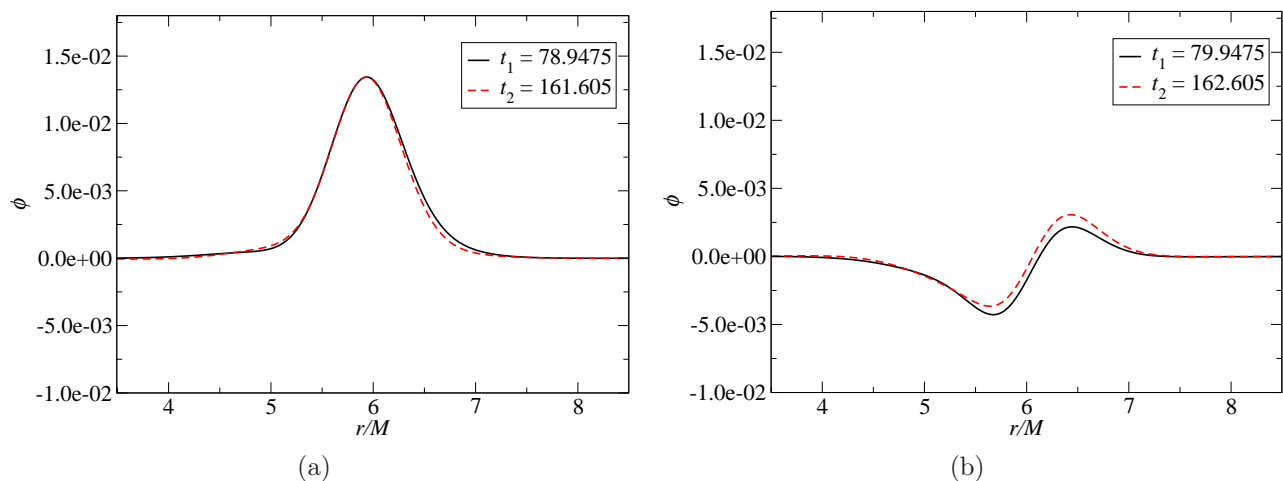
Figure 2.5: Here we show the same comparison of profiles as in figure 2.4, this time for the case with non-time-harmonic initial data. The separation between the profiles compared is also 22 periods. The initial mass of the scalar field is $m_{\mathrm{sf}} = 0.01M$.

for this configuration, the shooting method gives rise to three possible modes. It is thus not surprising that the evolution gives rise to a solution described by these modes. Deeper potentials give rise to more modes.

Figures 2.8 and 2.9 show the Misner-Sharp mass function (equation (2.54)) for both types of initial data. The continuous line shows the initial value (M_{MS} at $t = 0$). The discontinuous lines show M_{MS} at $t = 200M$ for three different resolutions. In both cases the asymptotic value of the mass stays constant, indicating no scalar field energy is radiated away. An inspection of the mass behavior at smaller radii for the solution obtained with time-harmonic initial data reveals that this converges to essentially the initial value, thus a negligible amount of mass falls into the black hole. For the non-time-harmonic case about 10% of the field's initial mass falls into the black hole.
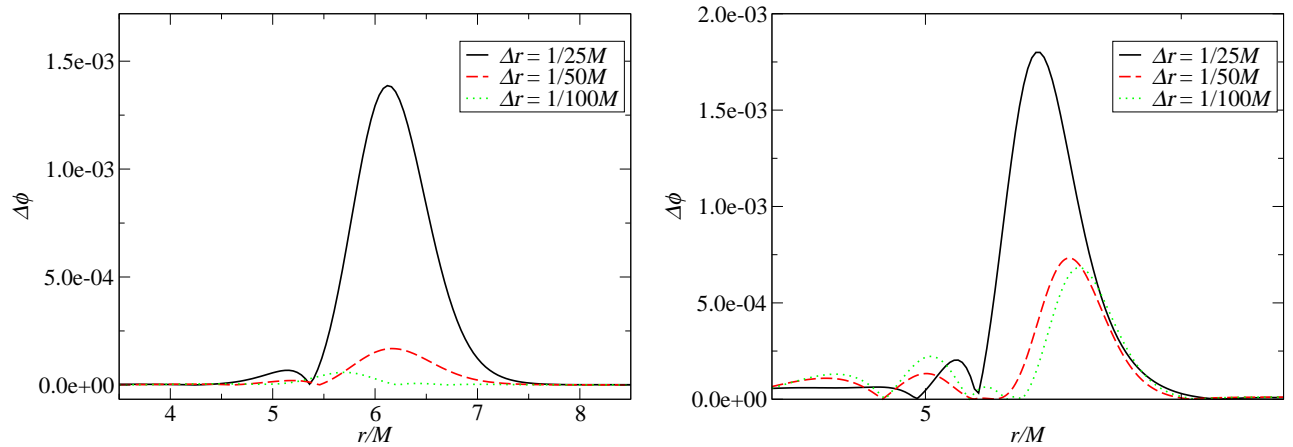
(a) $|\phi(t_1) - \phi(t_2)|$ for the case with time-harmonic initial data (see figure 2.4(a))

(b) $|\phi(t_1) - \phi(t_2)|$ for the case with non-time-harmonic initial data (see figure 2.5(a))

Figure 2.6: Absolute value of the difference between the scalar field at different times: $|\phi(t_1) - \phi(t_2)|$, where $t_2 - t_1 = 22$ periods. Figure 2.6(a) shows the difference between the profiles shown in figure 2.4(a), while figure 2.6(b) shows the difference between those in figure 2.5(a). In each case, we show these differences for three resolutions.
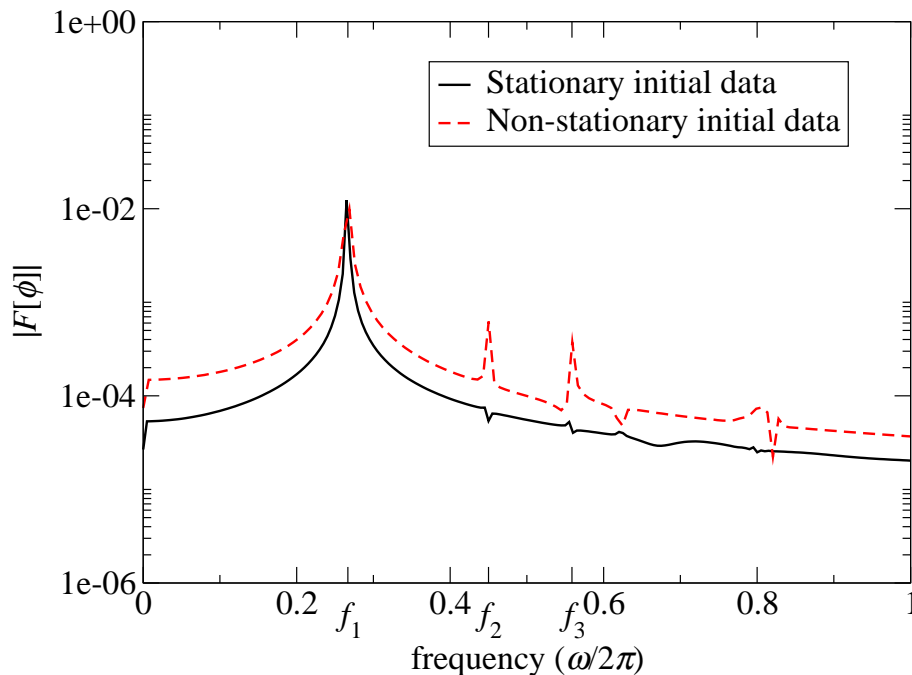
Figure 2.7: Absolute value of the discrete Fourier transform in time of $\int \phi\, dr$. The continuous line corresponds to the time-harmonic initial data, while the dashed line corresponds to the non-time-harmonic initial data. In the later case, the scalar field relaxes to a superposition of the first time-harmonic modes, whose frequencies are shown in the figure (labeled f_n).

The amount of mass that falls into the black hole is calculated by subtracting the Misner-Sharp mass at the horizon, minus the initial mass of the black hole. In the case of time-harmonic initial data this number is $(1 \pm 3) \times 10^{-4} M$, while for that of non-time-harmonic initial data it is $(10 \pm 3) \times 10^{-4} M$ (see table 2.1 and figure 2.14). These values are calculated using the highest

23

resolution ($\Delta r = 1/100M$), and the errors as the difference of these values with those of a lower resolution ($\Delta r = 1/50M$).
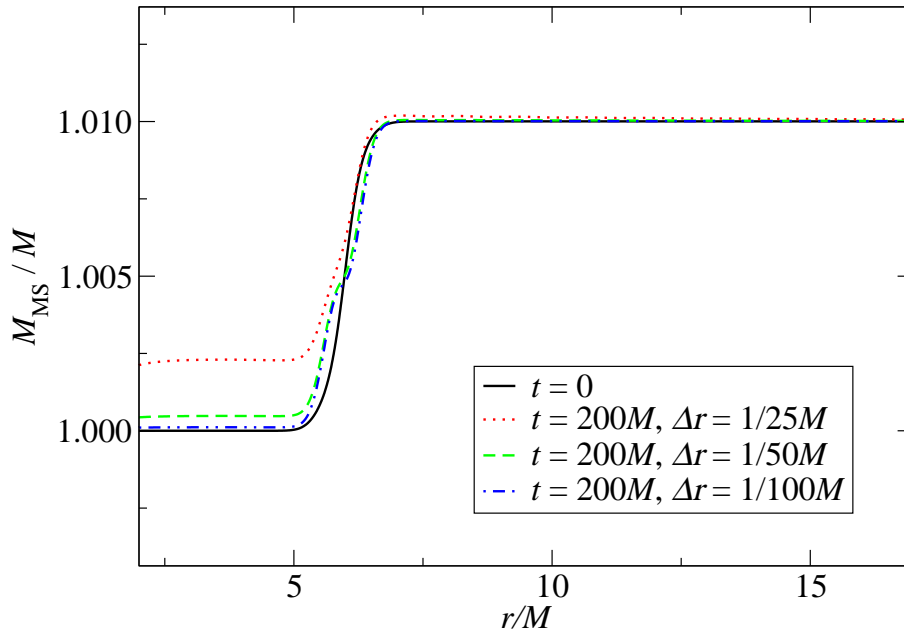
Figure 2.8: Mass function at $t = 0$; and at $t = 200M$ for three resolutions. Stationary initial data. Initial $m_{\rm sf} = 0.01M$. The continuous line shows the mass function at $t = 0$, while the discontinuous lines show, for different resolutions, the mass function at $t = 200M$. In this case the escape of mass into the black hole is negligible ($\Delta m_{\rm sf} = (1 \pm 3) \times 10^{-4}M$).

● **Non-Linear Case**

We turn now to the non-linear cases investigated. These correspond to initial mass configurations where the scalar field has a mass of at least 10% of that of the black hole. In this regime we solely adopt the "pulse" prescription defined in equation (2.50) for the scalar field since the time-harmonic data is obtained under an assumption which is no longer valid.

As we have done for the linear case, we also compare profiles at different times for simulations with higher initial $m_{\rm sf}$. Figures 2.10 and 2.11 correspond to initial masses of the scalar field of $m_{\rm sf} = 0.10M$ and $m_{\rm sf} = 0.50M$, respectively. The time it takes to reach a state described by a harmonic time dependence is longer than in the linear regime, especially for the higher initial $m_{\rm sf} = 0.50M$. For that reason, the first samplings (labeld t_1 in the figures) occur later than in the linear case, and the interval between the profiles compared, $t_2 - t_1$, is ten periods, as opposed to 22 in the linear cases.

The absolute value of the Fourier transform of $\int \phi \, dr$, $|F[\phi]|$, is shown in figure 2.12 for the two different initial masses of ϕ. Again, we compute the transformation after the initial transient behavior has passed and the scalar field has already reached a quiescent state. As a useful indicator, we also show the frequencies corresponding to time-harmonic states. Now, while the observed modes do not coincide exactly with those obtained at the linear approximation, they are close to them.

In figure 2.13 we show the Misner-Sharp mass at $t = 0$; and at $t = 200M$ for three different resolutions. Figures 2.13(a) and 2.13(b) correspond to initial masses of the scalar field of $m_{\rm sf} = $
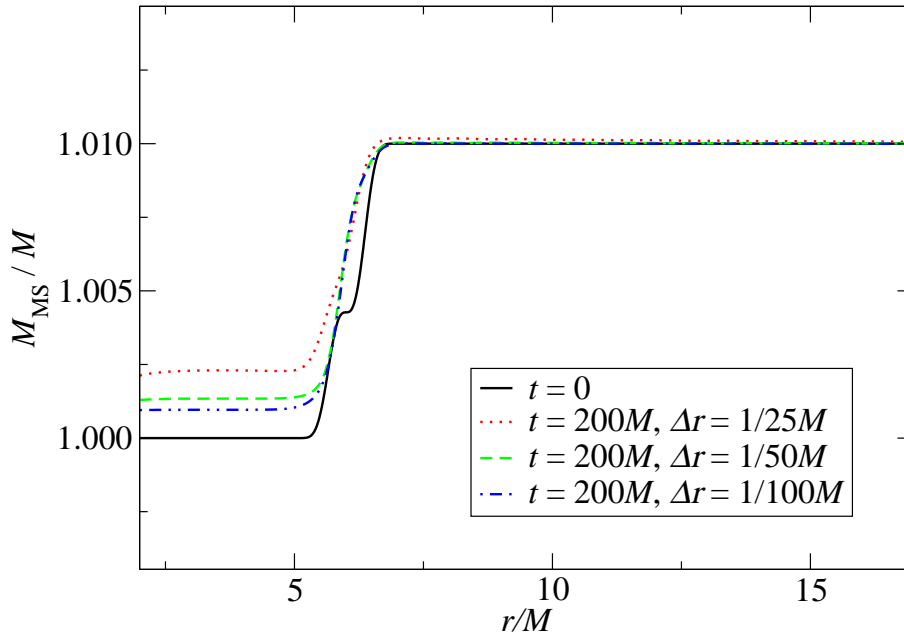
Figure 2.9: As in fig. 2.8, we show the mass function, this time for the non-time-harmonic case. The initial mass of the scalar field is $m_{\text{sf}} = 0.01M$. This time about 10% of it falls into the black hole.
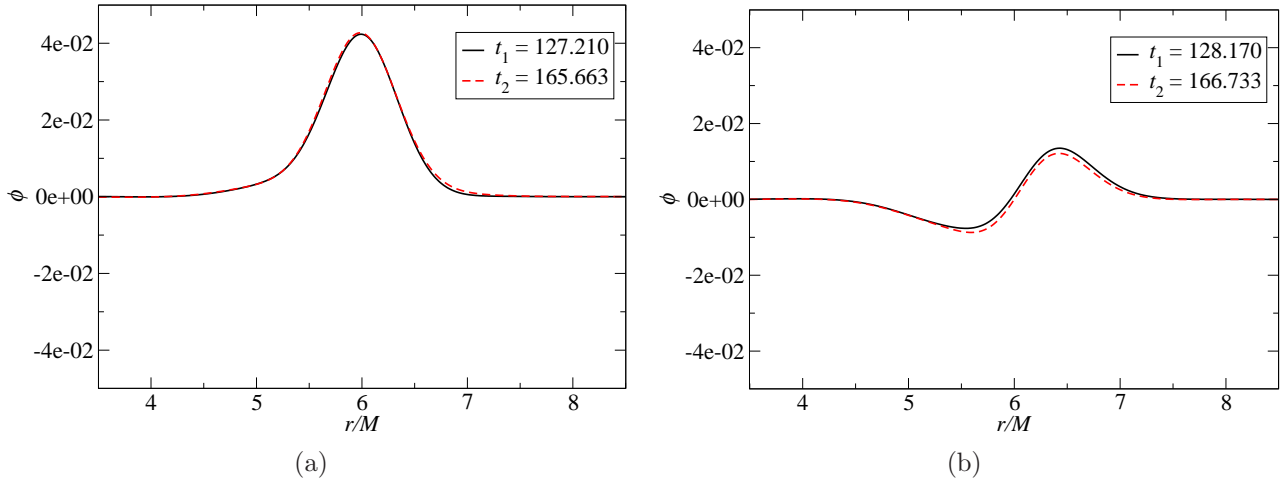
Figure 2.10: The scalar field at different times is compared to check if the solution obeys a harmonic time dependence. Case with non-time-harmonic initial data. Initial mass of the scalar field $m_{\text{sf}} = 0.10M$. Figure 2.10(a) shows the scalar field when it reaches a maximum, while figure 2.10(b) shows it at about a quarter of a period later. In both cases, the profile shown in continuous line is separated 10 periods from the one in dashed line.

$0.10M$ and $m_{\text{sf}} = 0.50M$, respectively. In all these cases about 10% of the scalar field's mass falls into the black hole, while nothing escapes outwards. Additionally, for the case with greater mass, the scalar field spreads slightly outwards before reaching a quiescent state. Although we only show figures corresponding to two different initial values of m_{sf}, we have simulated the system for other values of this parameter $m_{\text{sf}} = \kappa\, 10^{-1}M$ ($\kappa = 1...5$). In all these cases essentially no scalar field energy is radiated away, while a small portion falls into the black hole.
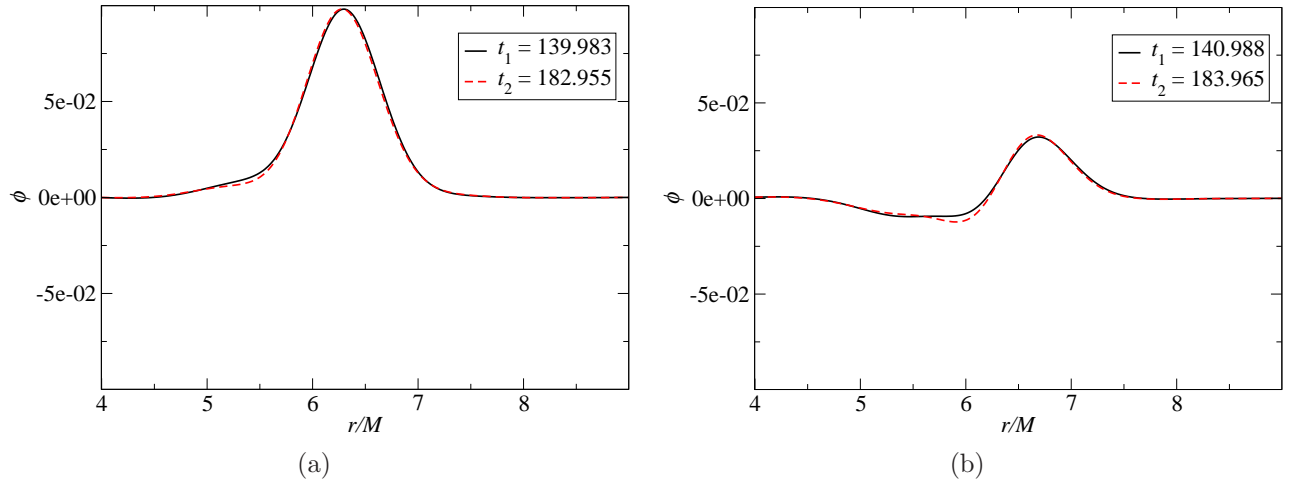
Figure 2.11: This figure shows the same comparisons as figure 2.10, but for an initial mass of the scalar field of $m_{\mathrm{sf}} = 0.50M$. The separation between the profiles compared is also 10 periods.

(a) Initial $m_{\mathrm{sf}} = 0.10M$

(b) Initial $m_{\mathrm{sf}} = 0.50M$
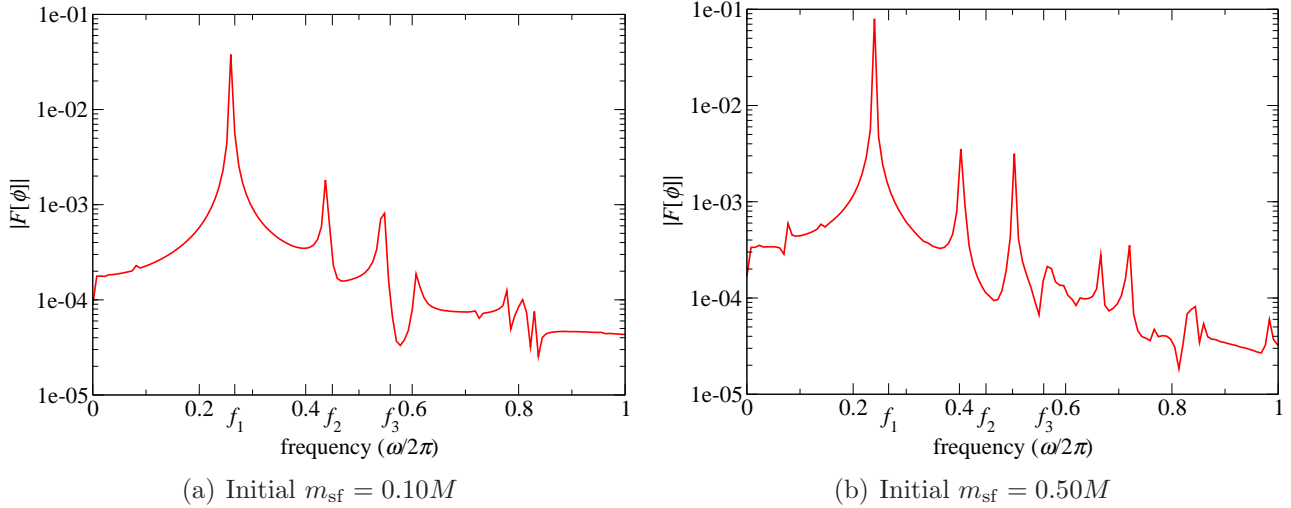
Figure 2.12: Absolute value of the discrete Fourier transform in t of the space integral $\int \phi(r,t)\,dr$. The marks labeled f_n denote the frequencies of the first modes obtained from the shooting. The three peaks, which indicate the dominant frequencies in the solution, lie at slightly lower frequencies than those of the time-harmonic states in the linear case. This behavior is consistent with the frequency shift due to the black hole growing in size. However, the growth alone does not fully account for the observed shift, though this is expected as non-trivial contribution due to non-linearities also play a role.

The measured values are shown in table 2.1 and figure 2.14.

Recall that, by virtue of Birkhoff's theorem [6], if after some transient time the scalar field is finally confined within a compact region, lets say $[r_a, r_b]$, the space-time should be that of Schwarzschild for $r > r_b$, with a Schwarzschild mass equal to the total mass inside the sphere $r = r_b$. This can be checked by evaluating the Kretschmann invariant. In figure 2.15 we show the quotient I/I_{Sch} (see the paragraph containing equation (2.56)) at $t \approx 140M$ for the case with initial $m_{\mathrm{sf}} = 0.5M$. This quotient converges to one for $r > r_b$, and also for $r < r_a$.

(a) Initial $m_{\text{sf}} = 0.10M$ (b) Initial $m_{\text{sf}} = 0.50M$
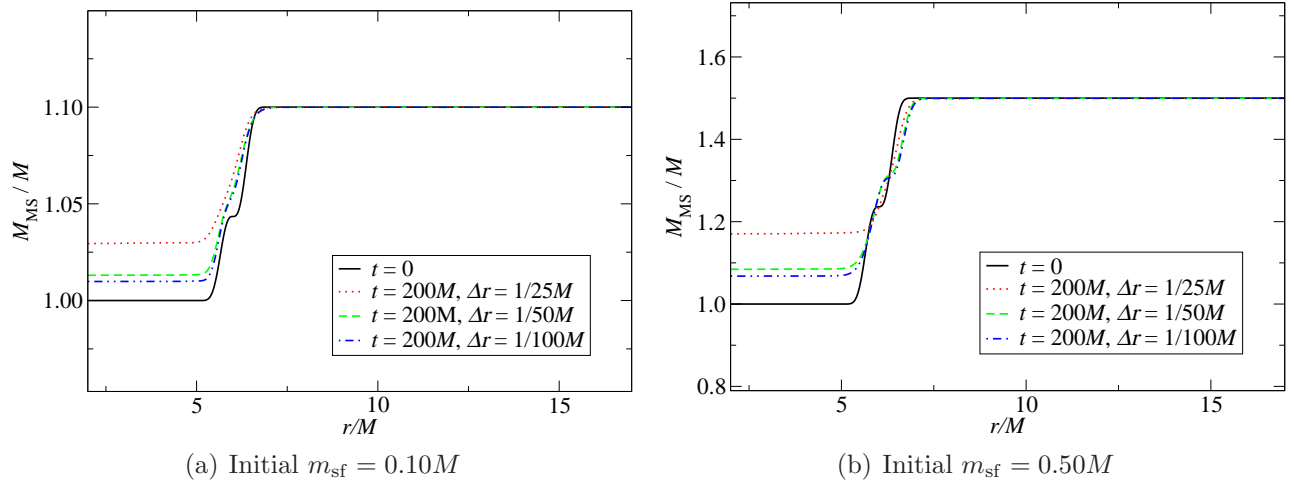
Figure 2.13: Mass function at $t = 0$; and at $t = 200M$ for three resolutions. The discontinuous lines show the mass function at t=200M for three resolutions. In each of these cases, about 10% of the initial mass of the scalar field falls into the black hole, while nothing escapes to infinity.

Table 2.1: Mass that falls into the black hole for different initial masses of the scalar field. Calculated as the Misner-Sharp mass at the horizon at $t = 200$ minus the initial mass of the black hole. See figure 2.14.

Initial m_{sf} $[M]$	$(M_{\text{MS}}(r_{\text{h}}) - M)$ $[10^{-2}M]$
0.01	0.10 ± 0.03
0.10	1.0 ± 0.3
0.20	2.9 ± 0.7
0.30	3 ± 1
0.40	5 ± 1
0.50	7 ± 2
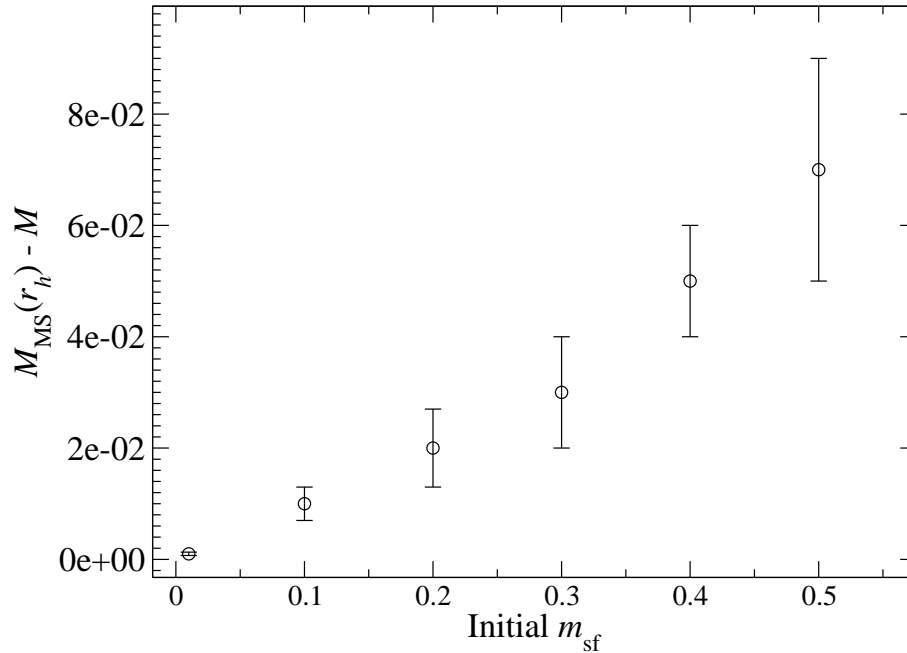
Figure 2.14: Mass that falls into the black hole for different initial masses of the scalar field. Calculated as the Misner-Sharp mass at the horizon at $t = 200$ minus the initial mass of the black hole. See table 2.1.
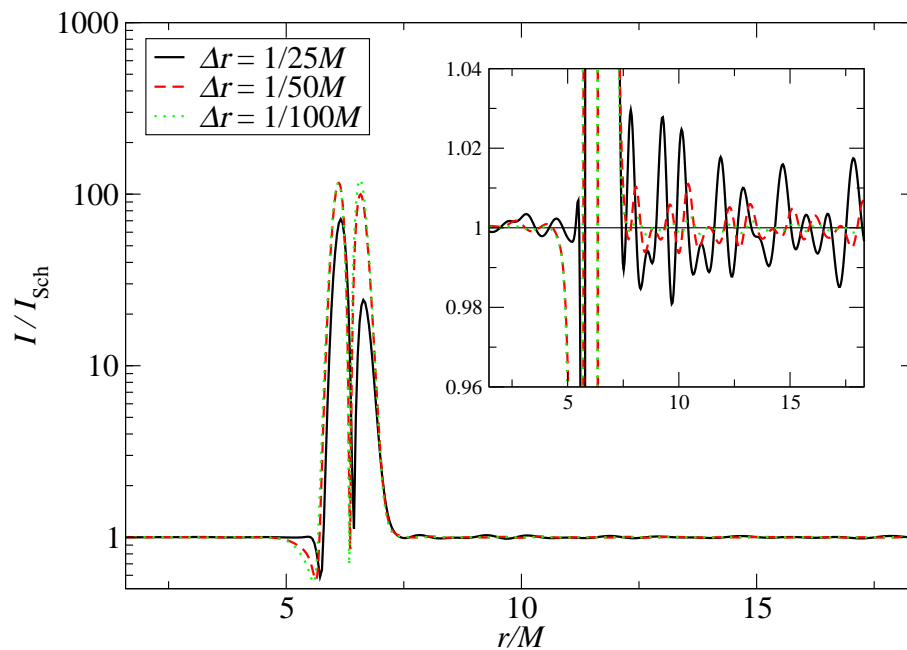
Figure 2.15: Kretschmann invariant quotient for three resolutions at $t_1 = 139.983M$. This quotient converges to 1 outside of the region where the scalar field is confined. A horizontal line at $I/I_{Sch} = 1$ have been drawn as a guide. Initial $m_{sf} = 0.50M$.

2.6 Conclusions

We have discussed difficulties encountered when attempting to confine a scalar field distribution within some region. The existence of a symmetry in the spacetime allows for doing so in a consistent manner. For the specific spherically symmetric case, we have given prescriptions for implementing a scalar field with a potential depending on the areal radius R.

We have illustrated the viability of this approach by confining a scalar field distribution around a black hole. For our particular choice of potential and initial scalar field, the scalar field becomes totally confined after some transient time, which depends on the initial mass. During the transient, part of the scalar field accretes into the black hole, while nothing escapes to infinity. By adjusting the depth of the potential, the amount of energy that falls in can be controlled.

The approach can be exploited, and extended, to mimic situations of interest. These can range from physical studies of particular systems, to serve as a testing model for infrastructure development aimed to simulate more complex systems.

2.7 Supplementary Material

2.7.1 Coordinate-Dependent Potential in Axial Symmetry

We now follow a procedure similar to that shown in section 2.2.1 to obtain a coordinate dependent potential, but for the case of axial symmetry.

Following [45], we write the (general) axi-symmetric line element in the form

$$ds^2 = -e^{2\nu}(dt)^2 + e^{2\psi}\left(d\varphi - q_1 dx^1 - q_2 dx^2 - \omega dt\right)^2 + e^{2\mu_1}(dx^1)^2 + e^{2\mu_2}(dx^2)^2, \qquad (2.57)$$

where all the functions appearing here are functions of $x^0 \equiv t$, x^1, and x^2, but independent of $x^3 \equiv \varphi$. We assume that the scalar field ϕ is independent of φ, and hence use $H^a{}_b$ as given in (2.16). Evaluating $\nabla_a H^a{}_b$ (and assuming that h and b are independent of φ) we find that the φ-component is of the form $(h - b)$ times an expression depending on the metric functions and their derivatives. We assume that the expression multiplying $(h - b)$ is not zero, because at this moment we want to consider the case of no other symmetry other than the axial symmetry. Then, setting this component to zero, we have the condition $b = h$, which, as we have seen earlier, implies that h is a constant. This means that the potential will be independent of the coordinates.

Consider now the special case of axial symmetry without rotation. We can write the line element in the form

$$ds^2 = g_{\varphi\varphi}d\varphi^2 + g_{ij}dx^i dx^j, \quad i, j \neq 3 \qquad (2.58)$$

Evaluating $\nabla_a H^a{}_b$, the φ-component this time results identically zero, and, setting the other components to zero, we have:

$$\frac{dg_{\varphi\varphi}}{dt}(h - b) + 2g_{\varphi\varphi}\frac{dh}{dt} = 0, \qquad (2.59)$$

$$\frac{dg_{\varphi\varphi}}{dx^1}(h - b) + 2g_{\varphi\varphi}\frac{dh}{dx^1} = 0, \qquad (2.60)$$

$$\frac{dg_{\varphi\varphi}}{dx^2}(h - b) + 2g_{\varphi\varphi}\frac{dh}{dx^2} = 0. \qquad (2.61)$$

At this point, one can follow the same procedures as in section 2.2.1 (compare these equations to (2.20) and (2.21)). For that reason, in this section we will just summarize the results.

Equations (2.59)-(2.61) are satisfied if, (i): h depends on the coordinates only through an arbitrary function of $g_{\varphi\varphi}$,

$$h(t, x^1, x^2) = f(g_{\varphi\varphi}(t, x^1, x^2)), \tag{2.62}$$

and (ii): b is given in terms of h by

$$b = h + 2g_{\varphi\varphi}\frac{\partial h}{\partial g_{\varphi\varphi}}. \tag{2.63}$$

Given these conditions, one can express $\nabla_a T^a{}_b$ with $\nabla_b\phi$ as a common factor, and, setting it to zero, obtain the equation of motion for the scalar field,

$$\nabla_a\nabla^a\phi + \frac{\partial f}{\partial \phi}\, h(g_{\varphi\varphi}) = 0, \tag{2.64}$$

where f and h are arbitrary functions of ϕ and $g_{\varphi\varphi}$, respectively. On can, in particular, choose these functions as follows,

$$f(\phi) = -\frac{1}{2}\phi^2, \tag{2.65}$$

$$h(g_{\varphi\varphi}) = m^2 + U(g_{\varphi\varphi}). \tag{2.66}$$

Then, the evolution equation becomes

$$\left(\nabla_a\nabla^a - m^2 - U(g_{\varphi\varphi})\right)\phi = 0, \tag{2.67}$$

where we can interpret U as a coordinate-dependent potential.

2.7.2   Evolution and Constraint Equations

We show here the explicit form of the Einstein and scalar field equations descirbed earlier. Denoting derivative with respect to t with a dot, and derivatives with respect to r with a prime, we can write the equations of motion (see section 2.3) as

$$\dot{g}_{rr} = \beta g'_{rr} + 2g_{rr}\beta' - 2\tilde{\alpha}g_{rr}^{1/2}g_T K_{rr} , \tag{2.68}$$

$$\dot{g}_T = \beta g'_T - 2\tilde{\alpha}g_{rr}^{1/2}g_T K_T + \frac{2\beta g_T}{r} , \tag{2.69}$$

$$\dot{K}_{rr} = \beta K'_{rr} - \tilde{\alpha}g_{rr}^{-1/2}g_T f'_{rrr} - \tilde{\alpha}''g_{rr}^{1/2}g_T - 6g_T^{-1}g_{rr}^{1/2}\tilde{\alpha}f_{rT}^2 + 4g_T r^{-1}g_{rr}^{1/2}\tilde{\alpha}' \tag{2.70}$$

$$-6g_T r^{-2}g_{rr}^{1/2}\tilde{\alpha} + 2K_{rr}\beta' - g_T g_{rr}^{-1/2}\tilde{\alpha}K_{rr}^2 + 2g_{rr}^{1/2}\tilde{\alpha}K_{rr}K_T - 8g_{rr}^{-1/2}\tilde{\alpha}f_{rT}f_{rrr}$$

$$+2g_T g_{rr}^{-3/2}\tilde{\alpha}f_{rrr}^2 + 2g_T r^{-1}g_{rr}^{-1/2}\tilde{\alpha}f_{rrr} - g_T g_{rr}^{-1/2}\tilde{\alpha}f_{rrr} + g_T g_{rr}^{1/2}\tilde{\alpha}\, 4\pi(Tg_{rr} - 2S_{rr}) ,$$

$$\dot{K}_T = \beta K'_T - \tilde{\alpha}g_T g_{rr}^{-1/2}f'_{rT} + 2\beta r^{-1}K_T + g_T r^{-2}g_{rr}^{1/2}\tilde{\alpha} + \tilde{\alpha}g_T K_T K_{rr}g_{rr}^{-1/2} \tag{2.71}$$

$$-g_T f_{rT}\tilde{\alpha}' g_{rr}^{-1/2} - 2\tilde{\alpha}f_{rT}^2 g_{rr}^{-1/2} + \tilde{\alpha}g_{rr}^{1/2}g_T\, 4\pi(Tg_T - 2S_T)\ ,$$

$$\dot{f}_{rrr} = \beta f'_{rrr} - \tilde{\alpha}g_{rr}^{1/2}g_T K'_{rr} - 4g_{rr}^{3/2}\tilde{\alpha}'K_T + 12g_T^{-1}g_{rr}^{3/2}\tilde{\alpha}K_T f_{rT} - 4g_{rr}^{1/2}\tilde{\alpha}K_T f_{rrr} \tag{2.72}$$

$$-g_T g_{rr}^{-1/2}\tilde{\alpha}K_{rr}f_{rrr} - 10g_{rr}^{1/2}\tilde{\alpha}K_{rr}f_{rT} + 3f_{rrr}\beta' + g_{rr}\beta'' - \tilde{\alpha}'g_{rr}^{1/2}g_T K_{rr}$$

$$+2r^{-1}g_T g_{rr}^{1/2}\tilde{\alpha}K_{rr} + 8r^{-1}g_{rr}^{3/2}\tilde{\alpha}K_T + 4\tilde{\alpha}g_{rr}^{3/2}g_T\, 4\pi J_r\ ,$$

$$\dot{f}_{rT} = \beta f'_{rT} - \tilde{\alpha}g_{rr}^{1/2}g_T K'_T + \beta' f_{rT} - \tilde{\alpha}'g_{rr}^{1/2}g_T K_T + 2g^{1/2}\tilde{\alpha}K_T f_{rT} \tag{2.73}$$

$$-\tilde{\alpha}g_{rr}^{-1/2}K_T f_{rrr}g_T + 2r^{-1}\beta f_{rT}\ ,$$

$$\dot{\Phi} = \beta\Phi' - \tilde{\alpha}g_{rr}^{1/2}g_T\Pi' - g_{rr}^{-1/2}\tilde{\alpha}g_T\Pi f_{rrr} + 2\tilde{\alpha}g_{rr}^{1/2}\Pi f_{rT} + 2r^{-1}\tilde{\alpha}g_{rr}^{1/2}g_T\Pi \tag{2.74}$$

$$-\tilde{\alpha}'g_{rr}^{1/2}g_T\Pi + \Phi\beta'\ ,$$

$$\dot{\Pi} = \beta\Pi' - g_{rr}^{-1/2}\tilde{\alpha}g_T\Phi' + g_{rr}^{-1/2}\tilde{\alpha}g_T\Pi K_{rr} + 2\tilde{\alpha}g_{rr}^{1/2}\Pi K_T - 4g_{rr}^{-1/2}\tilde{\alpha}\Phi f_{rT} \tag{2.75}$$

$$+2r^{-1}g_{rr}^{-1/2}\tilde{\alpha}g_T\Phi - g_{rr}^{-1/2}g_T\Phi\tilde{\alpha}' + g_{rr}^{1/2}g_T\tilde{\alpha}V\phi\ ,$$

$$\dot{\phi} = \beta\phi' - g_T g_{rr}^{1/2}\tilde{\alpha}\Pi\ , \tag{2.76}$$

where $\tilde{\alpha} = \alpha r^2\sin\theta = N/\sqrt{g_{rr}}g_T$; and the "source terms", ρ, T, J_r, S_{rr} and S_T, are defined as

$$4\pi\rho = \frac{V\phi^2}{2} + \frac{\Phi^2}{2g_{rr}} + \frac{\Pi^2}{2}\ , \tag{2.77}$$

$$4\pi T = -2V\phi^2 - \frac{\Phi^2}{g_{rr}} + \Pi^2 + $$
$$-\phi^2 r^2 g_T\frac{\partial V}{\partial g_\Omega}\ , \tag{2.78}$$

$$4\pi J_r = \Phi\Pi\ , \tag{2.79}$$

$$4\pi(Tg_{rr} - 2S_{rr}) = -V\phi^2 g_{rr} - 2\Phi^2 + $$
$$-\phi^2 g_{rr}r^2 g_T\frac{\partial V}{\partial g_\Omega}\ , \tag{2.80}$$

$$4\pi(Tg_T - 2S_T) = -g_T V\phi^2\ , \tag{2.81}$$

where $g_\Omega = r^2 g_T$ (see section 2.2.1).

Finally, the constraint equations are

$$C = \frac{f'_{rT}}{g_{rr}g_T} - \frac{1}{2r^2 g_T} + \frac{f_{rT}\left(\frac{2}{r} + \frac{7f_{rT}}{2g_T} - \frac{f_{rrr}}{g_{rr}}\right)}{g_{rr}g_T} + $$

$$-\frac{K_T\left(\frac{K_{rr}}{g_{rr}} + \frac{K_T}{2g_T}\right)}{g_T} + 4\pi\rho \;, \tag{2.82}$$

$$C_r \;=\; \frac{K_T'}{g_T} + \frac{2K_T}{rg_T} - \frac{f_{rT}\left(\frac{K_{rr}}{g_{rr}} + \frac{K_T}{g_T}\right)}{g_T} +$$
$$+4\pi J_r \;, \tag{2.83}$$

$$C_{rrr} \;=\; g_{rr}' + \frac{8g_{rr}f_{rT}}{g_T} - 2f_{rrr} \;, \tag{2.84}$$

$$C_{rT} \;=\; g_T' + \frac{2g_T}{r} - 2f_{rT} \;, \tag{2.85}$$

$$C_m \;=\; \Phi - \phi' \;, \tag{2.86}$$

2.7.3   Characteristic Structure

The characteristic modes and eigenvalues obtained at a surface $r = const$ (see section 2.4.2) are given by

$$
\begin{aligned}
u_1 &= g_{rr}, & \lambda_1 &= \beta, \\
u_2 &= g_T, & \lambda_2 &= \beta, \\
u_3 &= K_{rr} - f_{rrr}/g_{rr}, & \lambda_3 &= \beta + \tilde{\alpha}g_T, \\
u_4 &= K_T - f_{rT}/g_{rr}, & \lambda_4 &= \beta + \tilde{\alpha}g_T, \\
u_5 &= K_{rr} + f_{rrr}/g_{rr}, & \lambda_5 &= \beta - \tilde{\alpha}g_T, \\
u_6 &= K_T + f_{rT}/g_{rr}, & \lambda_6 &= \beta - \tilde{\alpha}g_T, \\
u_7 &= \Pi + \Phi/g_{rr}, & \lambda_7 &= \beta - \tilde{\alpha}g_T, \\
u_8 &= \Pi - \Phi/g_{rr}, & \lambda_8 &= \beta + \tilde{\alpha}g_T, \\
u_9 &= \phi, & \lambda_9 &= \beta.
\end{aligned} \tag{2.87}
$$

2.7.4   Code Tests

The standard code tests have been performed, showing that all the constraints and residuals converge to zero with order two, as expected. In figure 2.16 we show the Hamiltonian constraint, in the case of the strongest scalar field studied, that with initial $m_{\mathrm{sf}} = 0.5M$.

The evaluation of the constraints is a particularly important test in this work, to ensure that the implementation of a coordinate dependent potential is not breaking the covariance of the theory.
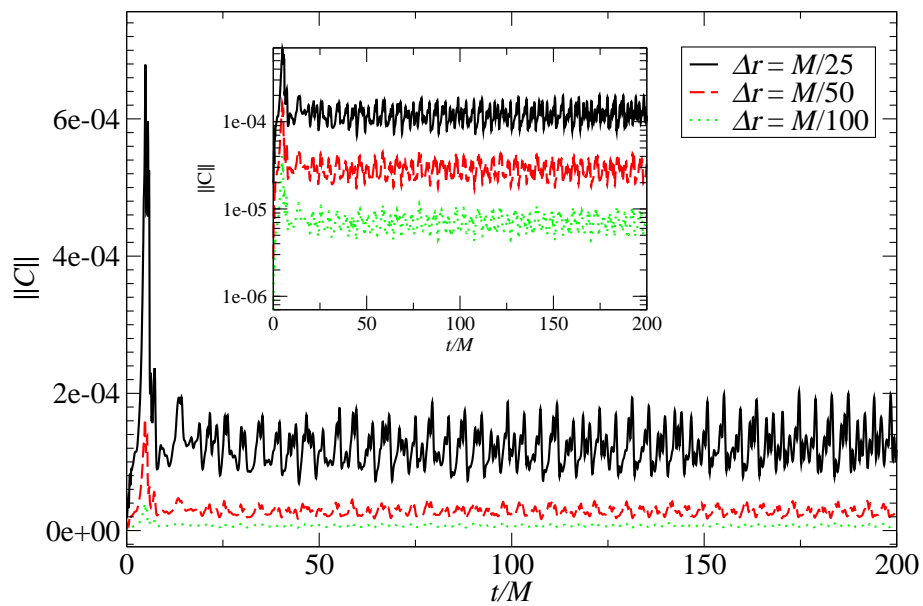
Figure 2.16: L_2 norm of the Hamiltonian constraint (equation (2.82)) for three different resolutions. The overlay graph shows the same constraint, but in logarithmic scale. The measured convergence results of order two as expected.

Chapter 3
Method to Estimate Time-Frequency Characteristics of Compact Binary Mergers.

In this chapter we present a method to estimate the gravitational wave frequency at the end of the inspiral phase of a compact binary. These frequency estimations can be used to study the possibility of a neutron star's tidal disruption occurring before plunging into the companion black hole. This estimations also provide a way of improving gravitational wave data analysis when using match filtering techniques.

The work shown here contains part of a published work [46] done in collaboration with researchers in gravitational wave data analysis. In particular, those applications pertaining mostly to data analysis are elaborated with more detail in that paper. Here I overview (section 3.4) some of those results, that suggest that the frequencies calculated in this chapter serve well as cut off frequencies for post Newtonian templates, and refer the reader to the mentioned paper for more details.

3.1   Introduction

As explained in chapter 1, the coalescence of compact objects shows different phases during the evolution that one may identify on the waveforms. For example, a binary black hole coalescence is characterized by three distinct phases: inspiral, merger and ring-down. A black hole-neutron star binary generally provides more features, since the evolution in this case may include a tidal disruption phase.

In some situations, it is desirable to have an estimate of when one of these phases ends and the next begins. One motivation would be, for example, to know when to apply a given approximation that may describe accurately one of the phases but not the others. In this chapter, we obtain an estimation of the end frequency of the inspiral phase, and describe two applications, particularly relevant in the detection of gravitational waves with LIGO.

Of particular interest are systems with a total mass ranging from about a few to a hundred solar masses, giving a gravitational wave frequency within the range detectable by kilometer-size laser interferometric detectors, such as LIGO.

The first application shows how interpreting a particular frequency (section 3.2) as that marking the end of the inspiral phase has implications on the ability to probe tidal disruption of neutron stars through gravitational waves. During the inspiral phase of a binary black hole-neutron star, the neutron star may be tidally disrupted. In that case, the gravitational waves emitted can provide information about the neutron star's equation of state. For example, the model described in [47] makes use of the tidal disruption frequency, that could be measured with LIGO (together with the individual masses determined form the inspiral waveforms) to calculate the mean radius of the NS. These data suffice, in the simplified model of [47], to obtain the NS's equation of state.

The analysis described in the previous paragraph applies only if the neutron star is actually disrupted before plunging into the black hole, which would occur quickly after reaching the innermost stable circular orbit (ISCO). Hence, to determine the detectability of tidal disruption through that kind of analysis, a good estimation of the ISCO frequency is necessary.

A similar analysis could also be done in the case of a binary neutron star, whose gravitational waves may also carry information about the equation of state. However, the frequencies in that case are too high to be detectable by LIGO (see [47] and references therein).

In section 3.3 we re-calculate frequency upper limits for observability of tidal disruption from previous work [47], but using the ISCO frequencies obtained in section 3.2 in addition to the simpler model used in that work for comparison. We also compare with results from numerical relativity.

The second application relates to the use of matched filtering techniques in gravitational wave data analysis. These techniques allow faint signals to be detected reliably, since maximal signal-to-noise ratio is achieved when using banks of template waveforms in searches for compact binary coalescence [48, 49, 50, 51, 52].

Numerical relativity can provide knowledge of the full waveforms emitted during inspiral, merger and ring-down [53, 54, 55], that could be used as templates. However, numerical simulations to date do not yet cover a large enough parameter space as would be required for constructing template banks [56, 55]. Post Newtonian (PN) calculations show good agreement with numerical relativity during the inspiral phase, and can be used to construct template banks to search for this phase separately, at least until fully relativistic simulations can cover a larger parameter space. It is then important to know what portion (i.e.: up to what frequency) of the post Newtonian waveform could be used. As is shown in section 3.4, the cut off frequency obtained in section 3.2 provides a higher signal to noise ratio than others used currently in matching filtering techniques.

3.2   Formalism

Except in the case of extreme mass ratio binaries, there is not a well defined way of determining when the inspiral phase ends and the merger begins for much of the parameter space. In the extreme mass ratio case, the system can be viewed as a test particle orbiting a larger object with well defined space-time, such as Schwarzschild or Kerr space-time. In the test particle limit the end of the inspiral phase is generally taken to be the ISCO. This particle-limit estimation, or a similar one, is usually used even in situations with arbitrary mass ratios.

For instance, some LIGO searches for non-spinning systems have taken the conservative approach to use the ISCO defined for a test particle orbiting a Schwarzschild black hole whose mass is the total mass of the binary system to mark the end of inspiral for all non-spinning binary systems regardless of mass ratio [57]. This is conservative because it seems to under-predict the ISCO frequency estimates for nearly equal mass binaries (see sections 3.3 and 3.4).

The expression for the ISCO frequency derived in this section takes into account the orbital angular momentum, and includes an explicit dependence on the mass ratio and individual spins. The calculation is an extension of that used in [58] to obtain the final spin of the merged binary, which contains an implicit reference to the ISCO of a test particle orbiting the Kerr black hole that results from the merger. We begin by reviewing the formalism presented in that work, which shows good agreement with fully relativistic simulations. In the rest of this chapter we will use the acronym BKL (from the authors of [58]) to refer to this formalism and the frequencies obtained here basing on that method.

The ISCO solution for a test particle orbiting a Kerr black hole on the equatorial plane is [59]

$$Z_1 \equiv 1 + \left(1 - \frac{a_{\mathrm{f}}^2}{M^2}\right)^{1/3}\left[(1 + \frac{a_{\mathrm{f}}}{M})^{1/3} + (1 - \frac{a_{\mathrm{f}}}{M})^{1/3}\right]$$

$$Z_2 \equiv \left(3\frac{a_{\mathrm{f}}^2}{M^2} + Z_1^2\right)^{1/2}$$

$$r_{\mathrm{ISCO}} = M\{3 + Z_2 \mp [(3 - Z_1)(3 + Z_1 + 2Z_2)]^{1/2}\} \quad, \tag{3.1}$$

where M is the total mass of the black hole and a_{f} is the angular momentum. In [58], assuming the amount of mass and angular momentum radiated beyond the ISCO is small, the following implicit formula for the final angular momentum of a black hole a_{f} with component spins aligned with the orbit is calculated,

$$\frac{a_{\mathrm{f}}}{M} = \frac{L_{\mathrm{orb}}}{M^2}\left(q, \frac{r}{M} = \frac{r_{\mathrm{ISCO}}}{M}, \frac{a_{\mathrm{f}}}{M}\right) + \frac{q^2\chi_1 + \chi_2}{(1 + q)^2} \quad, \tag{3.2}$$

where $\chi_i = a_i/m_i$, $q = m_1/m_2 \in [0, 1]$ and $M = m_1 + m_2$ is the total mass. The implicitly found a_{f} agrees well with numerical simulations [58] and the analysis can be modified to include arbitrary spin angles. L_{orb} is the orbital angular momentum contribution calculated from the orbital angular momentum of a particle at the ISCO of a Kerr black hole with spin parameter a_{f}, which has the following expression [59],

$$\frac{L_{\mathrm{orb}}}{M^2}\left(q, \frac{r}{M}, \frac{a_{\mathrm{f}}}{M}\right) = \frac{q}{(1 + q)^2}\frac{\pm(r^2 \mp 2a_{\mathrm{f}}M^{1/2}r^{1/2} + a_{\mathrm{f}}^2)}{M^{1/2}r^{3/4}(r^{3/2} - 3Mr^{1/2} \pm 2a_{\mathrm{f}}M^{1/2})^{1/2}} \quad, \tag{3.3}$$

where the upper/lower signs correspond to prograde/retrograde orbits. In order to agree with numerical simulations this function has to be evaluated at $r = r_{\mathrm{ISCO}}$ given by equation (3.1).

In order to get the gravitational wave frequency at ISCO we use the coordinate angular velocity of a circular orbit [59],

$$\Omega = \pm\frac{M^{1/2}}{r^{3/2} \pm a_{\mathrm{f}}M^{1/2}} \quad, \tag{3.4}$$

with a_{f} given by the implicit equation (3.2), and r by equations (3.1). The gravitational-wave frequency at a given radius is then

$$f = \Omega/\pi, \tag{3.5}$$

and so we define $f_{\mathrm{ISCO\,[BKL]}}$ as the frequency obtained by solving the system of equations (3.1-3.4) at the Kerr ISCO radius.

The solution space for $f_{\mathrm{ISCO\,[BKL]}}$ can be written as a function of the final unknown spin a_{f}. For convenience, we prefer to extend it as a surface parameterized by $(a_{\mathrm{f}}, q, \chi)$, where $\chi_1 = \chi_2 \equiv \chi$, as it is shown in figure 3.1. Proceeding in this way, the mass ratio dependence of the lines corresponding to different individual spins can be seen explicitly.

For the case without spin one can use, for simplicity, an approximate expression for the ISCO frequency:

$$f_{\mathrm{ISCO\,[BKL]}}(M, q) \approx \left(0.8q^3 - 2.6q^2 + 2.8q + 1\right) \times \frac{1}{\pi 6^{3/2}M} \quad, \tag{3.6}$$

which is compared to the numerical solution in figure 3.2. Notice that, for $q = 0$, equation 3.6 reduces to the exact frequency corresponding to a Schwarzschild test particle ISCO:

$$f_{\mathrm{ISCO\,[SCH]}} = \frac{1}{\pi 6^{3/2}M}. \tag{3.7}$$

36
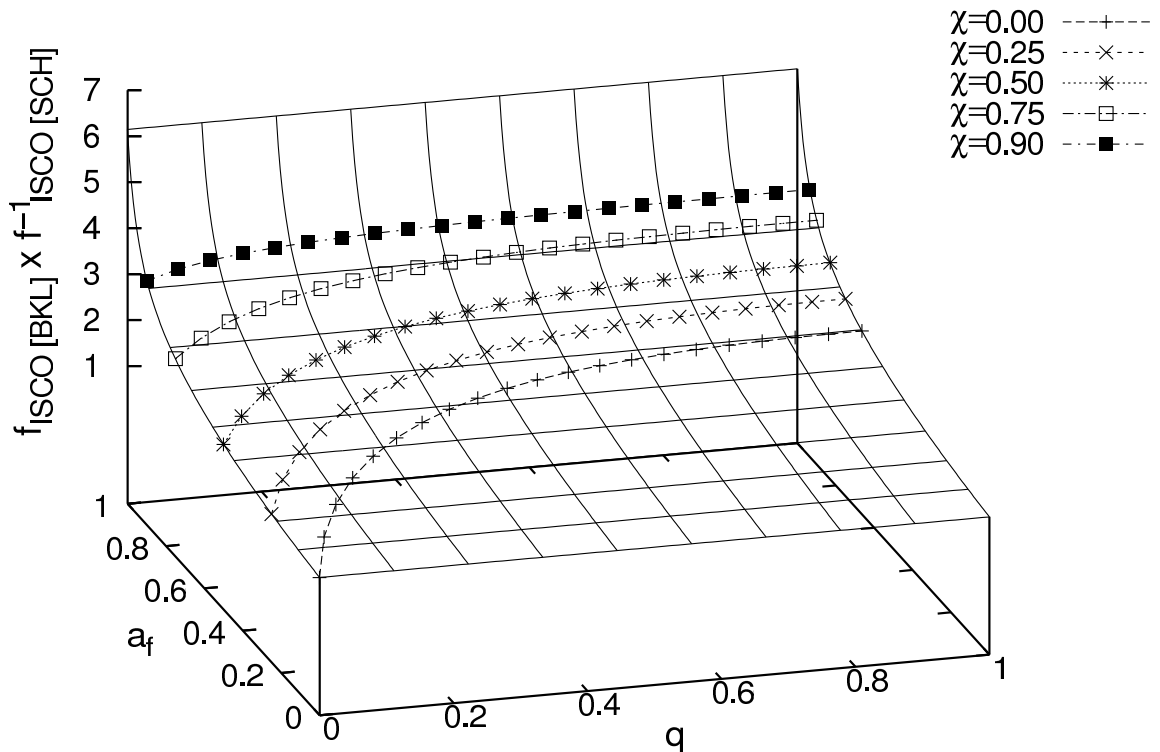
Figure 3.1: The surface of solutions of the frequencies at the ISCO as a function of the mass ratio q and the final spin a_f for components with spins that are aligned with the orbital angular momentum. Also shown, are curves corresponding to the solution of the equal spin case $\chi_1 = \chi_2 = \chi$.

3.3 Probing the Tidal Disruption of Neutron Stars

If the BKL ISCO truly marks (in the absence of tidal disruption) the transition from an inspiral, radiation-dominated evolution to a dynamical one, then it does have some consequence for the ability to probe the tidal disruption of neutron stars through gravitational waves. Estimation of gravitational-wave frequencies for tidal disruption of NS-BH binaries may be useful for determining various properties of the neutron star, such as its mean radius [47, 60]. Knowing the radius of the neutron star would in turn provide information about its equation of state [61, 62]. However, as pointed out in [47], it would be difficult to extract information about the disruption unless it occurs before the binary reaches the ISCO. If the disruption occurs afterwards, its signature in the produced gravitational waves might be too weak for extracting accurate information. Thus, the cases where a clear signal is expected are those for which the tidal-disruption frequency is less than the frequency at the plunge ($f_\mathrm{td} < f_\mathrm{plunge} \approx f_\mathrm{ISCO}$).

A more accurate calculation of f_plunge would imply a better estimate of the range of NS-BH binaries for which the disruption is more plausible to be measured. In this section we show how that range changes when the formalism of section 3.2 is applied, as compared to that in [47].

That work describes a relatively simple model to study the tidal disruption of neutron stars. The neutron stars are modeled as irrotational ellipsoids orbiting in Kerr geodesics (based on [63]), parameterized by their mass and mean radius at a given distance from the black hole. The inspiral is modeled as a sequence of progressively smaller circular orbits, until the star either reaches a critical density (or radius) at which point it begins to tidally disrupt, or it reaches
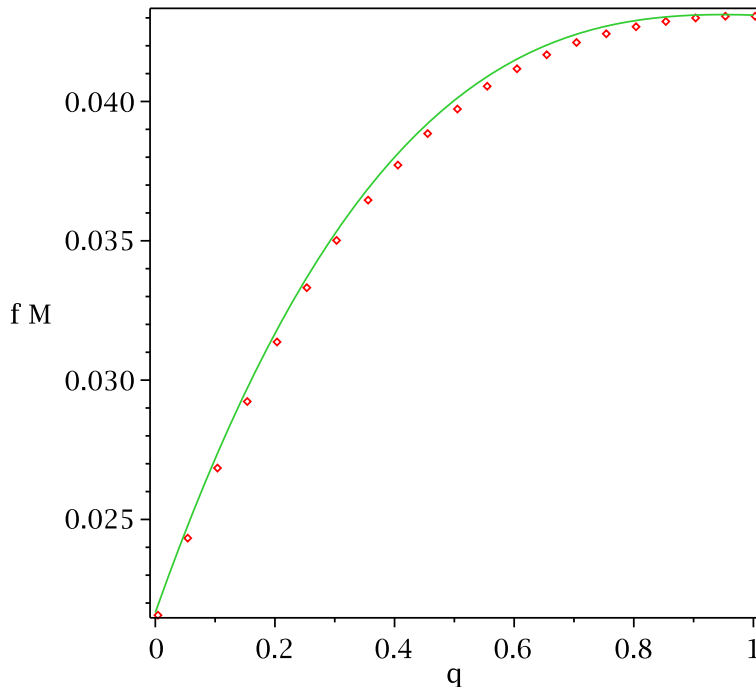
Figure 3.2: ISCO frequency vs mass ratio in the case of $\chi = 0$. Comparison of the solution of equations (3.1-3.4) obtained numerically (circles), to the approximate expression given in equation 3.6 (continuous line).

the ISCO and quickly plunges into the black hole, whichever occurs first. This model provides the NS's mean radius R as a function of the orbital distance r_{td} at which tidal disruption begins. Having in mind LIGO detections, it is more significant to speak about gravitational wave frequencies instead of orbital distances. To that end, one can re-express $R(r_{td})$ as $R(f_{td})$ using equations (3.4-3.5), where f_{td} is the gravity wave frequency at which the disruption begins. The observability of the disruption then depends on f_{td} being smaller than the plunge (or ISCO) frequency.

To compare with [47] we first plot R vs f_{td} (figure 3.3) for the same parameters as in that work: $m_{NS} = 1.4 M_\odot$; $m_{BH} = 2.5, 10, 20, 40$ and $80 M_\odot$. using the following approximation, given also there,

$$\frac{R}{m_{NS}^{1/3} m_{BH}^{2/3}} \approx \begin{cases} 0.145(f_{td}m_{BH})^{-0.71}, & f_{td}m_{BH} < 0.045 \\ 0.069(f_{td}m_{BH})^{-0.95}, & f_{td}m_{BH} > 0.045 \end{cases}. \tag{3.8}$$

These curves are valid only for frequencies lower than that at which, in the absence of disruption, the plunge would occur. The plunge frequencies, estimated as the ISCO frequencies, are represented with circles in figure 3.3. White circles correspond to the ISCO frequencies estimated using the BKL approach, while black circles correspond to those estimated in [47]. For each curve (i.e., for each black hole mass), we show more than one black and one white circle. This is because the ISCO frequency also depends on the black hole spin, so we show ISCO frequencies corresponding to different values of χ_{BH} in each case. We emphasize that, for each case, only the part of the curve that is to the left of the corresponding circle is valid. This means that the more to the right the circles are, the more the chances of detecting tidal disruption.

The ISCO frequencies obtained in [47] correspond to that of a test particle orbiting a (spinning) black hole of mass m_{BH}, equivalent to setting, in our approach, $m_{NS} = 0$, and hence $q = 0$,

$\chi_{\mathrm{NS}} = 0$ and $M = m_{\mathrm{BH}}$. In figure 3.3 we reproduce those results (compare to figure 2 of [47]), together with the values obtained using the formalism presented here. We also assume in this case that the neutron star is non-spinning, but with $q = m_{\mathrm{NS}}/m_{\mathrm{BH}} \neq 0$.
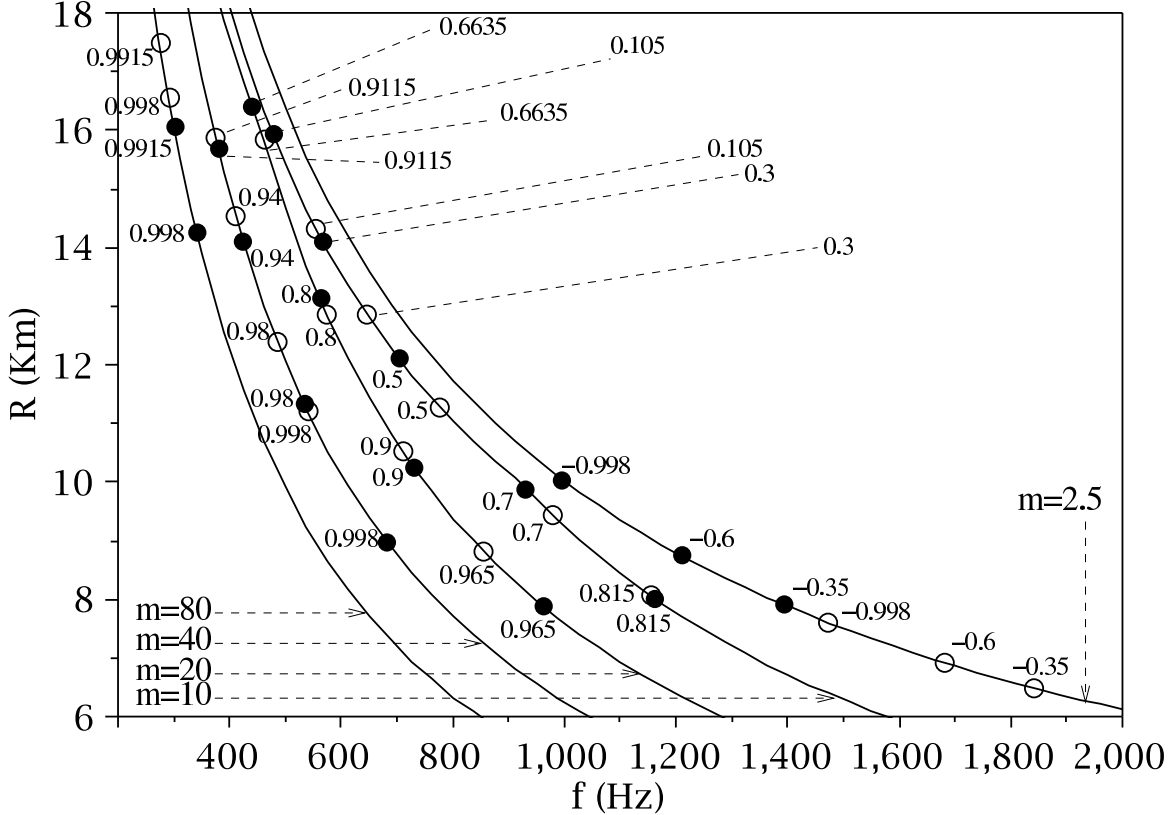
Figure 3.3: Radius of the neutron star vs. the disruption frequency. The circles indicate the points at which the plunge would occur; the filled circles correspond to f_{plunge} as calculated in [47], included here for comparison purposes. The value of χ_{BH} is indicated next to the corresponding circle where possible, otherwise a dashed line was used to connect the value to the circle. Each curve is labeled with the value of the BH mass: $m_{\mathrm{BH}} = 2.5 - 80 M_\odot$ (indicated, for clarity, as just m in the figure).

It is worth noticing that the plunge frequencies calculated in [47] for the case with $m_{BH} = 2.5 M_\odot$ (black circles in the right-hand-side curve of figure 3.3), where obtained assuming retrograde orbits. This is valid in the approach of [47], in which the plunge frequency is estimated as that of a test particle on a Kerr background (equivalent to setting $m_{\mathrm{NS}} = 0$, and hence $q = 0$, in our approach). That approach always admits both prograde and retrograde orbits. However, in our approach, for that particular case (in which the mass ratio is $q = 1.4/2.5 = 0.56$) the test particle orbiting the merger product ISCO does so in a prograde fashion due to the orbital angular momentum always dominating (see equation 3.2). Thus, the final spin is aligned with the orbital angular momentum even though the initial black hole spin is anti-aligned. This explains why we see a larger difference with [47] in the case with $m_{BH} = 2.5 M_\odot$ than in the other cases represented in figure 3.3, in which both approaches assume prograde orbits. To better understand this in terms of the equations of section 3.2, notice that in the BKL method we do not set a_{f} a priori, we choose the initial spin value, and the sign in equation 3.3 (the $\pm$ in the right hand side), which fixes the assumption about the orbits being prograde or retrograde. Then, the final spin obtained may or may not point in the direction of L_{orb}. If the direction of

a_{f} is inconsistent with the choice of sign in equation 3.3, then that solution must be discarded and a new solution must be found after changing the sign.

3.3.1 Comparison with Numerical Relativity

As a test of the criteria adopted in this section, we now compare with numerical relativity results shown in [64], in which the authors perform a tidal disruption study for black hole-neutron star binaries of nearly equal masses. It is shown in that work that the neutron star is not immediately tidally disrupted at the expected frequency, f_{tidal}, estimated from analytical considerations, although the tidal disruption likely sets in at that frequency. The disruption completes at a higher frequency, given by f_{cut} from table IV of [64], reproduced here in table 3.1 (see also figure 8 of that paper). Hence, there is no significant signature of the disruption until $f \approx f_{\mathrm{cut}}$.

If a given ISCO frequency estimation is reliable for determining the observability of tidal disruption, one expects that no tidal disruption should be observed at frequencies higher than that ISCO frequency estimation. In table 3.1 we compare the BKL ISCO frequencies, and the ISCO frequencies obtained in the extreme mass ratio approximations (denoted $f_{q=0}$), to the frequencies f_{cut} given in [64].

Table 3.1: Comparison of BKL frequencies, f_{BKL}, to f_{cut} for models A-F of [64], and to the frequencies obtained in the approximation of a test particle on a black hole background with mass m_{BH} ($f_{q=0}{}^{a}$), and with mass $M \equiv M_{\mathrm{BH}} + M_{\mathrm{NS}}$ ($f_{q=0}{}^{b}$). Also shown are the parameters q and M used in each case (χ_{BH} and χ_{NS} are set to 0 in all cases, as in [64]).

Model from [64]	q	$M(M_\odot)$	f_{BKL}(kHz)	f_{cut}(kHz) from [64]	$f_{q=0}{}^{a}$(kHz) ($m = m_{\mathrm{BH}}$)	$f_{q=0}{}^{b}$(kHz) ($m = M$)
A	0.327	5.277	1.38	1.16	1.11	0.83
B	0.327	5.244	1.39	1.41	1.11	0.84
C	0.328	5.311	1.37	0.92	1.10	0.83
D	0.392	4.623	1.65	1.14	1.32	0.95
E	0.392	4.594	1.66	1.40	1.33	0.96
F	0.281	5.929	1.18	1.09	0.95	0.74

We note that $f_{\mathrm{BKL}} \gtrsim f_{\mathrm{cut}}$ for all models. This result is consistent with the criteria used earlier to determine in which cases neutron star disruption could be observed. If, instead, one were to use frequencies obtained from the extreme mass ratio approximation as in [47] ($f_{q=0}{}^{a}$ in table 3.1), one could underestimate possible detections, since $f_{q=0}{}^{a} < f_{\mathrm{cut}}$ for four of the six models considered.

We also note that the total mass, $M \equiv m_{\mathrm{BH}} + m_{\mathrm{NS}}$, is sometimes used, instead of m_{BH}, as the mass of the central object when calculating the ISCO frequency in the extreme mass ratio approximation. The frequencies calculated in that way are presented as $f_{q=0}{}^{b}$ in the table. That approach underestimates even more the possible detections, since the frequencies obtained are then much lower.

3.4 Cut Off Frequencies of Post Newtonian Templates

In the implementation of matched filtering techniques, it is necessary to have an estimation of the characteristic frequency at which a given template waveform ceases to resemble the one

produced by the physical systems. Some searches for low mass binary systems of non-spinning component masses use the ISCO of a test particle orbiting a Schwarzschild black hole [57]. Other searches use the ISCOs calculated from explicit post-Newtonian energy considerations, and some abandon the use of an ISCO altogether and use the Schwarzschild light ring as a termination frequency [65].

For low mass ratio ($q \sim 0$) systems of non-spinning objects, the Schwarzschild test particle limit is a good approximation for the expected ISCO frequency since the merger product will be a Schwarzschild-like black hole. However, for systems with comparable masses and/or with spin, the true ISCO frequency may be different since the non-trivial contribution from the orbital angular momentum will have a strong impact on the final black hole's spin, and the space-time in the near merger epoch. Various post Newtonian approximations stay faithful to numerical relativity solutions until stages very close to the merger [53, 66, 67, 68, 69, 70, 71]. Most approximations stay faithful through the Schwarzschild ISCO frequency and some even beyond that point [69],

The fact that some PN approximations do remain faithful far beyond the Schwarzschild ISCO is a good motivation to examine using the ISCO frequency described in section 3.2 as the termination frequency for inspiral data analysis.

Besides the frequency obtained using a test particle on a Schwarzschild black hole, more accurate techniques exist for estimating the ISCO frequency. These are based on effective one body (EOB) calculations [65, 72, 73], which consist on solving for a test particle on an effective background, where the background is chosen (based on post Newtonian approximations) so that it incorporates features of the dynamics of a binary.

It is shown in [46] that the BKL frequency obtained in section 3.2 is consistent with some of the PN and EOB models for predicting the ISCO (see figure 2 of [46]) and is consistent with exact solutions in the test particle limit. The BKL method has the advantage of being waveform model, or fit, independent (based on first principles) and is easy to calculate.

Next, we show that the expected signal to noise ratio (SNR) for LIGO, for some total mass and mass ratio combinations, is significantly higher when using the BKL frequencies as cut off frequencies for post Newtonian templates, as compared to the expected SNR when using the Schwarzschild ISCO frequency as is done currently [57]. This means that using the BKL approach would increase the chances of detection.

When using matched filtering techniques, one needs to have a measure of the overlap between two waveforms. This overlap can be defined, given two waveforms $h_1(t)$ and $h_2(t)$, as [74]

$$O(h_1, h_2) = \frac{< h_1 | h_2 >}{\sqrt{< h_1 | h_1 >< h_2 | h_2 >}}. \tag{3.9}$$

The inner product $< | >$ is defined as

$$< h_1 | h_2 >= 4\mathrm{Re} \int_0^\infty \frac{\tilde{h}_1(f)^* \tilde{h}_2(f)}{S_n(f)} df, \tag{3.10}$$

where $\tilde{h}_i(f)$ is the Fourier transform of $h_i(t)$ and the star (*) denotes complex conjugate. The inner product is weighted by the inverse of the power spectral density of the detector noise, $S_n(f)$, which can be approximated analytically by [74]

$$S_n(f) \approx 9 \times 10^{-46} \left[\left(\frac{4.49f}{150} \right)^{-56} + 0.16 \left(\frac{f}{150} \right)^{-4.52} + 0.32 \left(\frac{f}{150} \right)^2 + 0.52 \right], \tag{3.11}$$

where f is given in Hz. The signal to noise ratio when detecting a signal $s(t)$ by means of bank templates $\{h_j\}$ is calculated as [74]

$$\text{SNR} = |O(s, h_j)|\sqrt{< h_j|h_j >}. \tag{3.12}$$

The SNR is maximized when the signal present in the data matches the filter waveform. The integrals in $< \, | \, >$ are evaluated between the low frequency sensitivity of the detector, f_{low}, and a maximum frequency, f_{final}, for which the templates are assumed to be accurate. In our case we set $f_{\text{low}} = 40\text{Hz}$ [52] and f_{final} to the frequency at the ISCO.

To compare the SNR obtained using the BKL frequency to that using the Schwarzschild frequency as cutoff, we evaluate the ratio $\text{SNR}_{\text{BKL}}/\text{SNR}_{\text{Sch.}}$ for different values of total mass, M, and mass ratio, q. We use as waveform filters second order PN templates, given by the stationary phase approximation [57] as

$$\tilde{h}(f) \propto f^{-7/6} e^{i\Psi(f;M,q)}, \tag{3.13}$$

and represent the detector data by one of these templates. Since the relevant case is for the filter that maximizes the SNR, we evaluate the SNR using the same filter that was chosen to represent the detector data. Then, the SNR ratio is

$$\frac{\text{SNR}_{\text{BKL}}}{\text{SNR}_{\text{Sch.}}} = \left(\int_{f_{\text{low}}}^{f_{\text{BKL}}} \frac{df}{f^{7/3} S_n(f)}\right)^{1/2} \left(\int_{f_{\text{low}}}^{f_{\text{Sch.}}} \frac{df}{f^{7/3} S_n(f)}\right)^{-1/2}. \tag{3.14}$$

This ratio is shown in figure 3.4, showing a significant gain for some combinations of the parameters q and M when using the BKL ISCO frequency as a cutoff.
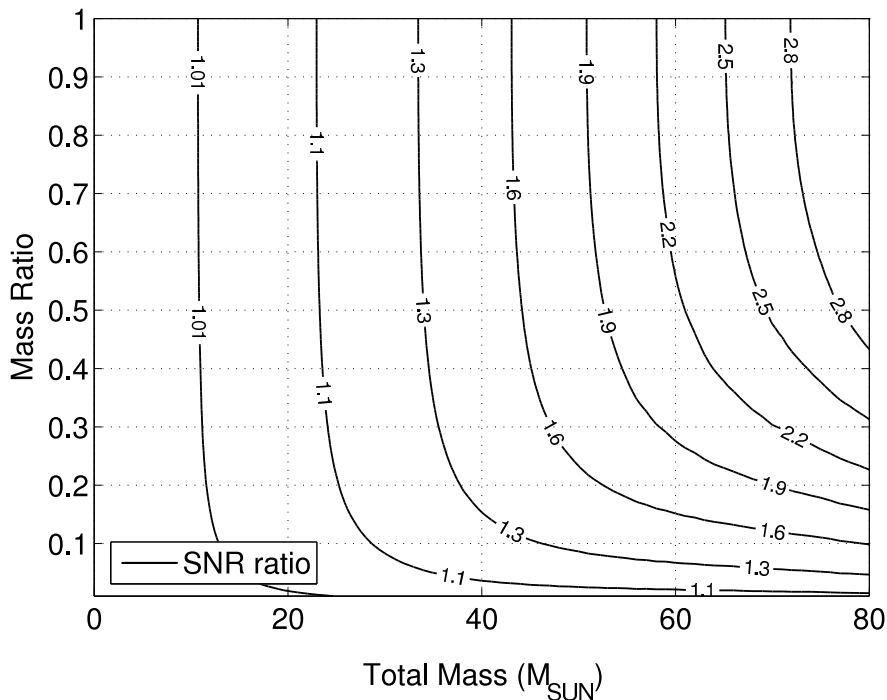
Figure 3.4: SNR ratio, defined in equation 3.14, for different values of q and M. Non-spinning case ($\chi = 0$).

Comparisons of post-Newtonian waveforms with numerical relativity results [75] show that, for $q \approx 1$, phase errors begin to accumulate for frequencies beyond the Schwarzschild ISCO frequency. That means that using one of the PN templates h as the detector data s in the calculations of the SNR (as it is done in equation 3.14) would overestimate the gain when using the BKL instead of the Schwarzschild cutoff. However, a significant gain is still obtained for some values of q and M when including possible phase errors of up to $\pm\pi$ between $f_{\text{Sch.}}$ and f_{BKL} [46] (more than 50% gain for $q > 0.5$ and $M > 50 M_\odot$).

3.5   Conclusions

In this chapter we showed a method to estimate the characteristic frequency for the end of the inspiral phase of a compact binary coalescence. The estimation takes into account the orbital angular momentum, mass ratio and individual spins in the case they are aligned (or anti-aligned) with the orbital angular momentum. This method is an extension of that used in [58] to estimate the final spin of the merged binary. As shown there, it can be extended to account for arbitrary inclinations of the individual spins.

We showed how adopting this frequency as that marking the end of the inspiral phase has implications on the ability to probe tidal disruption, providing a better estimate of the range of BH-NS binaries for which the disruption is more plausible to be measured. We also showed that the frequencies obtained in this way are consistent with results from numerical relativity.

Additionally, our estimation of the frequency at the ISCO provides a good cut off frequency for the post-Newtonian templates used in data analysis to model the inspiral part of the waveform, resulting in an increased signal to noise ratio as compared to the approach that uses the ISCO of a test particle on a Schwarzschild background.

Chapter 4
Binary Black Hole Merger Effects on Circumbinary Disks

As discussed in chapter 1, the merger process of a binary black hole system can have a strong impact on a circumbinary disk. In this chapter we study the effect of both central mass reduction (due to the energy loss through gravitational waves) and a possible black hole recoil (due to asymmetric emission of gravitational radiation). For the mass reduction case and recoil directed along the disk's angular momentum, oscillations are induced in the disk which then modulate the internal energy and bremsstrahlung luminosities. On the other hand, when the recoil direction has a component orthogonal to the disk's angular momentum, the disk's dynamics are strongly impacted, giving rise to shocks. The shock heating leaves its signature in the total internal energy and bremsstrahlung luminosity. Interestingly, for the range of kick velocities considered (in all cases below the smallest orbital velocity in the disk) we observe a common, characteristic pattern in the disk's internal energy fluctuations, where variations in kick velocity simply provide a phase offset in the characteristic pattern. Observations of such a signature could yield a measure of the kick velocity through electromagnetic signals, or simply just be an independent sign of a merger. The work shown in this chapter resulted in a publication [76].

4.1   Introduction

The study of a number of astrophysical systems will soon add gravitational wave astronomy as a new tool to complement observations in the electromagnetic band. Since most systems capable of producing detectable gravitational waves will also radiate strongly in the electromagnetic band (see, e.g., [77, 78]), combining information from both spectra will allow for a richer description of these systems. Furthermore, the complementary nature of observation in both bands will help the detection enterprise as a signal in one band will help follow up studies in the other (see, for instance, [2, 79].)

   Among interesting possible sources of strong signals in both spectra, the collision of a binary black hole system within a circumbinary disk presents the possibility of a detection of gravitational waves (as the black holes merge), which will be followed by electromagnetic signals emitted by the disk as its dynamics are affected in the process [5]. This scenario is common in nature, since massive black holes exist in the core of most galaxies and galaxies undergo mergers throughout their evolutionary path. As galaxies merge, they produce a binary black hole in the newly formed galaxy which eventually collide as their orbit shrinks through several mechanisms. As discussed in [5], a circumbinary disk is formed as the binary hollows out the surrounding gas, and the disk becomes mostly disconnected from the binary's dynamics [80, 81]. Afterwards, while the disk remains essentially frozen, the black holes' orbits continue to shrink until they merge.

   The merger process gives rise, in particular, to two relevant effects that will perturb the disk (see, e.g., [5, 82]). One is related to the final mass of the black hole, which is less than the initial total mass as the system radiates energy via gravitational waves. The other one

is a consequence of the radiation of linear momentum, which, if asymmetric (as in the case of an unequal mass binary, or asymmetric individual angular momenta of the black holes), induces a nontrivial recoil on the nascent black hole. This recoil effect has been predicted before through perturbative analysis of Einstein equations [83, 84], and recent numerical simulations implementing the equations in full show even higher recoil velocities are possible [85, 86, 87, 88, 89, 90, 91, 92, 93]. The largest recoil velocities found correspond to mass ratios close to 1 and spins lying anti-aligned on the orbital plane. In the case of quasi circular orbits, recoil velocities up to about 4000 km/s have been calculated [87]. However, most of the black hole collisions occurring in nature are expected to produce kicks of about 500 km/s or less, since larger kicks would occur only in the case of nearly equal masses [94].

As a result of both effects mentioned above, namely, mass reduction and recoil, the fluid dynamics in the disk is modified and shocks may be induced. The shocks' energy can then heat the gas, which can produce electromagnetic flares. For the recoiling black hole case, prior studies, which employ simulations of collisionless particles in Keplerian orbits forming a flat (zero height) disk, predict emissions ranging from UV to X-rays [95, 96] or in the infrared [97] if this radiation is assumed to be absorbed before leaving the disk and re-emitted. Since these studies employ a particle description of the fluid, they can not fully capture the development (and hence influence) of shocks, which must be estimated by detecting collisions between particles. A recent work [98] adopted a field description for the fluid and studied the impact of a mass reduction in a pseudo-Newtonian potential to account for an innermost stable circular orbit (ISCO) at $r = 6M$ (which corresponds to the ISCO of a non-spinning black hole, while this is a rather uncommon output [99, 100, 101, 102] in the merger of two black holes. The spin value will play a relevant role mainly if accretion develops.) Based on computations of bremsstrahlung luminosity, that work predicts a decrease in luminosity as the fluid orbits adjust to the reduced gravitational potential.

In this work we study the effects on the disk by also considering a perfect fluid but in our case we do so employing the fully relativistic hydrodynamic equations in a background space-time. Thus, we are able to examine effects of spin, mass reduction and accretion, and comment on the relevance of different processes. In particular, our studies indicate that a significant distortion of the disk develops as time progresses when the kick has a component perpendicular to the disk's axis and that qualitatively similar features are present in all these cases.

In section 4.2 we describe our formulation of the problem and initial configuration. Section 4.3 offers a review of the numerical approach. We discuss the observed dynamics in the disk after the merger has taken place in section 4.4, taking into consideration the effect of mass reduction and different recoil velocities. Section 4.5 concludes and offers some further considerations.

Unless otherwise specified, we use geometrized units, where $G = c = 1$, and sum over repeated indexes. Greek-letter indices range from 0 to 3.

4.2   Physical Setup

To explore the effects of the black hole merger in the dynamics of the accretion disk, we concentrate, in particular, in the post-merger stage –when the main burst of gravitational radiation has passed through the disk and this has settled down to a quasistationary state–.[1] To simulate a black hole formed through the merger process and account for the main effects of mass loss or recoil, we either consider a reduction in the mass of the black hole by 5%, or apply a boost to the black hole in a given direction. In the latter case, it is easier to adopt the black hole's rest frame

---

[1]Studies of possible pre-merger effects are presented in, e.g., [103, 104].

and apply the boost to the fluid variables (in the opposite direction) describing the disk, which is represented by a stationary toroidal solution of the fluid equations in a Kerr background. Thus, starting with a stationary torus on a Kerr background, we perform a Lorentz boost with velocity $-\vec{v}_{\text{kick}}$ on the disk. We employ this boost to transform the fluid's 4-velocity u^μ and magnetic field 4-vector b^μ when considering the recoil case.

The toroidal solutions are constructed following an approach similar to that in [105], adapted to the ingoing Kerr-Schild coordinates adopted in our studies, and with a different choice of specific angular momentum for the fluid for easier comparison with previous work in the absence of magnetic fields (In particular, we verify that identical solutions to those of [106] are obtained if the magnetic field is set to zero). In our case, we adopt the more standard definition, $l \equiv -u_\phi \left(u_t\right)^{-1}$ (see below), to allow for an easier comparison with previous work in the absence of magnetic fields. Notice, however, that all definitions are consistent, in the sense that they reduce to the familiar expression, $L/m = rv$, in the classical limit. While in the current work we do not simulate scenarios that include a magnetic field, we discuss the construction of initial data that allows for doing so for future reference. In the rest of this section we first review the main steps in this construction. Then we show how the stationary tori obtained are used to construct appropriate initial data for the different cases evolved in our numerical simulations.

4.2.1   Toroidal Stationary Solutions

We now derive toroidal stationary solutions for ideal magnetohydrodynamics (MHD) in a general relativistic space-time. The solutions obtained are then modified and used, as explained in 4.2.2, to setup initial data for a merged binary black hole-disk system.

The stress-energy tensor for ideal MHD can be written as

$$T_{\mu\nu} = \left(\rho h + b^2\right) u_\mu u_\nu + \left(P + b^2/2\right) g_{\mu\nu} - b_\mu b_\nu, \tag{4.1}$$

where ρ, P, and u^μ are the fluid's density, pressure and 4-velocity, respectively, b^μ is the magnetic field 4-vector, and h is the specific enthalpy, defined as

$$\rho h = \rho(1 + \epsilon) + P, \tag{4.2}$$

where ϵ is the specific internal energy density.

For the construction of initial data, we work with cylindrical coordinates (t, r, ϕ, z) and make the assumption that the space-time is stationary and axially symmetric. We adopt coordinates adapted to these symmetries, so that only the t- and ϕ-components of u^μ and b^μ are nonzero[2].

The fluid equations are obtained from

$$\nabla_\mu T^\mu{}_\nu = 0, \tag{4.3}$$

together with the continuity equation $\nabla_\mu(\rho u^\mu) = 0$ (which is trivially satisfied under our assumptions). After some lengthy manipulation, equation (4.3) can be reduced to the integral equation

$$\int u^t u_\phi \, d\left(\frac{u^\phi}{u^t}\right) - \ln u^t + \int \frac{1}{h\rho} \, dP + \int \frac{1}{2\rho h D} \, d(b^2 D) = \text{const.}, \tag{4.4}$$

where $D = |g_{tt}g_{\phi\phi} - g_{t\phi}^2|$. This equation can be integrated after imposing further conditions that fix relationships between the fluid variables as discussed below.

---

[2]Where t and ϕ are coordinates associated with the mentioned symmetries.

First, we fix a relationship between the velocity components. This can be accomplished by requiring that the specific angular momentum l satisfies

$$l \equiv -\frac{u_\phi}{u_t} = \text{const.} \tag{4.5}$$

Second, we assume an isentropic fluid, imposing $dh = \rho^{-1}dP$, which allows us to integrate one of the terms out. An equation of state that satisfies this condition is that of a polytrope

$$P = \kappa\rho^\Gamma. \tag{4.6}$$

In this case, the specific internal energy density can be calculated as

$$\epsilon = \frac{\kappa}{\Gamma - 1}\rho^{\Gamma-1}. \tag{4.7}$$

We adopt this condition only to obtain the stationary solutions for initial data. The fluid's entropy will change after the kick and so we adopt, during the evolution, a Γ-law equation of state

$$P = (\Gamma - 1)\rho\epsilon \tag{4.8}$$

with $\Gamma = 5/3$, considering the gas as being monoatomic.

Finally, we impose a convenient expression for b^2 in terms of other variables to integrate the last term:

$$b^2 \, D = C(\,\rho h \, D)^q, \tag{4.9}$$

where C and $q > 1$ are arbitrary constants.

After integrating equation (4.4), we use (4.6) and (4.7) to eliminate ρ and ϵ and obtain an algebraic equation for P, of the form

$$F(P, g_{\mu\nu}, l, C, q) = F_0, \tag{4.10}$$

where F_0 is a constant of integration. This equation can be solved analytically in the absence of magnetic field ($b^2 = 0$), otherwise a straightforward numerical integration can be set up to obtain the solution. The boundary of the torus is determined by setting $P = 0$, obtaining an expression of the form

$$f(g_{\mu\nu}, l) = F_0, \tag{4.11}$$

which, through the dependence of $g_{\mu\nu}$ on the coordinates, is an implicit surface equation. Notice that it is independent of both C and q so that the location of the disk's boundary is independent of the magnetic field. The solutions obtained may be toroidal as well as spheroidal, depending on the values of l and F_0.

Once P is known, one can use once again equations (4.6) and (4.7) to recover ρ and ϵ. The velocity u^μ is obtained from equation (4.5) together with the normalization condition $u^\mu u_\mu = -1$. Finally, the magnetic field b^μ is determined by equation (4.9) together with the relation $b^\mu u_\mu = 0$ (see [107]). The magnetic field is always zero at the surface of the disk (from equation (4.9)), and one can control how rapidly it decays to zero with the parameter q, and its maximum magnitude with C.

4.2.2 Initial Data: Set Up and Properties

To study the effects of mass loss and recoil, we start by constructing stationary tori (as shown in 4.2.1), and then perform one of two modifications before evolving the system: (i) For the mass loss case, we simply set, for the evolution, a black hole mass smaller than that used to obtain the stationary disk solution. (ii) For the recoil case, we perform a Lorentz boost on the fluid variables with respect to the stationary system of the background black hole.

Certainly, the parameter space is too vast to allow an exhaustive computational study. Therefore, we mainly concentrate here on varying the most relevant parameters, i.e., the kick magnitude and direction and study a few other cases varying the spin parameter to verify our results are qualitatively the same. And we study one case of mass loss, in which the black hole mass is reduced by 5%. Notice that variations with respect to the spin parameter a should not lead to significant qualitative differences unless accretion develops, as the disk's inner edge is located sufficiently far away for its influence to be of higher order. This intuitive observation is confirmed by our simulations.

A representative example of the toroidal configurations used is shown in figure 4.1. The
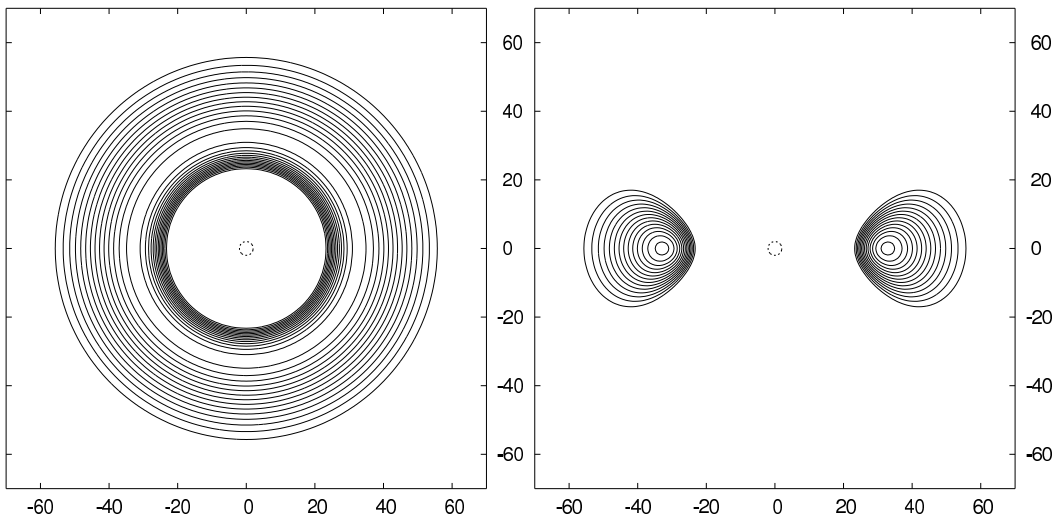
Figure 4.1: Representative example of the toroidal initial configurations, showing the density at the equatorial plane (left panel), and at a meridional plane (right panel). The dashed line indicates the location of the event horizon.

toroidal solutions employed in this work correspond to specific angular momentum $l/M = 6$, spin parameter $a/M = 0.5$ (except when analyzing the solution's dependence on the spin where we also consider $a/M = 0.9$). The sign convention used for the black hole spin and disk's angular momentum is so that positive values implies they point in the positive z-direction. Also, we fix the magnetic field parameter $C = 0$ (so that $b = 0$), and choose F_0 so that the inner edge of the disk is located at $r_{\mathrm{in}} = 20M$. With this choice of parameters, the outer edge is located at $r_{\mathrm{out}} = 60M$ and the maximum pressure in the disk lies at $r_{\mathrm{m}} = 32M$. Figure 4.1 shows a contour plot of the density. The pressure is qualitatively similar and hence no plot is shown here (see equation (4.6)). The fluid's orbital velocity, represented in figure 4.2, is then $v_{\mathrm{orb}} = 0.28$, 0.17 and 0.10 at r_{in}, r_{m} and r_{out} respectively. Thus, the orbital period at r_{m} is $P_{\mathrm{m}} = 1220M$. The figure also shows, for comparison purposes, the Keplerian velocity, i.e.: the velocity of test particles on the black holes' spacetime. Notice that, as expected, the fluid velocity at the annulus of zero pressure gradient, $r = r_{\mathrm{m}}$, coincides with the Keplerian value, while it is smaller

48

for $r > r_{\mathrm{m}}$, where the gradient points inwards, and larger for $r < r_{\mathrm{m}}$, where the gradient points outwards. The sound speed has a maximum value $\lesssim 0.05$ close to r_{m}, and drops somewhat abruptly to zero at the boundary of the torus. All fluid elements in the torus have an orbital speed much greater than the highest kick velocity adopted in this work, i.e., 0.01 (3000 km/s in MKS units), and so will remain bound to the black hole in all cases considered.[3] In fact, the binding energy per unit mass at the surface of the torus is 0.0121 (or, in non-generalized units, $0.0121c^2$), which implies a escape velocity of 0.155.
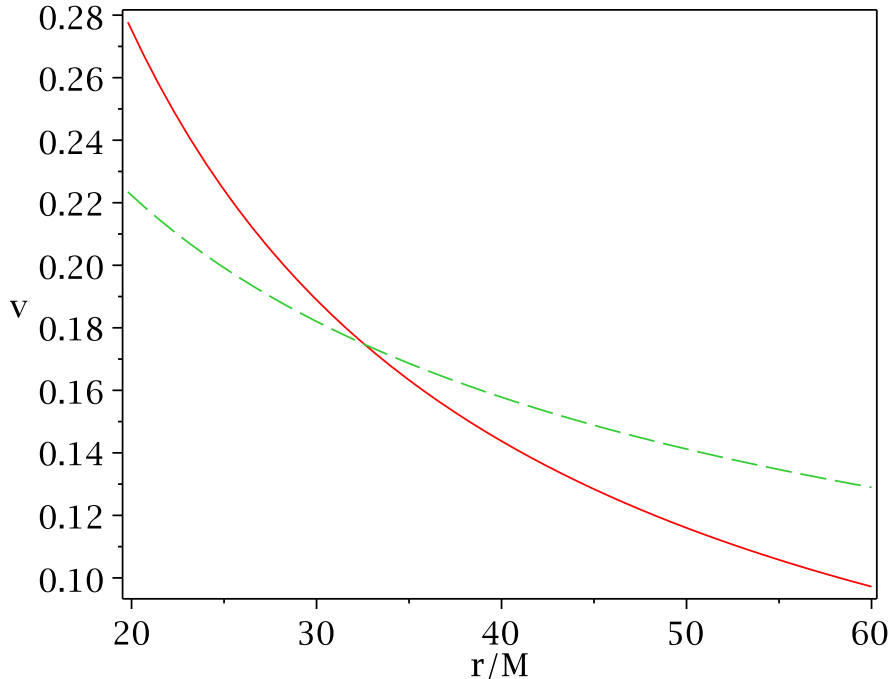
Figure 4.2: Orbital velocity of the fluid (continuous red line), and velocity of test particles in circular orbits (dashed green line) at the plane $z = 0$. The fluid's velocity is approximately independent of z, with a maximum variation smaller than 1% along the z-direction at any given radius.

Throughout the rest of this chapter, unless otherwise specified, all kick orientations mentioned refer to the kicks (or Lorentz boosts) applied to the disk, which would correspond to the black hole being kicked in the opposite direction. The density plots shown are in the black hole's reference frame, too.

4.2.3 Some Considerations about Rescaling the Solutions

Throughout most of this chapter we only show relative values of density, pressure and other quantities (for instance, we usually normalize them by their initial value.) We do so because these quantities can actually be rescaled after obtaining a solution, and hence we can use an arbitrary scaling when running the simulations. The results of this work are expressed in terms of normalized quantities (see section 4.4), that are independent of the scaling used.

Additionally, the fluid fields and calculated energies are represented as functions of x^i/M and t/M, allowing to rescale the black hole mass together with the coordinates, without affecting

---

[3]For comparison purposes we have also employed the unrealistic value of 9000 km/s.

their form as functions of x^μ/M (see below).

These two scalings can be done independently. This is valid because we use the Cowling approximation (fixed spacetime background), so a scaled stress-energy tensor does not fix the space-time scaling through equation 1.2.

To clarify these ideas, let us consider the equations being solved, equations (1.2) and (4.3), with (4.1), (4.2), (4.8) and $\nabla_\mu \rho = 0$. Assuming that the fields

$$V \equiv [\rho, P, u^\mu, b^\mu], \quad g_{\mu\nu} \tag{4.12}$$

are a solution of this system, we define a new set of fields,

$$\tilde{V} \equiv [\lambda\rho, \lambda P, u^\mu, \sqrt{\lambda}b^\mu], \quad \tilde{g}_{\mu\nu}, \tag{4.13}$$

where λ is a scaling factor. Plugging these new variables into the equations we obtain:

$$G_{\mu\nu}(\tilde{g}) = 8\pi\tilde{T}_{\mu\nu}, \tag{4.14}$$

$$\tilde{\nabla}^\mu\tilde{T}_{\mu\nu} = 0, \tag{4.15}$$

$$(\lambda P) = (\Gamma - 1)(\lambda\rho)\epsilon, \tag{4.16}$$

$$\tilde{\nabla}_\mu(\lambda\rho) = 0, \tag{4.17}$$

where

$$\tilde{T}_{\mu\nu} \equiv \left(\lambda\rho h + (\sqrt{\lambda}b)^2\right) u_\mu u_\nu + \left((\lambda P) + (\sqrt{\lambda}b)^2/2\right) \tilde{g}_{\mu\nu} - (\sqrt{\lambda}b_\mu)(\sqrt{\lambda}b_\nu)$$
$$= \lambda\left[\left(\rho h + b^2\right) u_\mu u_\nu + \left(P + b^2/2\right) \tilde{g}_{\mu\nu} - b_\mu b_\nu\right], \tag{4.18}$$

and $\tilde{\nabla}$ is the covariant derivative associated with the metric $\tilde{g}$. (Note that in equation 4.18 $\tilde{g}$ appears not only explicitly but also implicitly as it is used to lower indices.) Since we use the Cowling approximation, instead of equation (4.14) we actually have $G_{\mu\nu}(\tilde{g}) = 0$. Hence, the evolution equation for $g_{\mu\nu}$ is unchanged by the fluid scale factor λ, so we can just set $\tilde{g}_{\mu,\nu} = g_{\mu,\nu}$ (and hence $\tilde{\nabla} = \nabla$), which implies that $\tilde{T}_{\mu\nu} = \lambda T_{\mu\nu}$. Thus, since equation (4.15) is homogeneous, it is satisfied for U as long as it is satisfied for the original fields V. The same applies for equations (4.16-4.17).

Summarizing, we saw that the set $\{\tilde{V}, g_{\mu,\nu}\}$ is a solution as long as the set $\{V, g_{\mu,\nu}\}$ is a solution. This means that we can scale the fluid variables, while keeping the same space-time background.

Recalling the analysis of section 4.2.1, where we assumed the condition $P = \kappa\rho^\Gamma$ to obtain stationary solutions, we see that κ scales as $\tilde{\kappa} = \lambda^{(1-\Gamma)}\kappa$.

On the other hand, we can also rescale the black hole mass and coordinates as $\tilde{M} = \alpha M$, $\tilde{x}^\mu = \alpha x^\mu$. The fluid fields are not affected by this scaling, in the sense that they are invariant as functions of x^i/M and t/M. (Note that in this work we study cases without magnetic field. Otherwise, b^μ scales as α^{-1}, so $\tilde{T}_{\mu\nu} = \alpha^4 T_{\mu\nu}$ and the fluid equations remain invariant.) In the simulations we simply adopt $M = 1$.

4.3 Overview of the Numerical Approach

As mentioned earlier, we neglect the self-gravity of the fluid and evolve the fluid equations on a Kerr black hole background (Cowling approximation). This approximation will be valid as

long as the disk's mass is much smaller than the black hole's mass. However, notice that, as explained in section 4.2.3, we do not need to ensure that the ratio of disk mass to black hole mass is small at the moment of running the simulations, and these can be scaled afterwards if needed.

To evolve the fluid on a fixed space-time background we implement the general relativistic MHD equations using the high resolution shock capturing module described in [107, 108]. This module is implemented over the `HAD` computational infrastructure [109, 110] that provides parallelization and adaptive or fixed mesh refinement on a Cartesian 3D grid.

The shock capturing method used in this code is based on expressing the fluid equations in a conservation form (except for additional source terms that do not depend on derivatives of the fluid variables). To that end, the fluid variables are transformed back and forth between conservative and primitive variables. We show the form of these equations and the transformation from primitive to conservative variables in section 4.3.1.

Although the conversion to conservative variables is straightforward, the transformation that gives the primitive variables in terms of the conservative variables is transcendental, so a numerical root solver is used. This introduces unphysical values in regions of very low density or pressure, representing a problem specially in vacuum regions, which are present in most astrophysical scenarios, as is the case with the one we study in this work. We explain how we deal with this issue in section 4.3.2 below.

The black hole's singularity is excised from the computational domain using a cubic excision region inside the event horizon, so that it is causally disconnected from the outside solution (see section 1.1.1). Although the grid points located inside the event horizon are causally disconnected from the outside points at the analytical level, the very strong fields (and gradients) in that region can cause the code to crash. Furthermore, numerical errors may propagate out into the exterior region. For that reason it is preferable to adopt an excision region as large as possible, while still being inside the event horizon. We set its boundaries at $\pm 1.1M$ in all three directions. In our particular scenario we also needed to introduce a slight modification of the hydrodynamic equations inside the horizon, introducing a damping term, to improve the fluid's behavior close to the excision region. This is explained in more detail in section 4.3.3.

The code used in our studies has been previously tested and employed in a variety of scenarios, e.g., [108, 111, 112]. For our specific application we have verified that, in the absence of a kick or mass reduction, the disk remains fairly stationary as expected, except only for small perturbations caused by the accumulation of numerical error during the evolution. This small perturbations remain much smaller than the effects studied in this work. Additionally, we have verified convergence by comparing results obtained with three different resolutions in the case of a kick velocity of 3000 km/s perpendicular to the axis of rotation. The convergence rate measured at different locations varies between first and third order depending on the presence of shocks.

After setting the initial data for a boosted disk or a reduced mass black hole as explained previously, such configurations are evolved on a computational domain given by $[-150\,M, 150\,M]$ in the x- and y-direction, where M is the black hole mass, centered at $x = y = z = 0$, and $[-100\,M, 100\,M]$ in the z-direction (since the disk lies on the $x - y$ plane). Due to the dynamics involved in this work, it is only necessary to use a fixed refinement hierarchy, covering with finer grids the (central) region containing the disk and black hole, and increasingly coarser grids in the outer regions in order to locate the boundaries far away at a low computational cost.

The simulations were run on systems from the LONI [113] network (mostly Queen Bee) using 32 processors, and taking approximately two weeks for each simulation.

4.3.1 Fluid Equations

As mentioned earlier, to evolve the fluid equations in the numerical code, they are first converted to a "conservative" form, defining a new set of fluid variables. This is described in detail in [107, 108] and, in more general grounds, in [114]. For reference, we show here the transformation and resulting equations, omitting for simplicity the magnetic field, which is set to zero in our simulations.

We begin by defining the quantities

$$h_e \equiv \rho(1 + \epsilon) + P, \tag{4.19}$$

$$W \equiv -n^a u_a, \tag{4.20}$$

$$v^i \equiv \frac{1}{W} h^i{}_j u^j, \tag{4.21}$$

where h_{ij} is the 3-metric on the space-like hypersurfaces of the foliation, n^a is the unit normal to the hypersurfaces, and v^i is the spatial coordinate velocity of the fluid.

Then, we define the conservative variables $\{D, S_i, \tau\}$ as

$$D = W\rho, \tag{4.22}$$

$$S_i = h_e W^2 v_i, \tag{4.23}$$

$$\tau = h_e W^2 - P - D, \tag{4.24}$$

It is also convenient to define densitized conserved variables as

$$\tilde{D} = \sqrt{h}\, D, \quad \tilde{S}_i = \sqrt{h}\, S_i, \quad \tilde{\tau} = \sqrt{h}\, \tau, \tag{4.25}$$

where $h = \det(h_{ij})$ is the determinant of the 3-metric. The numerical code has the capability of evolving either the conserved variables or the densitized conserved variables. In our simulations we adopted the latter, since that resulted in improved code robustness.

The fluid equations then take the form

$$\partial_t \tilde{D} + \partial_i \left[\alpha \tilde{D} \left(v^i - \frac{\beta^i}{\alpha} \right) \right] = 0, \tag{4.26}$$

$$\partial_t \tilde{S}_j + \partial_i \left[\alpha \left(\tilde{S}_j \left(v^i - \frac{\beta^i}{\alpha} \right) + \sqrt{h}\, P\, h^i{}_j \right) \right] = \alpha\, {}^3\Gamma^i{}_{jk} \left(\tilde{S}_i v^k + \sqrt{h}\, P h_i{}^k \right)$$
$$+ \tilde{S}_a \partial_j \beta^a - \partial_j \alpha\, (\tilde{\tau} + \tilde{D}), \tag{4.27}$$

$$\partial_t \tilde{\tau} + \partial_i \left[\alpha \left(\tilde{S}^i - \frac{\beta^i}{\alpha} \tilde{\tau} - v^i \tilde{D} \right) \right] = \alpha \left[K_{ij} \tilde{S}^i v^j + \sqrt{h}\, K P - \frac{1}{\alpha} \tilde{S}^a \partial_a \alpha \right], \tag{4.28}$$

where α and β^a are the lapse and shift functions, respectively, ${}^3\Gamma^i{}_{jk}$ is the Christoffel symbol associated with h_{ij}, K_{ij} is the extrinsic curvature and $K = K^i{}_i$.

Finally, the system of fluid equations is closed with the ideal gas equation of state,

$$P = (\Gamma - 1)\, \rho\epsilon. \tag{4.29}$$

4.3.2 Setting an Atmosphere

As mentioned earlier, the transformation from conservative to primitive variables introduces unphysical values in regions of zero or very low density or pressure. To address this issue it

is common practice to implement a "floor" or "atmosphere", which consist of reseting a field to some small value whenever it falls bellow that value. The floor or atmosphere are chosen so that they do not significantly affect the evolution of the physical system, while allowing the numerical code to work properly. The appropriate values to use depend on the particular case to study.

We start by implementing an atmosphere, setting initially the density and pressure to some small value outside of the disk. Since during the evolution this variables can eventually decrease to a much smaller value at some grid point, every time they fall below a given floor they are reset to the value of that floor. Although the initial atmosphere and floor can in principle be different, we set them to the same value in this work. The atmosphere must be chosen wisely: The larger it is, the better the code will behave, but it must be small enough so that it does not affect the physical scenario one wants to study.

By trial and error we first found that the simulations run without much trouble if we set an atmosphere six orders of magnitude below the initial maximum density. To see if this value was small enough to not alter the dynamics of the physical system, we then run test simulations with atmospheres seven and eight orders of magnitude below that maximum, and evaluated how the differences in the low density regions affected the evolution of the higher density regions, i.e., the disk itself. As is illustrated in figure 4.3. we found no significant difference among the three cases when comparing regions where the density was above 10^{-4} times the initial maximum value.
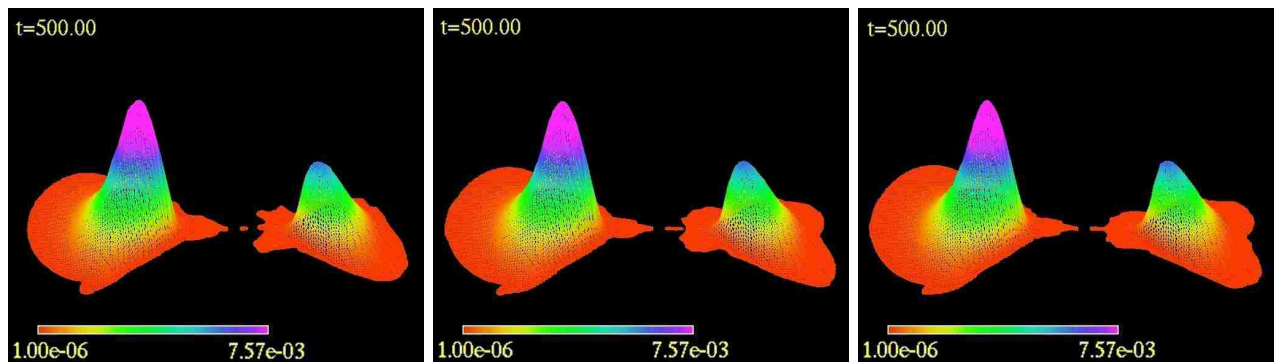
Figure 4.3: Comparison of simulations using different values for the atmosphere. The figures show the density at $t/M = 500$ on the $y - z$ plane, with atmospheres set (from left to right) at six, seven and eight orders of magnitude below the mean density. In this figures we only show all density values that are at least two orders of magnitude above the atmosphere. We can see that there is no significant difference in the evolution of those higher density regions, which represent the physical system.

Hence, after seeing that an atmosphere six orders of magnitude below the maximum initial density is small enough, we adopted this value for all our simulations from there on.

4.3.3   Damping Inside the Event Horizon

For the particular case of the black hole-disk simulations, some modifications needed to be implemented to improve the robustness of the code. This is due to the increase of pressure and velocity of the low density "atmosphere" in the region inside and close to the black hole horizon, and to the very long simulations involved. Our approach was to add a damping term to the

fluid equations. Given an equation of the form[4]

$$\frac{\partial U}{\partial t} + \frac{\partial F(U)}{\partial x} = S(U),$$ (4.30)

where U represents the fluid (conservative) variables, we modify it in order to include a damping term:

$$\frac{\partial U}{\partial t} + \frac{\partial F(U)}{\partial x} = S(U) - f(r)(\Delta x)^p (U - U_0),$$ (4.31)

$$f(r) = \begin{cases} A\,|r - 2M|^n & r < 2M \\ 0 & r \geq 2M \end{cases},$$ (4.32)

where p, A and n are free parameters and U_0 is set to zero in the case of the velocities and magnetic field, and to the value of the atmosphere for the density and pressure. Δx is the grid spacing in that region. The function $f(r)$ is chosen so that it decreases smoothly with r, ensuring more damping in the regions closer to the excision, and is zero for $r > 2M$ so that the exterior of the black hole is causally disconnected from the effect of this extra term. The coefficient $(\Delta x)^p$ ensures that the damping term converges to zero and will not modify the convergence rate as long as one chooses p to be greater than or equal to the order of convergence of the code. The particular values adopted were $p = 4$, $A = 100$ and $n = 2$.

This modification greatly improved the robustness of the code. Figure 4.4 illustrates the effect of the damping term, showing how "spikes" develop close to the excision (causing the simulations to eventually crash) if no damping is used, and how they go away when using a damping term, while the exterior region remains unchanged.
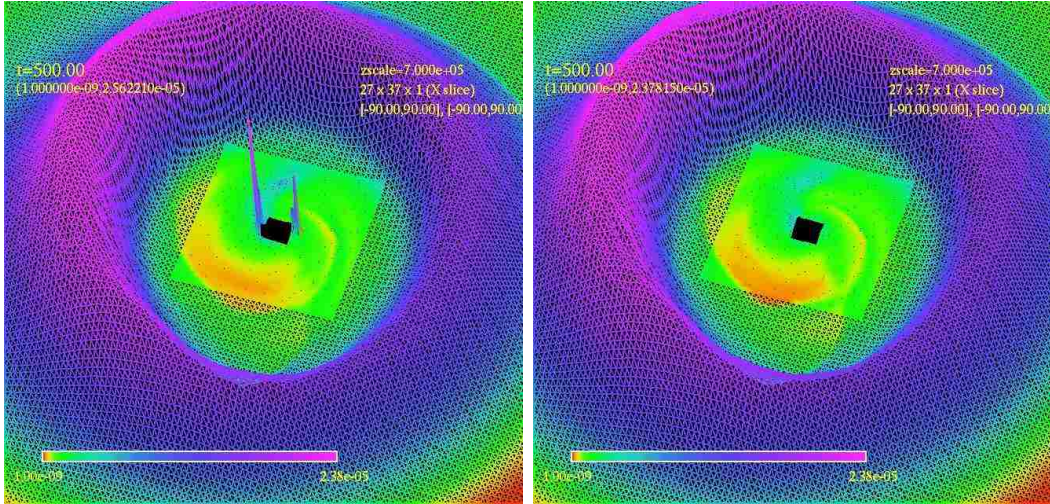
Figure 4.4: Pressure on x-y plane at $t/M = 500$. The black square seen in this 2D slice is the excision region (a cube in the 3D grid), contained entirely inside of the event horizon. *Left panel*: Without damping. *Right panel*: With damping. We clearly see how the simulation improve near the excision region, while the exterior regions remain unchanged.

---

[4]For clarity we use here a simple expression to represent the fluid equations, see section 4.3.1 or [107, 108] for the full equations.

4.4 Results

4.4.1 Diagnostic Quantities

We monitor the fluid's behavior by examining the dependence of the primitive values as different physical parameters are varied. Ultimately, our goal is to understand possible electromagnetic signals emitted by the system as the disk' dynamics is affected. At present, our code does not incorporate radiation transport; thus, a direct computation of these signals is not possible. Therefore, we concentrate on related quantities, which, when combined with a suitable model, can be tied to possible emissions. In particular, we compute (an approximation to) the temperature, T, the total internal energy, U, and bremsstrahlung luminosity, L_B, as [115, 116]

$$T \propto P/\rho, \tag{4.33}$$

$$U \propto \int \rho \epsilon dV, \tag{4.34}$$

$$L_B \propto \int \rho^2 T^{1/2} dV. \tag{4.35}$$

Notice that unless the disk is optically thin, the bremsstrahlung luminosity need not capture the luminosity resulting from shocks and shock heating. While the bremsstrahlung luminosity is a good measure of the energy exchanged between atoms and the radiation field, it does not take into account how this energy can be radiated out of the disk. In the absence of a more refined model, the qualitative features of the true radiative behavior may be estimated simply by a black body assumption. We monitor the internal energy for this purpose and also the bremsstrahlung luminosity to obtain a measure of the mentioned energy exchange (as well as to compare with results presented in [98]).

The gas temperature, equation (4.33), was estimated as follows: We assume an ideal gas equation of state,

$$P = nk_B T, \tag{4.36}$$

where n is the particle number per unit volume and k_B the Boltzmann constant. In terms of the density of the gas, equation (4.36) reads

$$P = \frac{\rho}{\mu m_H} k_B T, \tag{4.37}$$

where m_H is the mass of the hydrogen atom (that can be approximated by the mass of the proton, m_p), and μ is the mean molecular weight. Assuming our gas consists of fully ionized hydrogen we have $\mu = 1/2$, and equation (4.37) becomes

$$k_B T = \frac{1}{2} m_p \frac{P}{\rho}. \tag{4.38}$$

In terms of geometrized units (g.u.), where $(P/\rho)_{g.u.} = c^{-2}(P/\rho)$ (see the appendix in [6]), we obtain

$$k_B T = \frac{1}{2} m_p c^2 \left(\frac{P}{\rho}\right)_{g.u.} = 469 \text{ MeV} \left(\frac{P}{\rho}\right)_{g.u.}, \tag{4.39}$$

or

$$T = 5.444 \times 10^{12} \text{ K} \left(\frac{P}{\rho}\right)_{g.u.}. \tag{4.40}$$

We include here these full expressions for future reference. However, notice that we only need equation 4.33 to calculate the normalized results shown in most of this chapter.

4.4.2 Axisymmetric Cases: Black Hole Mass Loss and Kick along the Disk's Angular Momentum

As a first step we consider the effect of black hole mass loss and that of a kick along the disk's orbital angular momentum. The former entails solely decreasing the mass of the black hole, while for the latter the mass is unchanged but a kick is introduced along the z axis. In both cases, the underlying axisymmetry of the problem is not broken, which, as we will see later, is a key issue.

For the mass loss case, we employ a toroidal solution corresponding to a black hole of mass M_0 for the initial data, and set $M = 0.95M_0$. The dynamics of the disk with either a reduced mass or a kick along the z axis behave in a rather smooth manner. For the mass reduced case, radial oscillations are induced as the different fluid elements follow their corresponding epicycles. For the case with a recoil velocity, further oscillations are generated by induced motions in the z axis as illustrated in figure 4.5. Indeed, the recoil motion of the black hole introduces a time-dependent vertical component of the black hole's gravitational pull on the disk. Using Newtonian mechanics for simplicity and ignoring pressure forces, one can show that a particle on a circular orbit with velocity v_{orb}, after a vertical kick of magnitude v_{kick} only reaches a height $z = \sqrt{2}R(v_{\mathrm{kick}}/v_{\mathrm{orb}})$ above the original plane before turning around. Since v_{kick} is the same for all disk radii, the vertical displacement is minimal at r_{in} and maximal at r_{out}. This results in a flexing axisymmetric mode, with the outer edge swinging the most. This can be seen in figure 4.5 if one defines the "midplane" of the disk by joining points at which the contours are vertical. This argument ignores pressure, but pressure gradients are unlikely to be very important away from shocks, and the behavior is qualitatively the same. Because all particles on a given radial annulus are kicked simultaneously, they remain in phase with each other and the flexing mode is naturally excited. Note that maximum compression occurs twice per orbital period, so this flexing mode is visible in both internal energy and bremsstrahlung at a frequency of about twice the orbital frequency (See figures 4.6 and 4.7).

Most importantly, in either case no significant shocks are developed during the time of these simulations ($\simeq 6P_{\mathrm{m}}$). The observed smooth behavior translates into a rather monotonic behavior in our diagnostic variables. Figures 4.6 and 4.7 illustrate the internal energy and bremsstrahlung luminosity, respectively. The behavior observed in the latter case is qualitatively similar to results shown in [98], i.e., an initial drop followed by a recovery in luminosity. Our simulations, which extend farther, indicate that this behavior continues quasi-periodically. Notice, however, that the disk geometry considered in [98] is different from ours and the bremsstrahlung computed includes the inner portion of the disk while we do so for the complete disk. Last, the small drift observed in figure 4.6 is consistent with a linear accumulation of numerical error. A similar linear drift is observed in simulations of an unperturbed disk. This growth however is small –within 5%– over the length of the simulations considered ($\simeq 6P_{\mathrm{m}}$) and significantly smaller than the effects induced by the perturbations due to the recoiling black hole.

4.4.3 Asymmetric Cases: Kicks with a Component Orthogonal to the Disk's Angular Momentum

Next we concentrate on the oblique recoil case. For concreteness we adopt recoil velocity values $v_{\mathrm{kick}} = 300$, 1000 and 3000 km/s (we also consider 9000 km/s to verify the appearance of the main feature and check the empirical law presented below). We begin by examining the case where the kick direction is on the orbital plane (i.e., orthogonal to the angular momentum of the disk). The simulations for the different cases proceed along qualitatively similar phases, which
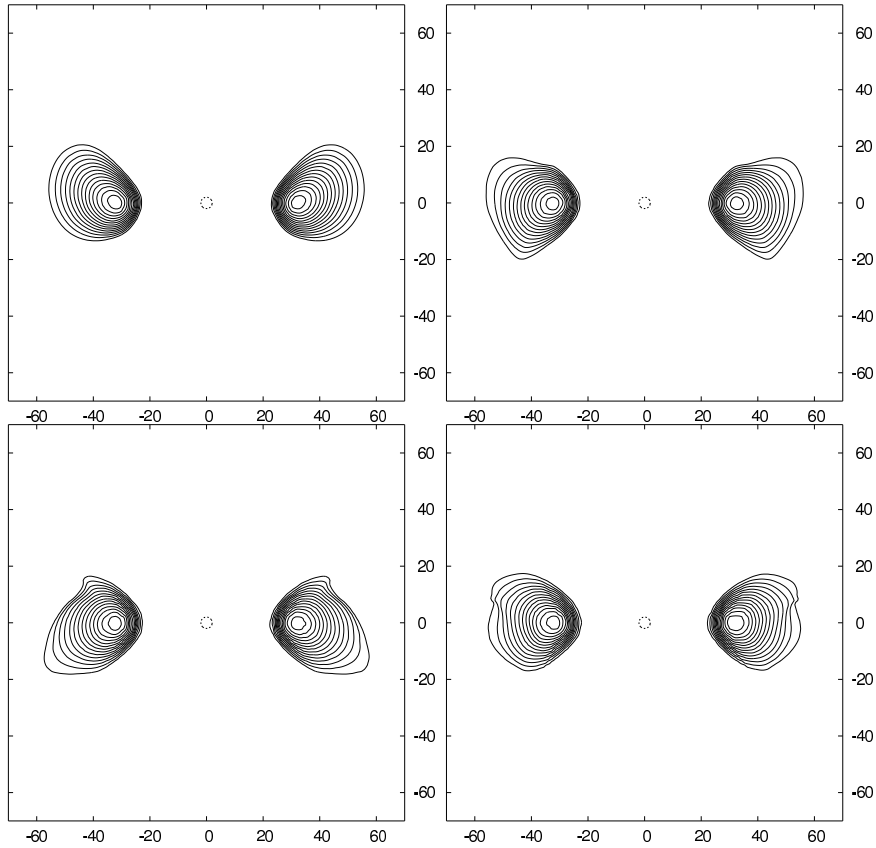
Figure 4.5: Density at plane $y = 0$ in the case of a disk kicked with a velocity 3000 km/s in the positive z-direction. The panels show snaps from $t/M = 500$ (top left) to 2000 (bottom right) at $\Delta t/M = 500$ intervals.

are illustrated for the case of v_{kick}=3000 km/s in figure 4.8, where we show the density, ρ, at different stages during the evolution. To better illustrate the formation of shocks, we also show, in figure 4.9, the norm of the pressure gradient, $|\nabla P|$. The disk's kick is applied in the positive x-axis direction (to the right in the figures.) The asymmetry introduced by the kick's direction induces an accumulation of gas at one side of the disk, while causing a significant decrease on the opposite side. As time progresses, shocks develop and a complex dynamic arises, at late times $\simeq 6000M$, an accretion phase is clearly noticeable for $v_{\text{kick}} >$1000 km/s (see figure 4.10).

To analyze the impact of the disk dynamics and possible observable features, we compute the internal energy (figure 4.11) and bremsstrahlung luminosity (figure 4.12) for v_{kick}=300, 1000, and 3000 km/s. An initial relatively small bump is observed, which takes place at a time given by half the orbital period of the maximum density region which is consistent with the epicyclic picture. From there on, a complex behavior is observed, though notably, independently of the magnitude of the kick, the same qualitative features are observed. Generally, we see that both the internal energy and the bremsstrahlung luminosity dip and rebound but the internal energy ends up higher, while the bremsstrahlung luminosity finishes lower. This can be understood as follows: the kick energy is dissipated in shocks, increasing the temperature and the pressure but the subsequent expansion reduces the density below the initial values. Because the bremsstrahlung emissivity is $\propto \rho^2 T^{1/2}$, the net effect is a reduction in emissivity despite the increase in pressure. The relative changes in both internal energy and bremsstrahlung luminosity
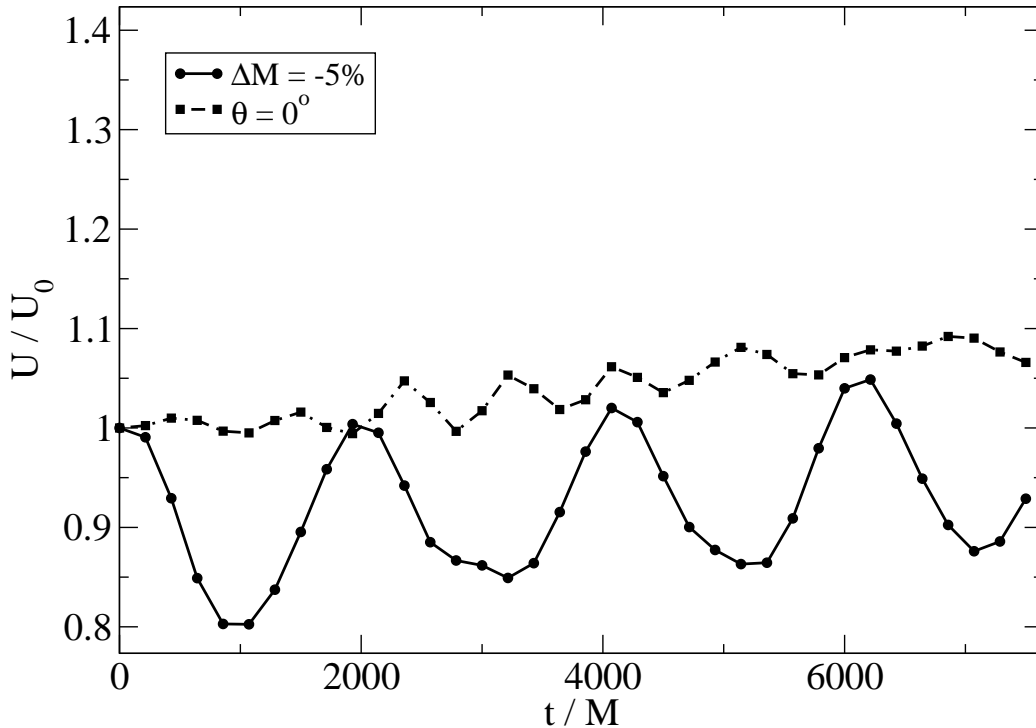
Figure 4.6: Total internal (normalized) energy of the disk. The continuous line corresponds to a black hole mass loss of 5% and no kick, while the dashed line corresponds to a kick with velocity $v_k = 3000$ km/s along the axis of rotation (and no black hole mass loss). The vertical scale and range was chosen to coincide with those in the other energy plots shown in this chapter for easy comparison.

are relatively modest, at a level of $\sim 20 - 40\%$ and occur on characteristic timescales on the order of $1000M = 5000M_6$ s, where M_6 is the mass of the black hole in $10^6 M_\odot$.

Second, we examine the dependence on kicks at different angles. Since the main qualitative features of all kick cases considered are similar, we concentrate in the case v_{kick}=3000 km/s as this is the one that displays the overall behavior within the shortest computational time. We compute the internal energy and bremsstrahlung luminosity for kicks at $\theta = 0, 30, 60$, and $90°$, where the angle θ is measured with respect to the axis of rotation. Figure 4.13 shows the density at plane $z = 0$ in the case of a kick at $30°$. Figures 4.14 and 4.15 illustrate the (normalized) internal energy and bremsstrahlung luminosity vs time for the different angles considered. Recall that no significant shocks form when the kick is along the axis of the disk. When the kick has a component along the disk's plane, however, the qualitative features observed in the internal energy are similar for all cases. We note that the evolution observed for a given $v_\perp \equiv v_k \sin\theta$ (with $v_k = 3000$ km/s) is nicely bracketed by evolutions with pure orbital plane kicks above and below $v_\perp$. Thus, $v_\perp$ is the most important parameter determining the behavior of the kicked disk, apart from the small oscillations also present when the kick is parallel to the axis of rotation, and the likely small differences in the shape of the initial shock.

Another feature common to all the internal energy results (See figures 4.11 and 4.14) is a rapid swing from a dip to a bump, followed by an oscillating growth at a moderate pace. While the magnitude of the upward swing of the internal energy does not depend strongly on $v_\perp$, the time at which it occurs does. The delay we observe decreases as $v_\perp$ is increased. If this delay were due to the time taken by a perturbation traveling at $v_\perp$ to cross some fixed distance, one
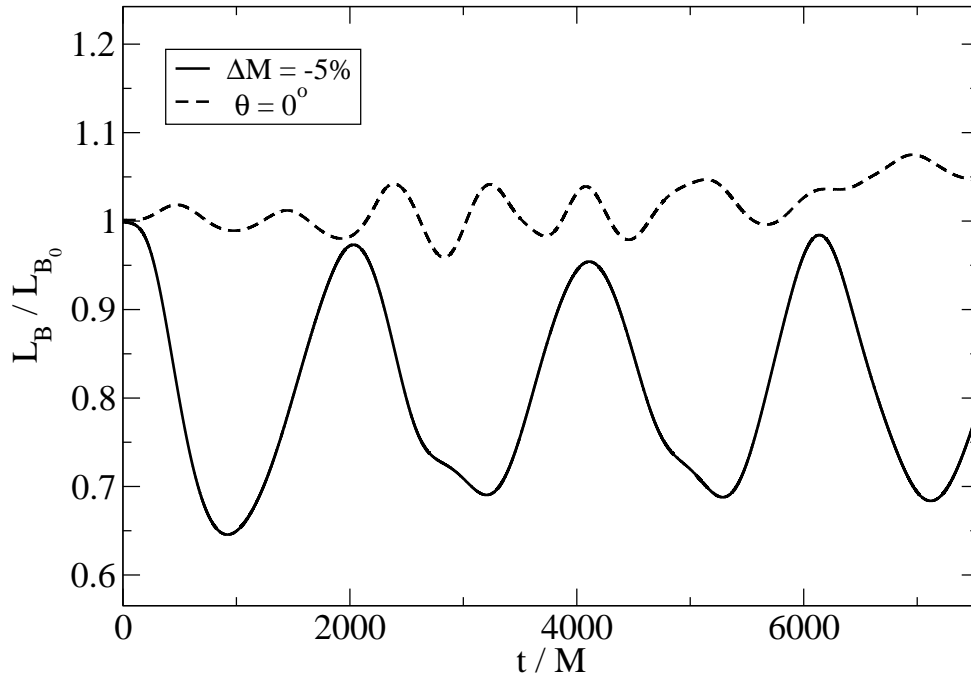
Figure 4.7: Bremsstrahlung luminosity (normalized) of the disk. The continuous line corresponds to a black hole mass loss of 5% and no kick, while the dashed line corresponds to a kick with velocity $v_{\mathrm{k}} = 3000$ km/s along the axis of rotation (and no black hole mass loss).

would expect a dependence $\propto v_\perp^{-1}$. Instead, we observe a logarithmic decrease. Defining the delay as the time after the initial kick at which the internal energy swings upward through the initial value, we find the following empirical dependence:

$$\frac{t_{\mathrm{swing}}}{M} = 5200 - 912 \ln \left(\frac{v_\perp}{300 \text{ km/s}} \right) \tag{4.41}$$

Note that this formula applied naïvely "predicts" an infinite delay for a kick along the axis of rotation.

It is known that constant specific angular momentum tori are prone to a non-axisymmetric instability [117, 118]. This instability has been studied numerically in the pseudo-Newtonian approximation [119] and in GRMHD [120]. The final outcome depends, in particular, on the aspect ratio of the torus, the nature and strength of any large-scale magnetic fields present and the presence of accretion [121].

Therefore, the perpendicular component of the kick is likely to excite at some level the $m = 1$ non-axisymmetric mode, which is expected to grow at a rate $\omega \approx 0.2\Omega_{\mathrm{m}}$, where $\Omega_{\mathrm{m}} = 2\pi/P_{\mathrm{m}}$ is the Keplerian angular frequency at the pressure maximum. If one assumes that the initial pressure perturbation is $\delta P_0 \propto v_\perp^2$, which is reasonable for shocks and on dimensional grounds, and one sets $\delta P = \delta P_0 \exp(\omega t)$, then the time required for the perturbation to attain a given fiducial level would follow an equation of the form (4.41), with $t = t_{\mathrm{ref}} - (2/\omega) \ln (v_\perp/v_{\mathrm{ref}})$, where t_{ref} and v_{ref} are some arbitrary reference values.

This seems to suggest that the behavior observed in our simulations is produced by the instability. However, for the particular parameters used in our simulations, we have $P_{\mathrm{m}} = 1220M$, and $\Omega_{\mathrm{m}} = 0.00515$, and analyzing the results obtained indicates that $\omega = 0.43\Omega_{\mathrm{m}}$, which is significantly higher than the expected value.
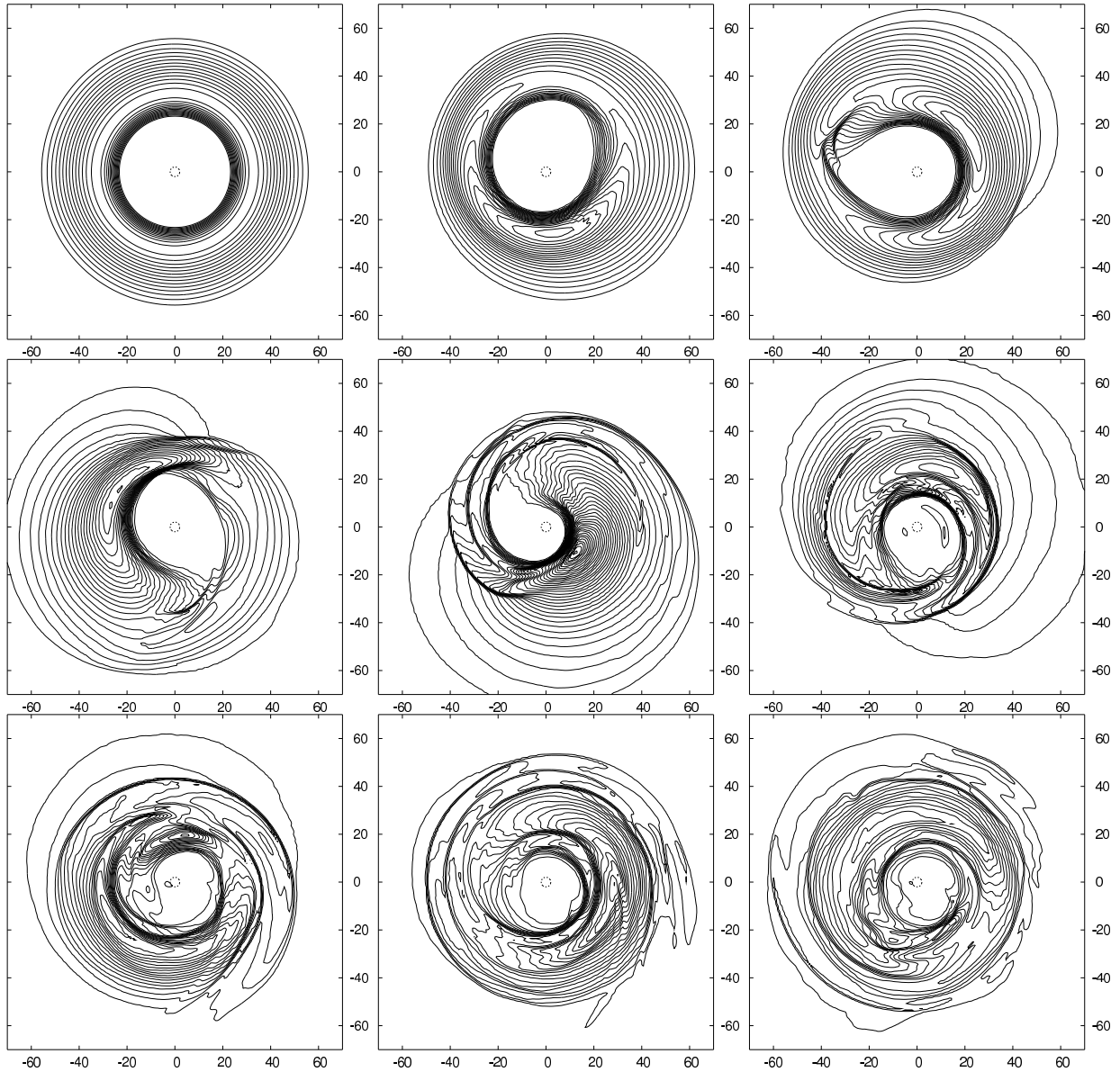
Figure 4.8: Density ρ at plane $z = 0$ in the case of a disk kicked with a velocity 3000 km/s in the positive x-direction, i.e., to the right of this page (which corresponds to the black hole being kicked to the left). The panels show snaps from $t/M = 0$ (top left) to 4000 (bottom right) at $\Delta t/M = 500$ intervals.

Thus, we suggest that the swing we see in both the internal energy and bremsstrahlung plots in all cases where there is a non-zero $v_\perp$ is not due to this instability, but a common transient response to the kick that may be observable in principle. We also note that a similar swing in the bremsstrahlung luminosity was observed in the (axisymmetry preserving) simulations by O'Neill et al [98] using thin disks, which are not prone to this type of instability.

The subsequent growth (see, for example, the blue curve of figure 4.11 for $t/M > 4200$) may be due to the growth of the instability and/or the rise to the expected level of dissipation of the input kinetic energy. However, we have not run our simulations for a longer time in order to study these possibilities. Moreover, our simulations display an accretion phase at late times (at least those cases with the highest kicks) and so this possibilities can not be further explored.
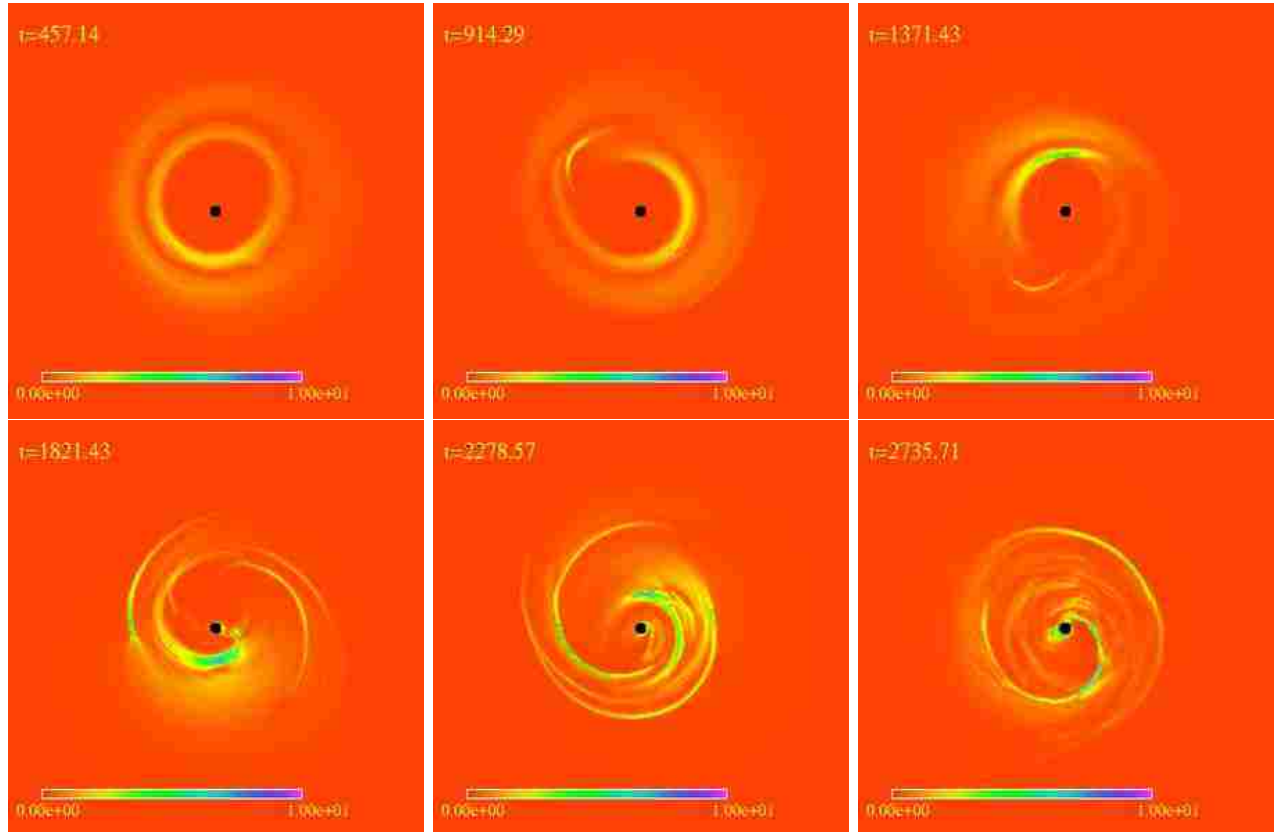
Figure 4.9: To illustrate the formation of shocks we show here $|\vec{\nabla}P|$ at $z = 0$ in the case of a kick velocity of 3000 km/s in the positive x-direction. The black square at the center represents the excised region, contained entirely inside the event horizon.
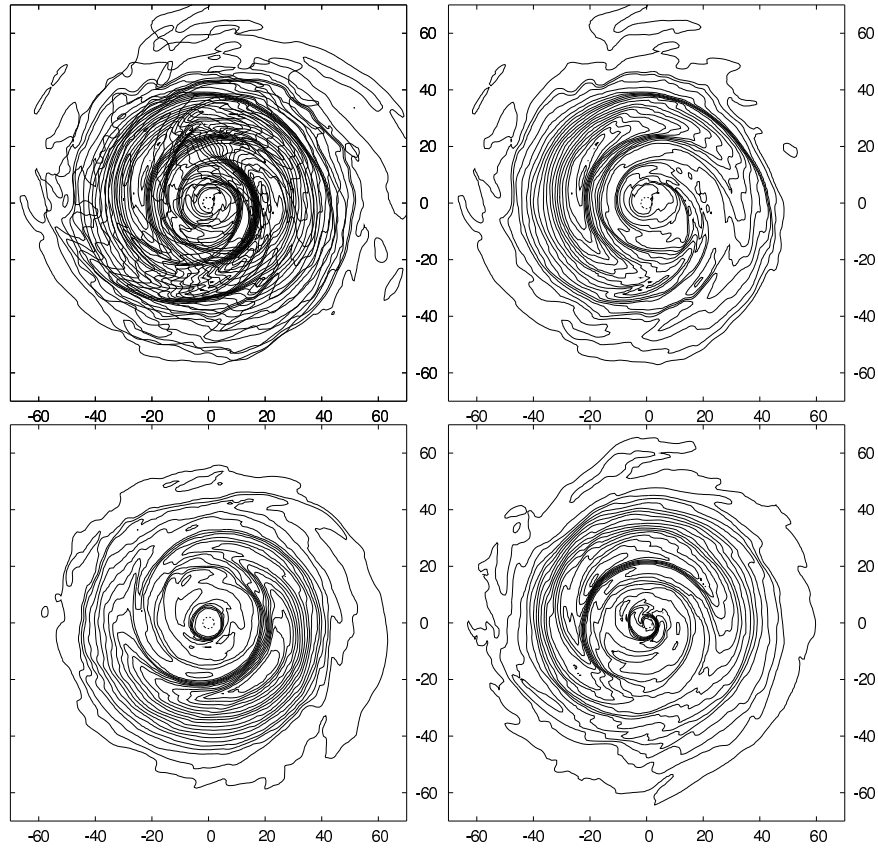
Figure 4.10: Later stages of the simulation shown in figure 4.8, in which the gas begins to accrete into the black hole. The panels show snaps from $t/M = 6000$ (top left) to 7500 (bottom right) at $\Delta t/M = 500$ intervals. Notice that at $t/M = 7000$ the ISCO is clearly noticeable.
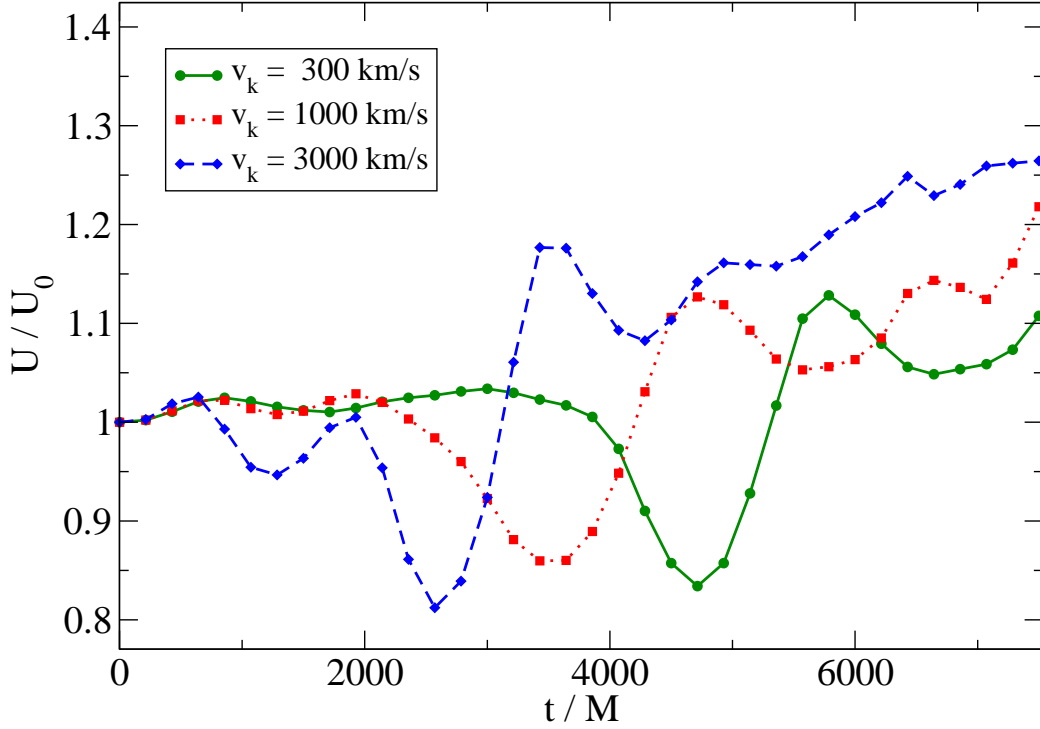
Figure 4.11: Normalized internal energy for cases with a kick perpendicular to axis of rotation ($\theta = 90°$). Similar features are seen in all three cases, with only a time offset difference.
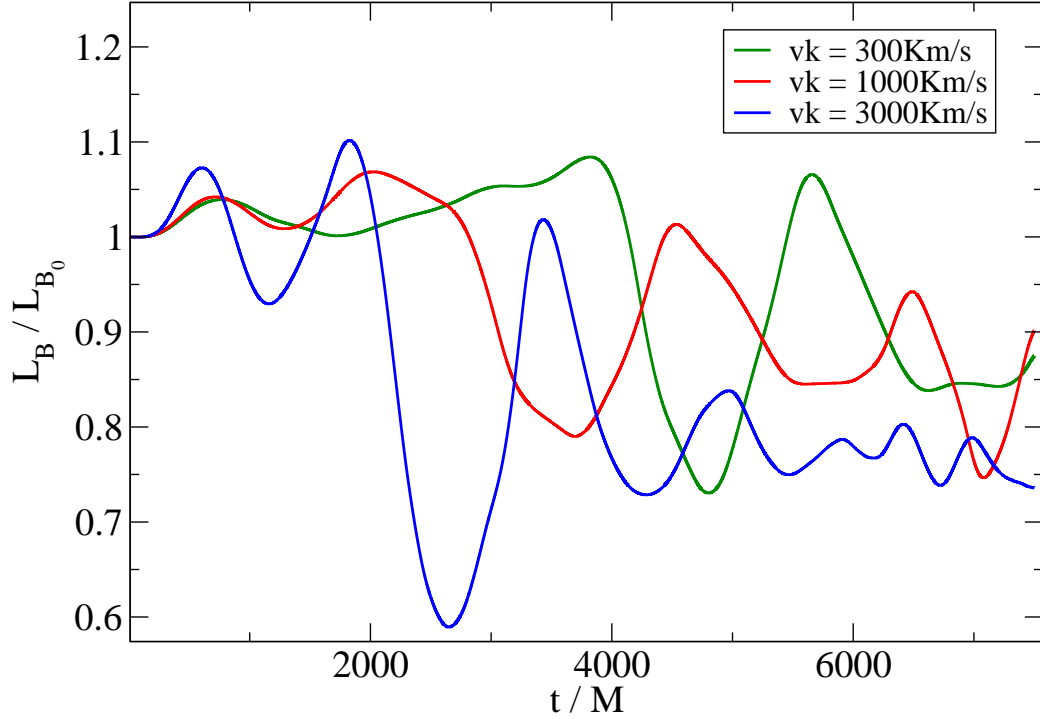
Figure 4.12: Normalized bremsstrahlung luminosity for cases with a kick perpendicular to axis of rotation ($\theta = 90°$). Although less obvious than in the internal energy plot, we can also see common features (besides a time offset), mainly during the time frame of greater fluctuation in each case.
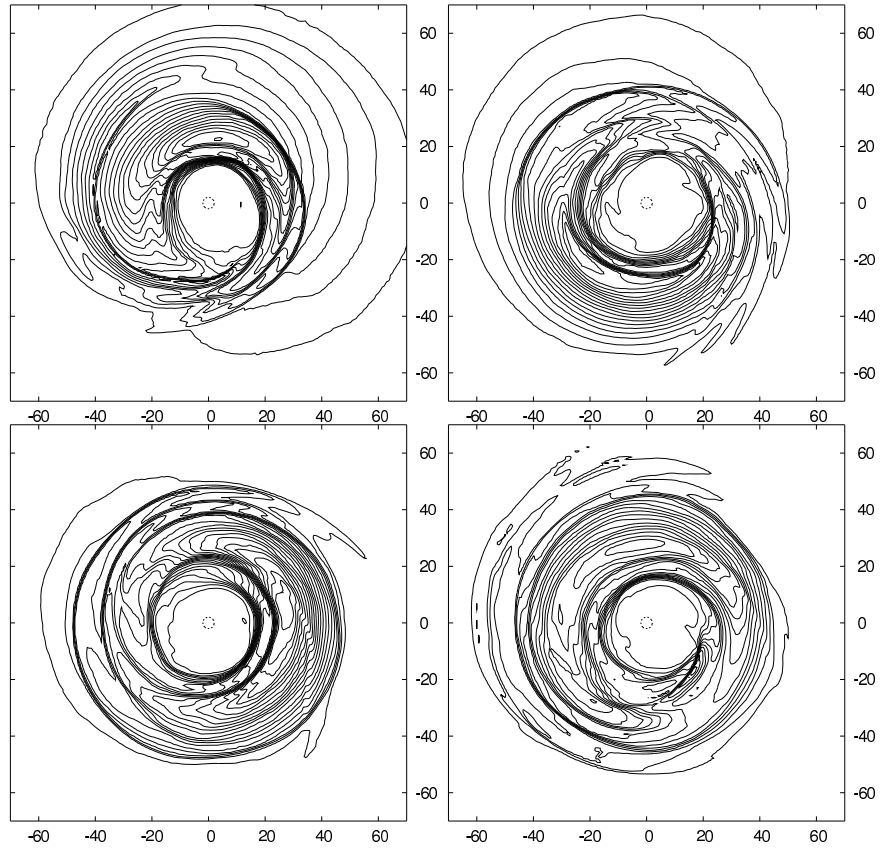
Figure 4.13: Density ρ at plane $z = 0$ in the case of a disk kicked with a velocity 3000 km/s at $\theta = 30°$. The panels show snaps from $t/M = 2500$ (top left) to 4000 (bottom right) at $\Delta t/M = 500$ intervals.
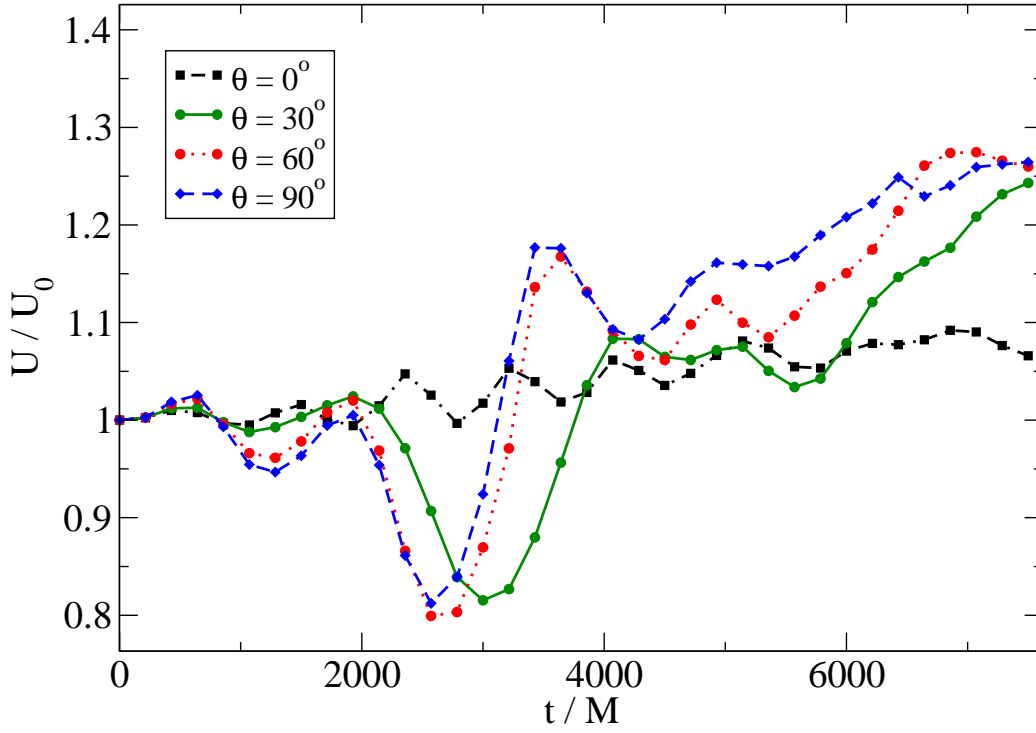
Figure 4.14: Internal energy. Kicks at varying inclinations θ with respect to the axis of rotation. All cases with $v_{\mathrm{kick}} = 3000$ km/s. For the cases with a perpendicular kick component we can see the same main features as in figure 4.11.
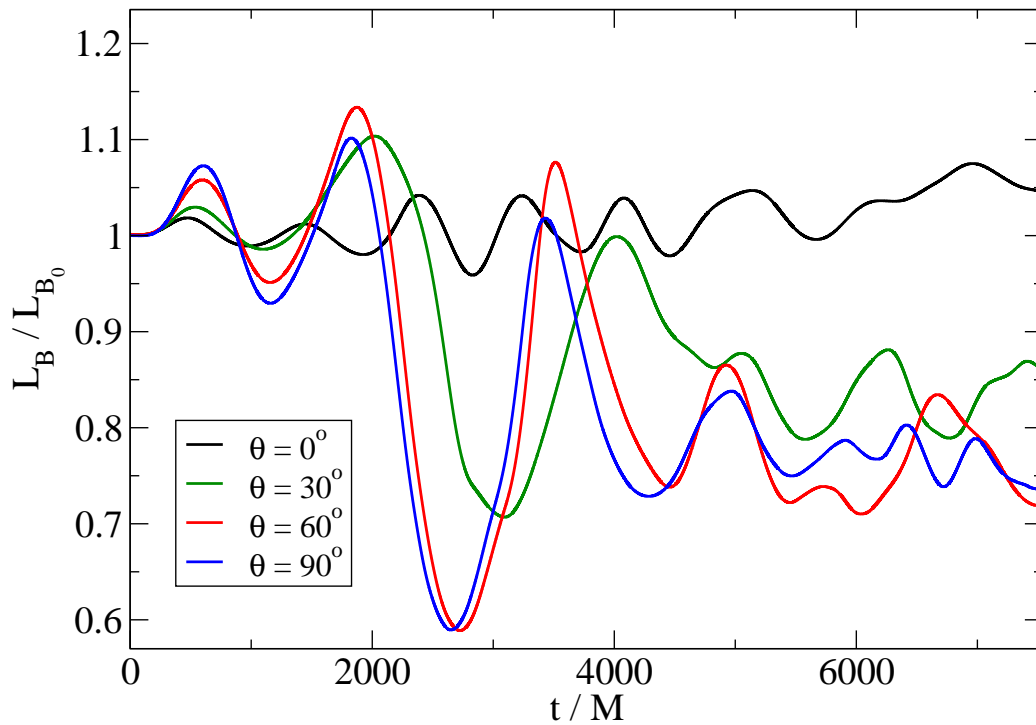
Figure 4.15: Bremsstrahlung luminosity for kicks at varying inclinations θ with respect to the axis of rotation. All cases with $v_{\mathrm{kick}} = 3000$ km/s.

4.4.4 Dependence on Black Hole Spin

Finally, we investigate possible differences between cases with different black hole spins. To that end, we perform a simulation with spin $a/M = 0.9$ in addition to the value $a/M = 0.5$ used in the rest of the simulations. For this test we chose the "strongest" kick setting, i.e., that with kick velocity of 3000 km/s perpendicular to the disk's axis, since all the other cases considered in this work would show less discrepancy.

Notice that although all other parameters (besides spin) coincide in these simulations, the stationary disk solutions used to construct the initial data are slightly different since they depend on a. Still, we see no significant differences, as is illustrated in figure 4.16, where we show a comparison between the maxima of density, normalized by dividing by its value at $t = 0$ (which is slightly different in each case.)
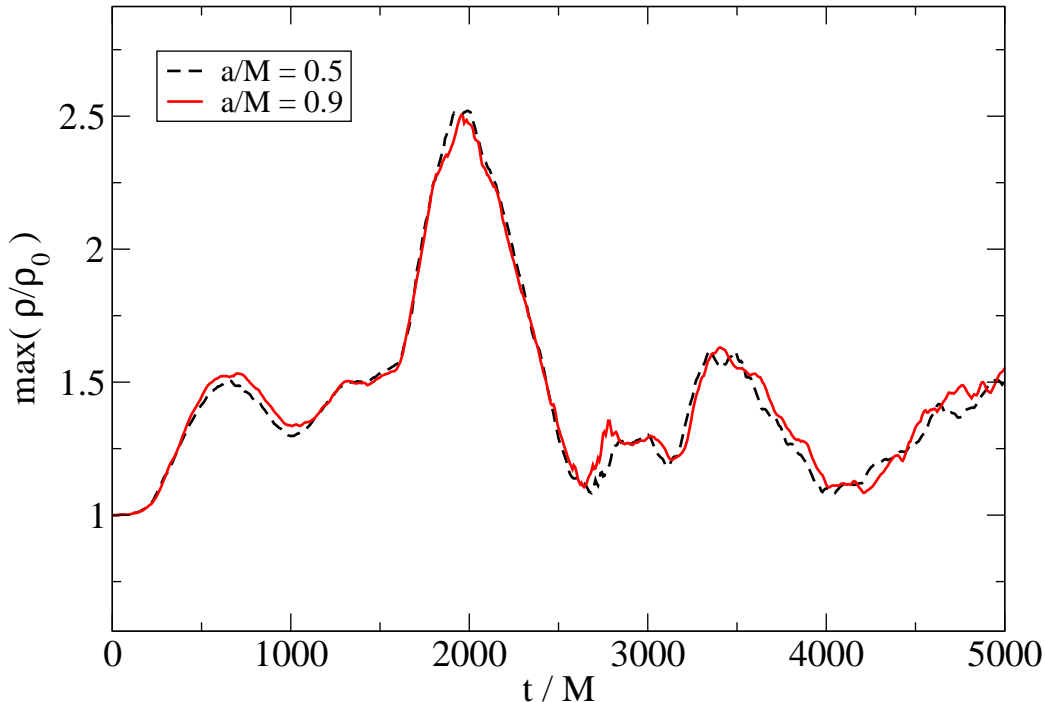
Figure 4.16: Comparison of the maximum of density for black hole spins $a/M = 0.5$ (dashed line) and 0.9 (continuous line) for a kick of 3000 km/s perpendicular to the disk's axis.

4.4.5 Ray Tracing: Preliminary Results

At the moment of writing this dissertation, work is in progress [122] to incorporate a more refined radiation model. In that work, the radiation transfer equation is integrated along geodesics to study the photon transport from the source to observers located at different orientations. The model being used at the moment incorporates Bremsstrahlung emission, together with Kramer's opacity law adjusted to incorporate black body effects in the optically thick regions. The calculations in [122] are done as post-processing using data from the simulations described previously in this chapter.

As a preliminary result, we show in figure 4.17 a comparison between the (normalized) bremsstrahlung luminosities emitted at a frequency of 10^{18} Hz in three different orientations, and the total bremsstrahlung luminosity (integrated over all frequencies source points) calculated

using equation 4.35, showing qualitatively good agreement with the results shown previously. Similar results are seen for frequencies larger than 10^{13} Hz (including the whole X-ray spectrum), where the disk is mostly optically thin. In that regime, the main features observed, coincide with those shown earlier, in which we base our conclusions.
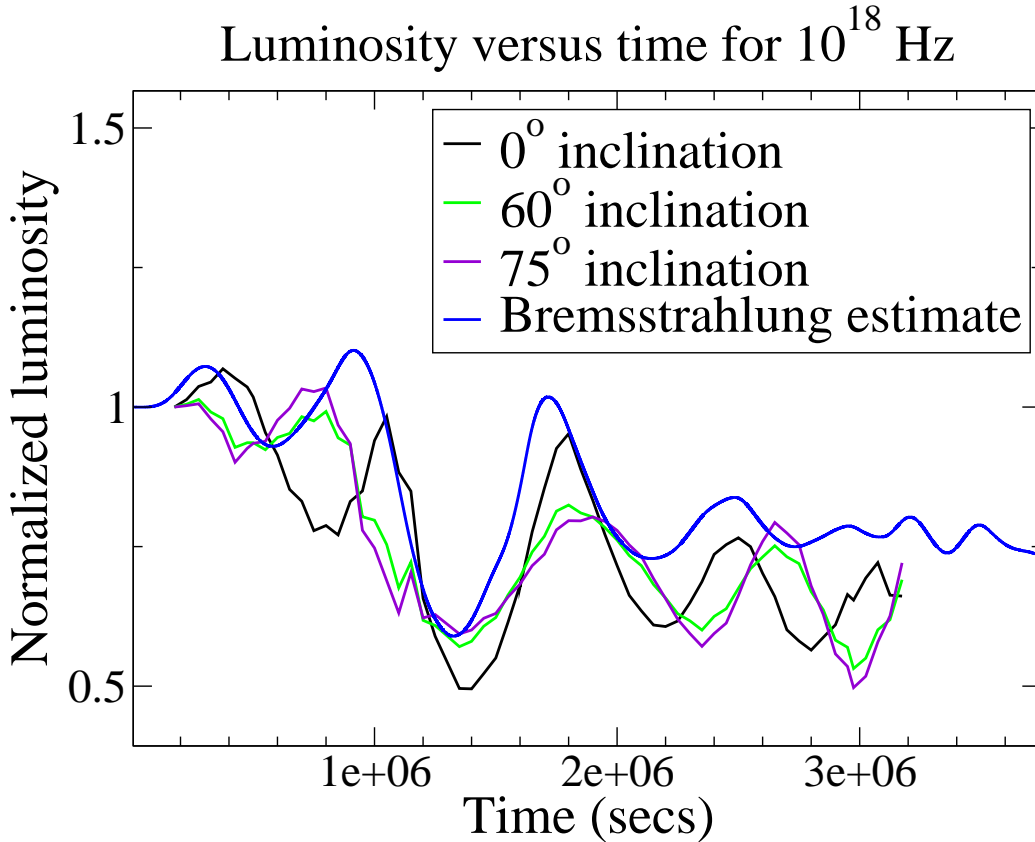
Figure 4.17: Comparison with preliminary results from [122]. The blue curve corresponds to that shown in figure 4.12 (also in blue).

4.5 Conclusions

In this chapter we have studied the possibility that binary black hole mergers, within a circumbinary disk, give rise to scenarios likely to emit electromagnetic radiation. We have studied both the impact of mass loss in the system and recoil velocities. While both induce deformations of the disk, it is the case of a recoiling black hole, when the recoil's direction has a component along the disk's plane, the one that appears as the most promising option to generate an observable electromagnetic signature. This is so not just because the effect is larger, but also the variability induced is significantly more pronounced than that observed in the case of mass loss or kick along the disk's angular momentum. Furthermore, we find that the magnitude of the kick is not very important (at least as long as it is less than the smallest orbital speed of the fluid.) While the kick magnitude impacts the time at which the strongest variation in internal energy or bremsstrahlung appears, the intensity and time scale of the variation and behavior afterwards is not. Since super-massive binary black hole mergers will generically give rise to recoils (simply by having a mass ratio different from unity) which in turn ensures a kick component orthogonal

to the final black hole spin, effects like those observed here indicate a possible common behavior for the majority of scenarios.

Our studies also indicate that the final black hole spin has no strong effect on the main features of the solution. However, when an accretion phase takes place, the location of the innermost stable circular orbit, which depends on the spin, will naturally play a key role.

Chapter 5
Final Comments

In this dissertation we have studied the interaction of matter sources with a black hole in different scenarios. In Chapter 2 we discussed the possibility to confine a scalar field to some region surrounding a black hole. We saw that this can be done systematically if the spacetime posseses some symmetries, thus taking advantage of those symmetries to construct a coordinate-dependent potential. We considered in particular an axially symmetric spacetime and, in more detail, a spherically symmetric one. In the latter case we showed, by solving numerically the Einstein equations coupled to a scalar field, that a spherical shell can indeed be confined to the surrounding of the black hole. Varying the characteristics of the initial conditions set for the scalar field and potential, part of the scalar field can be allowed to accreted into the black hole during an initial transient. The amount of energy that falls into the black hole can be controlled varying the mentioned parameters.

Then, in chapter 3, we described a method to estimate the characteristic frequency of the end of the inspiral phase of a merging binary. The method was used to provide a better estimate (as compared to previous work) of the range of BH-NS binaries for which the disruption is more plausible to be measured. The estimated frequencies also provide good cut off values for the post-Newtonian templates used in data analysis to model the inspiral part of the waveform, resulting in an increased signal to noise ratio as compared to more simplistic approaches.

Finally, in chapter 4, we studied the effects of a black hole binary merger on a circumbinary disk, that would result in electromagnetic signatures. Two effects were studied separately, namely, the central mass reduction caused by the energy lost in the emitted gravitational waves, and the final black hole recoil, caused by anisotropic gravitational radiation, that may carry away linear momentum. The most interesting result is seen when the recoil velocity has a component along the disk's plane, in which case both the internal energy and bremsstrahlung luminosity show a characteristic pattern, qualitatively independent of the recoil velocity, except for a time offset that depends on the perpendicular component of the kick.

In our analysis we use simple models, in which we compute internal energy variations, as well as total (integrated over all frequencies) bremsstrahlung luminosity in the optically thin approximation. Yet it seems reasonable to expect that the signatures described will be somehow reflected in observable electromagnetic signals. However, more refined radiation models may be needed to further support our results in less restrictive approximations. Work is underway to include richer models, of which preliminary results (presented in section 4.4.5) so far support our previous analysis in a wide range of emission frequencies. Besides continuing improving and adding other processes to our radiation models, we plan to consider other disk geometries, as well as including a magnetic field. Work is also underway to study pre-merger effects (not considered in this work) for which fully dynamical simulations of a binary black hole are run.

Bibliography

[1] http://www.ligo.caltech.edu/.

[2] Zoltan Haiman, Bence Kocsis, Kristen Menou, Zoltan Lippai, and Zsolt Frei. Identifying Decaying Supermassive Black Hole Binaries from their Variable Electromagnetic Emission. 2008.

[3] http://www.virgo.infn.it/.

[4] Cedric Deffayet and Kristen Menou. Probing gravity with spacetime sirens. *The Astrophysical Journal Letters*, 668(2):L143–L146, 2007.

[5] Milos Milosavljevic and E. S. Phinney. The Afterglow of Massive Black Hole Coalescence. *Astrophys. J.*, 622:L93–L96, 2005.

[6] R. M. Wald. General relativity. *Chicago: The University of Chicago Press*, 1984.

[7] Richard H. Price and Viqar Husain. Model for the completeness of quasinormal modes of relativistic stellar oscillations. *Phys. Rev. Lett.*, 68(13):1973–1976, Mar 1992.

[8] J. M. Weisberg and J. H. Taylor. The Relativistic Binary Pulsar B1913+16: Thirty Years of Observations and Analysis. In F. A. Rasio and I. H. Stairs, editors, *Binary Radio Pulsars*, volume 328 of *Astronomical Society of the Pacific Conference Series*, page 25, July 2005.

[9] M. Kramer, I. H. Stairs, R. N. Manchester, M. A. McLaughlin, A. G. Lyne, R. D. Ferdman, M. Burgay, D. R. Lorimer, A. Possenti, N. D'Amico, J. M. Sarkissian, G. B. Hobbs, J. E. Reynolds, P. C. C. Freire, and F. Camilo. Tests of General Relativity from Timing the Double Pulsar. *Science*, 314:97–102, October 2006.

[10] Bernard F. Schutz. A first course in general relativity. *Cambridge University Press*, 2nd edition (2009).

[11] A. Stroeer and A. Vecchio. The LISA verification binaries. *Classical and Quantum Gravity*, 23:809–+, October 2006.

[12] http://geo600.aei.mpg.de/.

[13] http://lisa.nasa.gov/.

[14] M. Megevand, I. Olabarrieta, and L. Lehner. Scalar field confinement as a model for accreting systems. *Classical and Quantum Gravity*, 24:3235–3258, July 2007.

[15] C W Misner, K S Thorne, and J A Wheeler. Gravitation. *New York: W H Freeman and Company*, 1973.

[16] M. A. Scheel, S. L. Shapiro, and S. A. Teukolsky. Scalar gravitation: A laboratory for numerical relativity. III. Axisymmetry. *Phys. Rev. D*, 49:1894–1905, February 1994.

[17] David J. Kaup. Klein-gordon geon. *Phys. Rev.*, 172(5):1331–1342, Aug 1968.

[18] Remo Rufini and Silvano Bonazzola. Systems of self-gravitating particles in general relativity and the concept of an equation of state. *Phys. Rev.*, 187(5):1767–1783, Nov 1969.

[19] Edward Seidel and Wai-Mo Suen. Oscillating soliton stars. *Phys. Rev. Lett.*, 66(13):1659–1662, Apr 1991.

[20] C. Palenzuela, L. Lehner, and S.L. Liebling. Orbital dynamics of binary boson star systems. arXiv:gr-qc/0706.2435, 2007.

[21] A. R. Liddle. An Introduction to Cosmological Inflation. In A. Masiero, G. Senjanovic, and A. Smirnov, editors, *High Energy Physics and Cosmology, 1998 Summer School*, page 260, 1999.

[22] J. E. Lidsey, A. R. Liddle, E. W. Kolb, E. J. Copeland, T. Barreiro, and M. Abney. Reconstructing the inflaton potential-an overview. *Reviews of Modern Physics*, 69:373–410, April 1997.

[23] Matthew W. Choptuik. Universality and scaling in gravitational collapse of a massless scalar field. *Phys. Rev. Lett.*, 70(1):9, Jan 1993.

[24] C. Gundlach. Critical Phenomena in Gravitational Collapse. *Living Reviews in Relativity*, 2:4, December 1999.

[25] Matthew W. Choptuik, Eric W. Hirschmann, Steven L. Liebling, and Frans Pretorius. Critical collapse of a complex scalar field with angular momentum. *Phys. Rev. Lett.*, 93(13):131101, Sep 2004.

[26] I. (. Olabarrieta, J. F. Ventrella, M. W. Choptuik, and W. G. Unruh. Critical behavior in the gravitational collapse of a scalar field with angular momentum in spherical symmetry. *Phys. Rev. D*, 76(12):124014, December 2007.

[27] Arlen Anderson and James W. York. Fixing einstein's equations. *Phys. Rev. Lett.*, 82(22):4384–4387, May 1999.

[28] Lawrence E. Kidder, Mark A. Scheel, Saul A. Teukolsky, Eric D. Carlson, and Gregory B. Cook. Black hole evolution by spectral methods. *Phys. Rev. D*, 62(8):084032, Sep 2000.

[29] Gioel Calabrese, Luis Lehner, and Manuel Tiglio. Constraint-preserving boundary conditions in numerical relativity. *Phys. Rev. D*, 65(10):104031, May 2002.

[30] W Press, B Flannery, Teukolsky S, and W Vetterling. Numerical recipes in fortran. *Cambridge University Press*, 1992.

[31] A C Hindmarsh. http://www.llnl.gov/casc/odepack/, Lawrence Livermore National Laboratory.

[32] H O Kreiss and G Scherer. in mathematical aspects of finite elements in partial differential equations, edited by c d boor. *New York: Academica Press*, 1974.

[33] H O Kreiss and G Scherer. Tech. rep. *Dept. of Scientific Computing, Uppsala University*, 1977.

[34] B Strand. Summation by parts for finite difference approximations for d/dx. *Journal of Computational Physics*, 110:47, 1994.

[35] G Calabrese, L Lehner, D Neilsen, J Pullin, Reula O, O Sarbach, and M Tiglio. Novel finite-differencing techniques for numerical relativity: application to black hole excision. *Class. Quant. Grav.*, 20:L245, 2003.

[36] G Calabrese, L Lehner, O Reula, O Sarbach, and M Tiglio. Summation by parts and dissipation for domains with excised regions. *Class. Quant. Grav.*, 21:5735, 2004.

[37] D Levy and E Tadmor. *SIAM Journal on Num. Anal.*, 40:40, 1998.

[38] H Kreiss and J Oliger. Methods for the approximate solution of time independent problems. *Geneva: GARP Publication Series*, 1973.

[39] B Gustafsson, H Kreiss, and J Oliger. Time dependent problems and difference methods. *John Wiley and Sons*, 1995.

[40] Reula O Lehner L, Neilsen D and Tiglio M. The discrete energy method in numerical relativity: Towards long-term stability. *Class. Quant. Grav.*, 21:5819, 2004.

[41] P Olsson. *Math. Comp.*, 64:1035, 1995.

[42] P Olsson. *Math. Comp.*, 64:S23, 1995.

[43] P Olsson. *Math. Comp.*, 64:1473, 1995.

[44] J W Thomas. Numerical partial differential equations: Finite difference methods. *New York: Springer-Verlag*, 1995.

[45] S Chandrasekhar. The mathematical theory of black holes. *New York: Oxford University Press*, 1992.

[46] C. Hanna, M. Megevand, E. Ochsner, and C. Palenzuela. A method for estimating time frequency characteristics of compact binary mergers to improve searches for inspiral, merger and ring-down phases separately. *Classical and Quantum Gravity*, 26(1):015009, January 2009.

[47] M. Vallisneri. Prospects for Gravitational-Wave Observations of Neutron-Star Tidal Disruption in Neutron-Star-Black-Hole Binaries. *Physical Review Letters*, 84:3519–3522, April 2000.

[48] B. J. Owen. Search templates for gravitational waves from inspiraling binaries: Choice of template spacing. *Phys. Rev. D*, 53:6749–6761, June 1996.

[49] The LIGO Scientific Collaboration. Analysis of LIGO data for gravitational waves from binary neutron stars. *Phys. Rev. D*, 69(12):122001, June 2004.

[50] The LIGO Scientific Collaboration. Search for gravitational waves from galactic and extra-galactic binary neutron stars. *Phys. Rev. D*, 72(8):082001, October 2005.

[51] The LIGO Scientific Collaboration. Search for gravitational waves from binary black hole inspirals in LIGO data. *Phys. Rev. D*, 73(6):062001, March 2006.

[52] The LIGO Scientific Collaboration. Search for gravitational waves from binary inspirals in S3 and S4 LIGO data. *Phys. Rev. D*, 77(6):062002, March 2008.

[53] A. Buonanno, G. B. Cook, and F. Pretorius. Inspiral, merger, and ring-down of equal-mass black-hole binaries. *Phys. Rev. D*, 75(12):124018, June 2007.

[54] E. Berti, V. Cardoso, J. A. Gonzalez, U. Sperhake, M. Hannam, S. Husa, and B. Brügmann. Inspiral, merger, and ringdown of unequal mass black hole binaries: A multipolar analysis. *Phys. Rev. D*, 76(6):064034, September 2007.

[55] B. Vaishnav, I. Hinder, F. Herrmann, and D. Shoemaker. Matched filtering of numerical relativity templates of spinning binary black holes. *Phys. Rev. D*, 76(8):084020, October 2007.

[56] J. G. Baker, S. T. McWilliams, J. R. van Meter, J. Centrella, D.-I. Choi, B. J. Kelly, and M. Koppitz. Binary black hole late inspiral: Simulations for gravitational wave observations. *Phys. Rev. D*, 75(12):124024, June 2007.

[57] B. Allen, W. G. Anderson, P. R. Brady, D. A. Brown, and J. D. E. Creighton. FIND-CHIRP: an algorithm for detection of gravitational waves from inspiraling compact binaries. *ArXiv General Relativity and Quantum Cosmology e-prints*, September 2005.

[58] A. Buonanno, L. E. Kidder, and L. Lehner. Estimating the final spin of a binary black hole coalescence. *Phys. Rev. D*, 77(2):026004, January 2008.

[59] J. M. Bardeen, W. H. Press, and S. A. Teukolsky. Rotating Black Holes: Locally Non-rotating Frames, Energy Extraction, and Scalar Synchrotron Radiation. *Astrophys. J.*, 178:347–370, December 1972.

[60] M. Saijo and T. Nakamura. Possible direct method to determine the radius of a star from the spectrum of gravitational wave signals. II. Spectra for various cases. *Phys. Rev. D*, 63(6):064004, March 2001.

[61] L. Lindblom. Determining the nuclear equation of state from neutron-star masses and radii. *Astrophys. J.*, 398:569–573, October 1992.

[62] T. Harada. Reconstructing the equation of state for cold nuclear matter from the relationship of any two properties of neutron stars. *Phys Rev C*, 64(4):048801, October 2001.

[63] M. Shibata. Relativistic Roche-Riemann Problems around a Black Hole. *Progress of Theoretical Physics*, 96:917–932, November 1996.

[64] M. Shibata and K. Taniguchi. Merger of black hole and neutron star in general relativity: Tidal disruption, torus mass, and gravitational waves. *Phys. Rev. D*, 77(8):084015, April 2008.

[65] A. Buonanno and T. Damour. Effective one-body approach to general relativistic two-body dynamics. *Phys. Rev. D*, 59(8):084006, April 1999.

[66] Y. Pan, A. Buonanno, J. G. Baker, J. Centrella, B. J. Kelly, S. T. McWilliams, F. Pretorius, and J. R. van Meter. Data-analysis driven comparison of analytic and numerical coalescing binary waveforms: Nonspinning case. *Phys. Rev. D*, 77(2):024014, January 2008.

[67] M. Hannam, S. Husa, J. A. González, U. Sperhake, and B. Brügmann. Where post-Newtonian and numerical-relativity waveforms meet. *Phys. Rev. D*, 77(4):044020, February 2008.

[68] J. G. Baker, J. R. van Meter, S. T. McWilliams, J. Centrella, and B. J. Kelly. Consistency of Post-Newtonian Waveforms with Numerical Relativity. *Physical Review Letters*, 99(18):181101, November 2007.

[69] M. Boyle, D. A. Brown, L. E. Kidder, A. H. Mroué, H. P. Pfeiffer, M. A. Scheel, G. B. Cook, and S. A. Teukolsky. High-accuracy comparison of numerical relativity simulations with post-Newtonian expansions. *Phys. Rev. D*, 76(12):124038, December 2007.

[70] A. Gopakumar, M. Hannam, S. Husa, and B. Brügmann. Comparison between numerical relativity and a new class of post-Newtonian gravitational-wave phase evolutions: The nonspinning equal-mass case. *Phys. Rev. D*, 78(6):064026, September 2008.

[71] M. Hannam, S. Husa, B. Brügmann, and A. Gopakumar. Comparison between numerical-relativity and post-Newtonian waveforms from spinning binaries: The orbital hang-up case. *Phys. Rev. D*, 78(10):104007, November 2008.

[72] L. Blanchet. Gravitational Radiation from Post-Newtonian Sources and Inspiralling Compact Binaries. *Living Reviews in Relativity*, 9:4, June 2006.

[73] A. Buonanno, Y. Pan, J. G. Baker, J. Centrella, B. J. Kelly, S. T. McWilliams, and J. R. van Meter. Approaching faithful templates for nonspinning binary black holes using the effective-one-body approach. *Phys. Rev. D*, 76(10):104049, November 2007.

[74] T. Damour, B. R. Iyer, and B. S. Sathyaprakash. Comparison of search templates for gravitational waves from binary inspiral. *Phys. Rev. D*, 63(4):044023, February 2001.

[75] Y. Pan, A. Bounanno, J.G. Baker, J. Centrella, B.J. Kellly, S.T. McWilliams, F. Pretorius, and J.R van Meter. A data-analysis driven comparison of analytical and numerical coalescing binary waveforms: non-spinning case. 2007.

[76] M. Megevand, M. Anderson, J. Frank, E. W. Hirschmann, L. Lehner, S. L. Liebling, P. M. Motl, and D. Neilsen. Perturbed disks get shocked: Binary black hole merger effects on accretion disks. *Phys. Rev. D*, 80(2):024012, July 2009.

[77] Julien Sylvestre. Prospects for the detection of electromagnetic counterparts to gravitational wave events. *Astrophys. J.*, 591:1152–1156, 2003.

[78] Christopher W. Stubbs. Linking optical and infrared observations with gravitational wave sources through variability. *Class. Quant. Grav.*, 25:184033, 2008.

[79] Joshua S. Bloom et al. Astro2010 Decadal Survey Whitepaper: Coordinated Science in the Gravitational and Electromagnetic Skies. 2009.

[80] P. J. Armitage and P. Natarajan. Accretion during the Merger of Supermassive Black Holes. *Ap. J. Letters*, 567:L9–L12, March 2002.

[81] F. K. Liu, X.-B. Wu, and S. L. Cao. Double-double radio galaxies: remnants of merged supermassive binary black holes. *MNRAS*, 340:411–416, April 2003.

[82] Bence Kocsis and Abraham Loeb. Brightening of an Accretion Disk Due to Viscous Dissipation of Gravitational Waves During the Coalescence of Supermassive Black Holes. *Phys. Rev. Lett.*, 101:041101, 2008.

[83] J. D. Bekenstein. Gravitational-Radiation Recoil and Runaway Black Holes. *Astrophys. J.*, 183:657–664, July 1973.

[84] M. J. Fitchett. The influence of gravitational wave momentum losses on the centre of mass motion of a Newtonian binary system. *MNRAS*, 203:1049–1062, June 1983.

[85] J. G. Baker, W. D. Boggs, J. Centrella, B. J. Kelly, S. T. McWilliams, M. C. Miller, and J. R. van Meter. Modeling Kicks from the Merger of Nonprecessing Black Hole Binaries. *Astrophys. J.*, 668:1140–1144, October 2007.

[86] J. G. Baker, W. D. Boggs, J. Centrella, B. J. Kelly, S. T. McWilliams, M. C. Miller, and J. R. van Meter. Modeling Kicks from the Merger of Generic Black Hole Binaries. *Ap. J. Letters*, 682:L29–32, July 2008.

[87] M. Campanelli, C. Lousto, Y. Zlochower, and D. Merritt. Large Merger Recoils and Spin Flips from Generic Black Hole Binaries. *Ap. J. Letters*, 659:L5–L8, April 2007.

[88] M. Campanelli, C. O. Lousto, Y. Zlochower, and D. Merritt. Maximum Gravitational Recoil. *Physical Review Letters*, 98(23):231102, June 2007.

[89] J. A. González, U. Sperhake, B. Brügmann, M. Hannam, and S. Husa. Maximum Kick from Nonspinning Black-Hole Binary Inspiral. *Physical Review Letters*, 98(9):091101, March 2007.

[90] J. A. González, M. Hannam, U. Sperhake, B. Brügmann, and S. Husa. Supermassive Recoil Velocities for Binary Black-Hole Mergers with Antialigned Spins. *Physical Review Letters*, 98(23):231101, June 2007.

[91] F. Herrmann, I. Hinder, D. Shoemaker, and P. Laguna. Unequal mass binary black hole plunges and gravitational recoil. *Classical and Quantum Gravity*, 24:33, June 2007.

[92] F. Herrmann, I. Hinder, D. Shoemaker, P. Laguna, and R. A. Matzner. Gravitational Recoil from Spinning Binary Black Hole Mergers. *Astrophys. J.*, 661:430–436, May 2007.

[93] W. Tichy and P. Marronetti. Binary black hole mergers: Large kicks for generic spin orientations. *Phys. Rev. D*, 76(6):061502, September 2007.

[94] J. D. Schnittman and A. Buonanno. The Distribution of Recoil Velocities from Merging Black Holes. *Ap. J. Letters*, 662:L63–L66, June 2007.

[95] G. A. Shields and E. W. Bonning. Powerful Flares from Recoiling Black Holes in Quasars. *Astrophys. J.*, 682:758–766, August 2008.

[96] Z. Lippai, Z. Frei, and Z. Haiman. Prompt Shocks in the Gas Disk around a Recoiling Supermassive Black Hole Binary. *Ap. J. Letters*, 676:L5–L8, March 2008.

[97] J. D. Schnittman and J. H. Krolik. The Infrared Afterglow of Supermassive Black Hole Mergers. *Astrophys. J.*, 684:835–844, September 2008.

[98] S. M. O'Neill, M. C. Miller, T. Bogdanovic, C. S. Reynolds, and J. Schnittman. Reaction of Accretion Disks to Abrupt Mass Loss During Binary Black Hole Merger. *ArXiv e-prints*, December 2008.

[99] Alessandra Buonanno, Lawrence E. Kidder, and Luis Lehner. Estimating the final spin of a binary black hole coalescence. *Phys. Rev.*, D77:026004, 2008.

[100] Latham Boyle and Michael Kesden. The spin expansion for binary black hole merger: new predictions and future directions. *Phys. Rev.*, D78:024017, 2008.

[101] Luciano Rezzolla et al. On the final spin from the coalescence of two black holes. *Phys. Rev.*, D78:044002, 2008.

[102] Carlos O. Lousto, Manuela Campanelli, and Yosef Zlochower. Remnant Masses, Spins and Recoils from the Merger of Generic Black-Hole Binaries. 2009.

[103] Carlos Palenzuela, Matthew Anderson, Luis Lehner, Steven L. Liebling, and David Neilsen. Stirring, not shaking: binary black holes' effects on electromagnetic fields. 2009.

[104] Philip Chang, Linda Strubbe, Kristen Menou, and Eliot Quataert. Fossil gas and the electromagnetic precursor of supermassive binary black hole mergers. *Private Communication*, 2009.

[105] M. Shibata. Rotating black hole surrounded by self-gravitating torus in the puncture framework. *Phys. Rev. D*, 76(6):064035, September 2007.

[106] M. Abramowicz, M. Jaroszynski, and M. Sikora. Relativistic, accreting disks. *A&A*, 63:221–224, February 1978.

[107] D. Neilsen, E. W. Hirschmann, and R. S. Millward. Relativistic MHD and excision: formulation and initial tests. *Classical and Quantum Gravity*, 23:505, August 2006.

[108] M. Anderson, E. W. Hirschmann, S. L. Liebling, and D. Neilsen. Relativistic MHD with adaptive mesh refinement. *Classical and Quantum Gravity*, 23:6503–6524, November 2006.

[109] HAD home page. http://www.had.liu.edu/.

[110] S L Liebling. The singularity threshold of the nonlinear sigma model using 3d adaptive mesh refinement. *Phys. Rev.*, D66:041703, 2002.

[111] M. Anderson, Eric W. Hirschmann, Luis Lehner, Steven L. Liebling, Patrick Motl, David Neilsen, Carlos Palenzuela, and Joel E. Tohline. *Phys. Rev.*, D77:024006, 2008.

[112] Matthew Anderson et al. Magnetized Neutron Star Mergers and Gravitational Wave Signals. *Phys. Rev. Lett.*, 100:191101, 2008.

[113] http://www.loni.org/.

[114] Jose A. Font. Numerical hydrodynamics in general relativity. *Living Rev. Rel.*, 3:2, 2000.

[115] J. Frank, A. King, and D. J. Raine. *Accretion Power in Astrophysics: Third Edition.* February 2002.

[116] W. Tucker. *Radiation processes in astrophysics.* 1975.

[117] J. C. B. Papaloizou and J. E. Pringle. The dynamical stability of differentially rotating discs with constant specific angular momentum. *MNRAS*, 208:721–750, June 1984.

[118] P. Goldreich, J. Goodman, and R. Narayan. The stability of accretion tori. I - Long-wavelength modes of slender tori. *MNRAS*, 221:339–364, July 1986.

[119] J. F. Hawley. Global Magnetohydrodynamical Simulations of Accretion Tori. *Astrophys. J.*, 528:462–479, January 2000.

[120] J-P De Villiers and J F Hawley. A numerical method for general relativistic magnetohydrodynamics. *Astrophys. J.*, 589:458, 2003.

[121] O. M. Blaes. Stabilization of non-axisymmetric instabilities in a rotating flow by accretion on to a central black hole. *MNRAS*, 227:975–992, August 1987.

[122] M. Anderson et al. Simulating the emission from shocked accretions disks. *in preparation*, 2009.

Appendix: Copyright Permissions

Part of the work in Chapter 3 is published [46], and permission is granted to reproduce it under the following copyright agreement:

The work in Chapter 4 is published [76], and permission is granted to reproduce it under the following copyright agreement:

The work in Chapter 2 is published [14], and permission is granted to reproduce it under the following publisher's statement (source: http://authors.iop.org/atom/usermgmt.nsf/AuthorServices):

Vita

Miguel Megevand was born in San Vicente, Santa Fe, Argentina. In December of 2003 he obtained a Licenciado degree in physics from the Facultad de Matemática, Astronomía y Física (FaMAF) at the Universidad Nacional de Córdoba. In 2004 he moved to Baton Rouge, Louisiana, to pursue a doctoral degree in physics at Louisiana State University.